# GRAVITATIONAL REDSHIFTS AND THE MASS DISTRIBUTIONS OF GALAXIES AND CLUSTERS

SIMON COGGINS


Thesis submitted to the University of Nottingham
for the degree of Doctor of Philosophy

August 2003

**Supervisor:** Prof. Michael Merrifield
**Examiners:** Dr. Richard de Grijs
Prof. Peter Coles

# Contents

# Abstract

This thesis studies a new method of constraining the mass distributions of elliptical galaxies and clusters of galaxies: gravitational redshift. The aim was to determine the types of astrophysical object in which gravitational redshift can be most readily detected and to attempt to observe the effect for the first time in a single object.

Longslit stellar kinematics were combined with planetary nebulae kinematics to study the mass distribution of M87. Jeans modelling showed that, although the best-fit model gave too little mass ($\Upsilon = 5.34 \pm 0.34$, $\beta = 0.71 \pm 0.03$, $M_{\rm halo} = 2.64 \pm 0.92 \times 10^{12}\,M_{\odot}$), by adjusting the orbital anisotropy it was possible to construct a model that was consistent with both the kinematics and existing X-ray gas measurements.

Longslit kinematics from the literature were used to attempt to determine the mass-to-light ratio of a sample of elliptical galaxies using gravitational redshift. Models were developed to calculate the expected gravitational redshift from the surface brightness profile. The best-fit mass-to-light ratios were found using this model and also obtained independently using the Jeans equation. The results were not statistically inconsistent with the expected $H$-band mass-to-light ratios predicted by stellar population models – the Jeans modelling gave a mean mass-to-light ratio of $\Upsilon_{\sigma} = 1.67 \pm 0.10$, while the gravitational redshift predicted $\Upsilon_{v} = 4.84 \pm 2.67$.

Integral field spectroscopy of the centre of M60 was undertaken in an attempt to detect gravitational redshift in the centre of an individual galaxy for the first time. The velocity field was summed around the galaxy's isophotes to remove the effect of rotation. Models were constructed to predict the gravitational redshift, which were then compared to the data. It was found that the shallow slope of the light profile made it impossible to detect a gravitational redshift in this case, but

that the scatter of the data points suggests that a signal of a few $\mathrm{km\,s^{-1}}$ could be detected. Consideration of the models led to a better understanding of the most suitable targets for this kind of study.

An analysis of the 2dF groups catalogue was made in order to attempt to determine the strength of the gravitational redshift in clusters of galaxies. A new method was developed for measuring the signal in clusters. As part of the analysis, the density distribution of the clusters was obtained. It was found that they followed an exponential profile, which scaled linearly with the size of the cluster. The gravitational redshift was used to attempt to constrain the mean cluster mass, but it was found that the errors were too large to rule out all but the largest masses with any certainty. Future studies would require either a much larger sample, or one which concentrates specifically on the most uniform, high mass clusters.

Gravitational redshift offers a new approach to studying the mass distributions of galaxies and clusters that requires many fewer assumptions regarding the underlying physics than many of the current methods. Unfortunately, it also suffers from a number of potential setbacks. Recent advances in instrument technology, combined with the careful selection of suitable targets should allow gravitational redshift to become a viable tool for studying the nature and distribution of dark matter.

# List of Figures

# List of Tables

# Chapter 1

# Introduction

## 1.1 The Dark Matter Problem

The dark matter problem first came to light due to the work of Oort (1932) and Zwicky (1933). Zwicky applied the virial theorem to radial velocity data from the Coma Cluster, while Oort was measuring the motions of stars in the local Galactic neighbourhood. They both found that the observed motions could not be adequately explained by the mass of the visible matter. They independently suggested that the discrepant motions were caused by unseen non-luminous material, which was exerting a gravitational influence but could not be directly detected.

These early results remained controversial for many years. Eventually, observational techniques improved to the extent that the existence of dark matter became more certain. Numerical simulations by Ostriker & Peebles (1973) provided the motivation for introducing dark halos around spiral galaxies and measurements of the rotation curves of HI gas produced the first convincing evidence for its existence (see Faber & Gallagher (1979) for a review). It became increasingly obvious that dark matter was not only real, but that it contributed to a significant fraction of the mass of the Universe.

Today, understanding the nature of dark matter remains a critical goal of modern astrophysics, as it is known to play a fundamental role in a wide range of different fields. Cosmology has advanced greatly in recent years and it has now reached the stage where cosmological models and simulations are able to make definite predictions about the distribution of dark matter in the Universe. Although they are not successful on all scales (the most popular $\Lambda$CDM models over-predict

the number of satellite galaxies compared to the number observed in the Local Group), it is becoming increasingly important to obtain accurate observational constraints which can be used to test the success of different theoretical models. Particle physicists are interested in the nature of dark matter, as it may take the form of an exotic new fundamental particle, the properties of which cannot be observed in the laboratory.

Since the existence of dark matter can only be inferred by its gravitational influence, its exact composition remains the subject of a great deal of speculation. Dark matter candidates include baryonic matter, such as faint low mass stars, white dwarfs, brown dwarfs (often collectively known as massive compact halo objects, or MACHOs. See e.g. Carr 1994), or more exotic non-baryonic particles such as neutrinos, neutralinos or axions (called weakly interacting massive particles, or WIMPs. See e.g. Roszkowski 1999). The abundances of light elements produced during primordial nuclearsynthesis impose restrictions on the proportion of baryonic matter to $\sim 2-3\%$ of the total mass in the universe. Hence much of the current work is focused on searching for non-baryonic dark matter candidates.

An alternative theory argues that dark matter does not exist at all and that instead the laws of gravity must be adjusted on large scales (Milgrom 1983). Modified Newtonian Dynamics (or MOND) seeks to explain the dynamical evidence for dark matter by altering the gravitational force in the low acceleration regime. In regions where the acceleration due to gravity is very small (below $a_0 = 1.2 \times 10^{-10}\,\mathrm{m\,s^{-2}}$ the effective acceleration approaches $a = \sqrt{g_N\, a_0}$ where $g_N$ is the normal Newtonian acceleration.

Since its introduction MOND has had a number of successes. It correctly predicts a surface-brightness independent Tully-Fisher relation (although one could argue it was designed to do so) and provides good fits to a remarkably wide range of galaxy rotation curves. Despite these achievements MOND is still considered by many to be a rather drastic solution to the dark matter problem.

Since the modification to the force law is a universal one, it should be possible to disprove MOND simply by finding a single object in which the MOND prediction is clearly false. Some claim that such objects already exist, while supporters of MOND have argued that uncertainties in the analysis (such as inaccurate distance determinations and inclinations) are sufficiently large that MOND is still viable.

## 1.2 Existing Methods for Detecting Dark Matter

Typically, the quantity of dark matter in an astrophysical object is determined by comparing dynamical estimates of the mass to the quantity of luminous matter observed. Any discrepancy between the two values obtained is taken to be due to 'dark' material which contributes to the mass but is not emitting sufficient radiation to be observed. As mentioned above, HI emission provides a convenient method for probing the dark matter in spiral galaxies, but most elliptical galaxies contain little or no HI gas, so kinematics must be obtained using stellar absorption features.

### 1.2.1 Stellar Kinematics

The observed spectrum at any point in a galaxy consists of the sum of stellar spectra from the large number of unresolved stars along the observer's line of sight through the galaxy. Since these stars will be travelling with a range of line-of-sight velocities, the absorption lines in the galaxy spectrum will be Doppler broadened by a factor that reflects the independent motions of its constituent stars. Therefore the width of the absorption features in the galaxy contain important information about its dynamical state. Quantitatively, the galaxy spectrum $G(\lambda)$ can be described as the convolution of a typical stellar spectrum $S(\lambda)$ with the line-of-sight velocity profile $F(v_{\rm los})$ (see e.g. Binney & Merrifield 1998)

$$G(\ln\lambda) = \int F(v_{\rm los}) S(\ln\lambda - v_{\rm los}/c)\, dv_{\rm los}. \tag{1.1}$$

where the $v_{\rm los}/c$ term is included to account for the Doppler motions of the galaxy's stars along the line of sight.

In order to obtain the best possible fit, the template spectrum $S(\lambda)$ must accurately represent the unbroadened galaxy spectrum. The template can be obtained from a nearby star observed with the same instrument configuration, a mixture of several different stars, or even a synthetic spectrum generated using stellar population models. In a typical elliptical galaxy, light from K0 type stars tend to dominate the galaxy spectrum and hence provides a reasonable match to the unbroadened galaxy spectrum. Whatever type of spectrum is used, it is important to ensure that the spectral resolution is the same as that of the target galaxy, as

any difference could affect the width of the velocity profile.

Deconvolving Equation 1.1 can be difficult if the signal-to-noise ratio of the galaxy spectrum is low. It is common to parameterise the line-of-sight velocity profile and obtain the required parameters by comparing the galaxy spectrum to the convolution of the stellar template with a range of velocity profiles.

Stellar kinematics are limited to providing velocity information along the line of sight. Extracting the likely mass distribution from the line-of-sight velocity profile can only be done by making assumptions regarding the nature of the galaxy's stellar orbits. The velocity dispersion profile alone does not contain enough information to constrain both the mass and the orbital structure simultaneously (the so-called mass-anisotropy degeneracy – see Binney & Mamon 1982). It becomes necessary to rely upon the higher order moments of the velocity distribution (commonly parameterised by the Gauss-Hermite shape parameters $h_3$ and $h_4$) which are more difficult to determine accurately.

Elliptical galaxies are also characterised by rapidly declining light profiles. This makes it difficult to obtain reliable stellar kinematics in the outer region, where a dark halo is expected to dominate. Fortunately, other luminous tracers which extend beyond the stellar envelope can be used to constrain the mass distribution in that region.

### 1.2.2 Kinematics from Discrete Point Sources

Globular clusters and planetary nebulae can provide hundreds of individual velocity measurements, which can be statistically averaged to provide an insight into the underlying potential. A typical analysis would involve fitting and subtracting a sine wave to the discrete velocities (to remove the effect of rotation) and then dividing the sample into radial bins. The mean velocity and velocity dispersion can then be obtained in each bin by taking the mean and standard deviation of the distribution of velocities, or preferably by using an equivalent but more robust estimator of the properties of the distribution (e.g. Beers, Flynn & Gebhardt 1990).

Using discrete sources instead of stellar kinematics can extend the profiles to larger radii, but it does not avoid the mass-anisotropy degeneracy described above. In fact, the sparser sampling of the velocity distribution offered by discrete

sources usually makes it more difficult to constrain the mass distribution.

### 1.2.3 X-ray Gas

Another luminous tracer that can be found beyond the region that can be probed with stellar kinematics is thermal emission from hot X-ray gas. If it is assumed that the system is spherically symmetric and that the gas has settled into hydrostatic equilibrium with the underlying potential, then the gas can be described by

$$\frac{dP_{\rm gas}}{dr} = -\frac{GM(r)\rho_{\rm gas}}{r^2}, \tag{1.2}$$

where $P_{\rm gas}$ is the gas pressure and $\rho_{\rm gas}$ its density. This can be combined with the ideal gas law to produce an expression for the mass interior to $r$

$$M(r) = \frac{-kT_{\rm gas}}{G\mu m_H}\left(\frac{d\ln\rho_{\rm gas}}{d\ln r} + \frac{d\ln T_{\rm gas}}{d\ln r}\right) r, \tag{1.3}$$

where $T_{\rm gas}$ is the temperature of the gas, $k$ is Boltzmann's constant, $\mu$ is the mean molecular weight and $m_H$ is the mass of the hydrogen atom. To obtain $M(r)$ from Equation 1.3 it is necessary to obtain the density and temperature profiles of the gas. The density can be found by deprojecting the X-ray surface brightness profile, but the temperature profile is harder to obtain and so it is often assumed to be isothermal.

These simplifying assumptions allow the mass to be predicted, but unless they are correct they are likely to introduce significant uncertainty to the final mass determination. Recent observations by Chandra and XMM have provided examples of X-ray gas that is clearly not in hydrostatic equilibrium (McNamara et al. 2001; De Filippis, Schindler & Castillo-Morales 2003) and there is no reason to assume that the gas is likely to be isothermal either. Although it has become typical to make these assumptions in the literature, they could lead to errors in the mass determination as high as a factor of ten (Trinchieri, Fabbiano & Canizares 1986).

Even if the assumptions described above were correct, only the most massive galaxies are likely to have a sufficiently bright halo to allow the mass to be determined. There is also likely to be some question as to whether gas is associated with the galaxy itself or with any cluster of galaxies that surround it.

### 1.2.4 Gravitational Lensing

Gravitational lensing avoids assumptions regarding the underlying physics of the system by directly measuring the distortion of light from a distant source due to the intervening mass distribution. In the case of strong lensing, this results in arc shaped features on the sky which are formed from the distorted and magnified background source (see Wambsganss 1998 for a review). For weak lensing, the effect is less obvious, but statistical analysis of the shapes of a large number of background sources can yield information about the mass density of the intervening lens (see e.g. Kaiser 1996).

Unfortunately this technique suffers from a number of practical problems. For strong lensing, the alignment of the light source and mass must be rather precise, so lensing occurs only in relatively few cases. Even when it does occur, only the total mass within the arc can be obtained, when generally it is the mass distribution that is of more interest.

Weak lensing can be used to obtain mass information as a function of radius, but the number of background galaxies can limit the effectiveness of this approach. Better results can be obtained by statistically averaging over a large sample of galaxies, but then no information about the individual galaxies can be obtained (e.g. Brainerd, Blandford & Smail 1996).

## 1.3 Gravitational Redshift

Measurements of gravitational redshift have the potential to offer another independent way of measuring galaxy mass distributions. Photons are redshifted as they escape from a potential well as a consequence of general relativity. In the Newtonian limit, the gravitational redshift experienced by a photon escaping from a radius $r$ is $-\Phi(r)/c$, where $\Phi(r)$ is the potential and $c$ is the speed of light. This means that the light observed from the centre of a luminous, massive object will appear to be slightly redshifted relative to the outer regions. The magnitude of the effect is dependent on the depth of the potential well (and hence the mass of the object), as well as its distribution.

Like gravitational lensing, this method probes the mass distribution directly by measuring the effect of the underlying galaxy potential on light. Any system

with significant mass would be expected to contain a signal (masses has low as $5 \times 10^8\,M_\odot$ could produce shifts of up to $6\,\mathrm{km\,s^{-1}}$, provided the mass is centrally concentrated enough), so in principle it can be applied to a larger number of independent systems. Since the relationship between the mass distribution and the gravitational redshift profile is straightforward (see Equations 2.10 and 3.1), this method can in principle obtain radial mass information, provided the target is sufficiently bright and extended.

While this approach appears to avoid many of the difficulties which affect existing methods, it is not without problems of its own. The size of the expected gravitational redshift signal (a few $\mathrm{km\,s^{-1}}$ in a typical elliptical galaxy) is rather small compared to Doppler shifts due to galaxy rotation, which can be as large as a few hundred $\mathrm{km\,s^{-1}}$. Fortunately, this type of motion can be distinguished from the central redshift by dividing the velocity profile into symmetric (even) and antisymmetric (odd) components. Provided that the system is in dynamical equilibrium, rotation will only contribute to the odd component, so the even component can be used to determine the gravitational redshift.

There are some situations where coherent motions within the galaxy can mimic the appearance of a gravitational redshift. Merger remnants which have not completely settled into equilibrium within the galaxy could appear similar to gravitational redshift. Patchy dust which conspired to hide only the approaching side of a rotating galaxy could also produce a central redshift. Finally, longslit spectroscopy can lead to a similar signal, if the slit is not correctly aligned on the centre of the galaxy and picks up some rotational motion from the system.

Although these effects can all produce redshifted cores, they are all equally likely to result in a central blueshift. This allows a statistical approach to be used to distinguish between these effects and a true gravitational redshift. This method was used by Stiavelli & Setti (1993) in their investigation of a sample of longslit data from the literature. They found an excess of redshifted cores at 99.9% significance and attributed the result to the effect of gravitational redshift.

Possible detections of gravitational redshift are not only limited to individual galaxies. Cappi (1995) compared the redshift of a sample of central cD galaxies with the mean redshift of their parent cluster and found that the central galaxy was redshifted in 5 out of 6 cases. Broadhurst & Scannapieco (2000) performed the same analysis on another (slightly overlapping) sample of cD galaxies and

obtained a similar result.

Gravitational redshift is a relatively new approach to determining the mass distributions of astrophysical systems that has yet to be fully explored. This thesis is concerned with developing the techniques required to successfully detect gravitational redshift in galaxies and clusters and to understanding how that detection can be used to constrain the distribution of dark matter.

## 1.4 Outline of the Thesis

The layout of this thesis is as follows:

- Chapter 2 describes longslit spectroscopy of `M87`. Stellar kinematics are extracted and used to constrain a two component mass model which extends beyond the luminous matter out into the cluster environment.
- Chapter 3 describes an attempt to measure gravitational redshift from a sample of longslit kinematics taken from the literature. Models are developed to determine the expected magnitude of the effect and compared to the data to obtain the mass-to-light ratio of the sample.
- Chapter 4 details an attempt to use integral field spectroscopy to measure for the first time the gravitational redshift at the centre of an individual elliptical galaxy.
- In Chapter 5, gravitational redshift in clusters of galaxies are considered. A new method of determining the central redshift is applied to the 2dF Percolation-Inferred Galaxy Group catalogue in an attempt to constrain galaxy cluster masses.
- Chapter 6 summarises the results and conclusions from the previous chapters and outlines some possible future directions for this work.

# Chapter 2

# Longslit Spectroscopy of M87

## 2.1 Observations

Spectroscopic data of the giant elliptical galaxy `M87` (`NGC4486`) were obtained during two dark nights (1997 April 9–10) using the 4.2 metre William Herschel Telescope (WHT) on La Palma. Observations were made using the `ISIS` spectrograph (see Carter et al. 1994), a medium resolution, longslit spectrograph mounted on the Cassegrain focus of the WHT.

Overlapping longslits placed at two perpendicular position angles (65° and 155°) allowed spectra to be obtained out to a distance of $\sim 4$ effective radii from the centre. The `ISIS` spectrograph used dichroic slides to simultaneously observe in both the blue and red spectral regions, at wavelengths centred around 4400 Å and 8600 Å respectively. The red arm data were not used in the kinematical analysis, due to obscuration of the main absorption features by strong sky emission lines.

Figure 2.1. shows the position of the slits on the sky. The slits were aligned such that adjacent slits would overlap, increasing the total signal obtained at $\sim 2\,r_{\rm eff}$. The position angle (PA) of 65° was selected to avoid the optical synchrotron jet at 292.5° and roughly match the location of the minor axis at large radii (Peletier et al. 1990). It is also the same PA used by van der Marel (1994) in his analysis of the galaxy's inner region. Data were also obtained for the opposite side of the galaxy, but not used in this analysis because of unresolved data problems which resulted in erroneous kinematics.

Table 2.1 summarises the specifications of the longslit data obtained. The wavelength range observed includes the G-band and a strong Fe I line in the blue

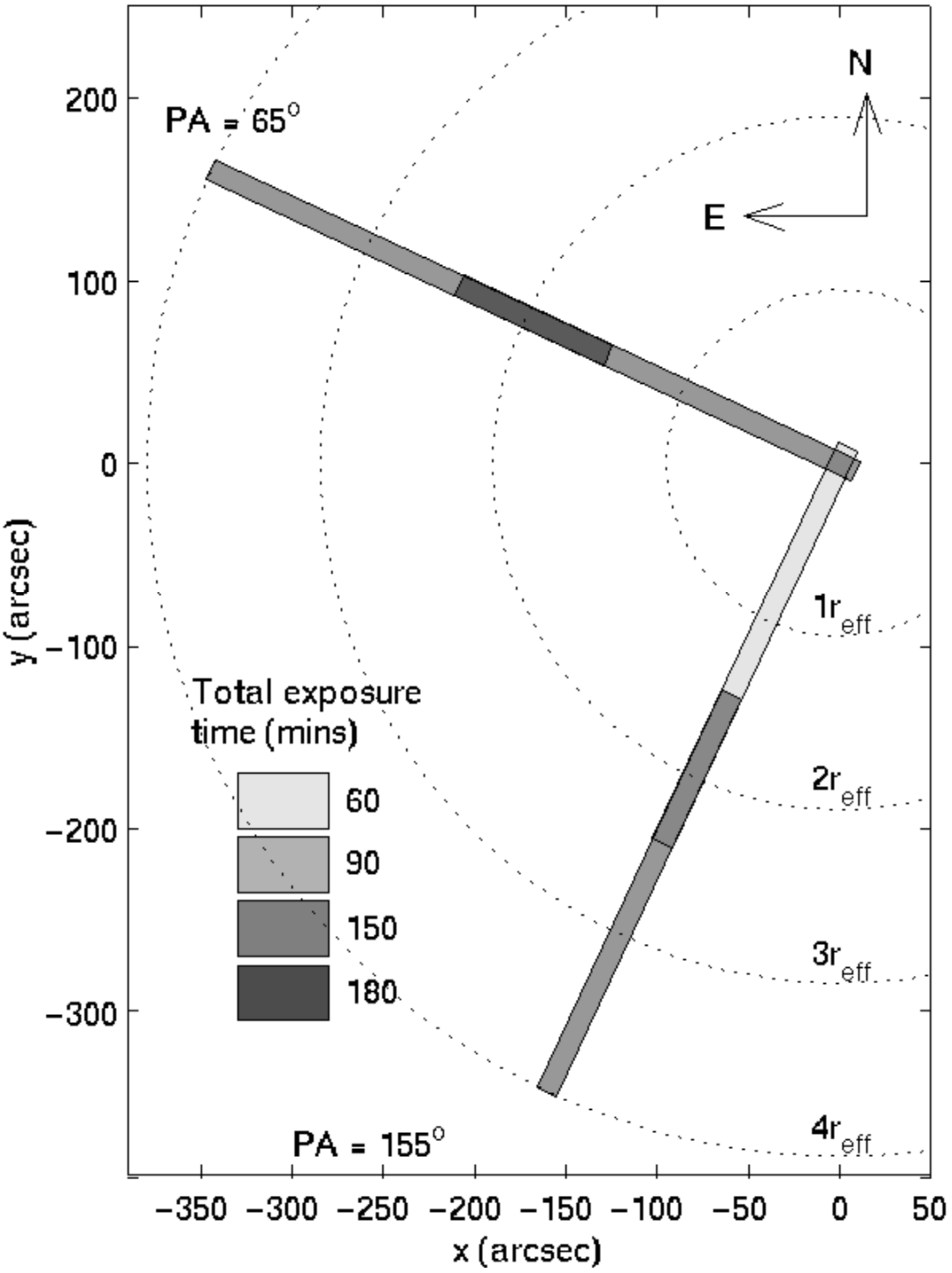


Figure 2.1: Positions of the slits on the sky. The shading represents the total exposure time in that region of the sky. Slit widths have been exaggerated for clarity. Effective radii are also shown as dotted circles.

| | |
|---|---|
| Wavelength range (Å) | $4225 - 4615$ |
| Dispersion (Å pix$^{-1}$) | 0.41 |
| Spectral resolution ($\sigma$) (km s$^{-1}$) | 41.3 |
| Total exposure time (hrs) | 11 |
| Slit width (arcsec) | 2.0 |
| Detector | TEK5 |
| Pixel scale (arcsec pix$^{-1}$) | 1.42 |

Table 2.1: Summary of instrument setup for longslit observations of `M87`.

spectral region (the more commonly used magnesium triplet is obscured by a strong sky line at this redshift). The spectral resolution quoted was obtained by measuring the RMS width of emission lines in the calibration lamp frames. The CCD was binned by a factor of four in the spatial direction.

Galaxy exposures were split into individual 30 minute exposures. During twilight, a selection of late-type stars (ranging from G2 – K3) were observed for use as template stars during the analysis.

## 2.2 Data Reduction and Analysis

The data were reduced using `IRAF`. The CCD frames were first cropped to remove the overscan region. The median of 33 bias frames taken throughout the run was subtracted from the remaining frames. A flat field frame was created to correct for (1) pixel-to-pixel variations in the sensitivity of the CCD detector and (2) the changes in the illumination of the CCD due to variations in the width of the slit and vignetting by the telescope and instrument (the slit profile).

The pixel-to-pixel variations were obtained by fitting and subtracting a 35 piece spline curve to each row of a tungsten calibration frame using the `background` task. The CCD contained a few particularly insensitive regions which tended to disrupt the fit. To prevent this, the 'bad' regions were interpolated over using `imedit`. The fit was made to the corrected frame then subtracted from the original flat field.

Sky flats obtained during twilight were used to determine the slit profile. Two pairs of sky flats, rotated by an angle of 180° to remove the gradient of the sky, were combined. The slit profile was obtained by averaging in the spectral direction. The slit profile and pixel-to-pixel variations were merged to create

the final flat field by scaling both frames to a mean of exactly one count, then multiplying the two frames together. All remaining science frames were then divided by the final flat field.

The wavelength calibration was completed using the `identify`, `reidentify`, `fitcoords` and `transform` IRAF tasks. CuNe+CuAr arc line lamps taken before and after the science frames were used to determine the wavelength solution. Typical RMS errors were found to be in the range $0.04 - 0.15$ Å. 20 arclines were used to perform the fit. During the wavelength calibration, the spectra were also rebinned logarithmically in the spectral direction.

Individual 30 minute exposures were stacked with the `imcombine` task, using a median combine in order to remove cosmic ray hits. The few remaining cosmic ray hits were removed by hand using `imedit`.

The sky was subtracted from the galaxy frames using the `background` task. The spectra from the outer edge of the slit were assumed to be representative of the sky and were subtracted from the inner regions. This may have resulted in the subtraction of a small amount of galaxy light, particularly in the case of the inner slits.

The inner and outer exposures were joined for each position angle by summing the spectra in the overlapping region, in order to increase the signal-to-noise ratio. The combined spectra were then coadded in the spatial direction so that each row had a signal-to-noise ratio of at least 40 in order to ensure that the stellar kinematics could be reliably obtained.

Finally, the continuum was subtracted from both the galaxy and template star frames. This was achieved by fitting the spectra with a low order polynomial.

The data were then analysed using van der Marel's Gauss-Hermite Fourier fitting software (van der Marel & Franx 1993) and Kuijken and Merrifield's Unresolved Gaussian Decomposition technique (Kuijken & Merrifield 1993).

Unresolved Gaussian Decomposition (UGD) extracts the line-of-sight velocity distribution from galaxy spectra by modelling the velocity distribution using the sum of a set of unresolved Gaussians. This technique allows for a wide range of possible distribution shapes while retaining the constraints of smoothness and non-negativity.

The UGD analysis was performed using a variety of unresolved Gaussians com-

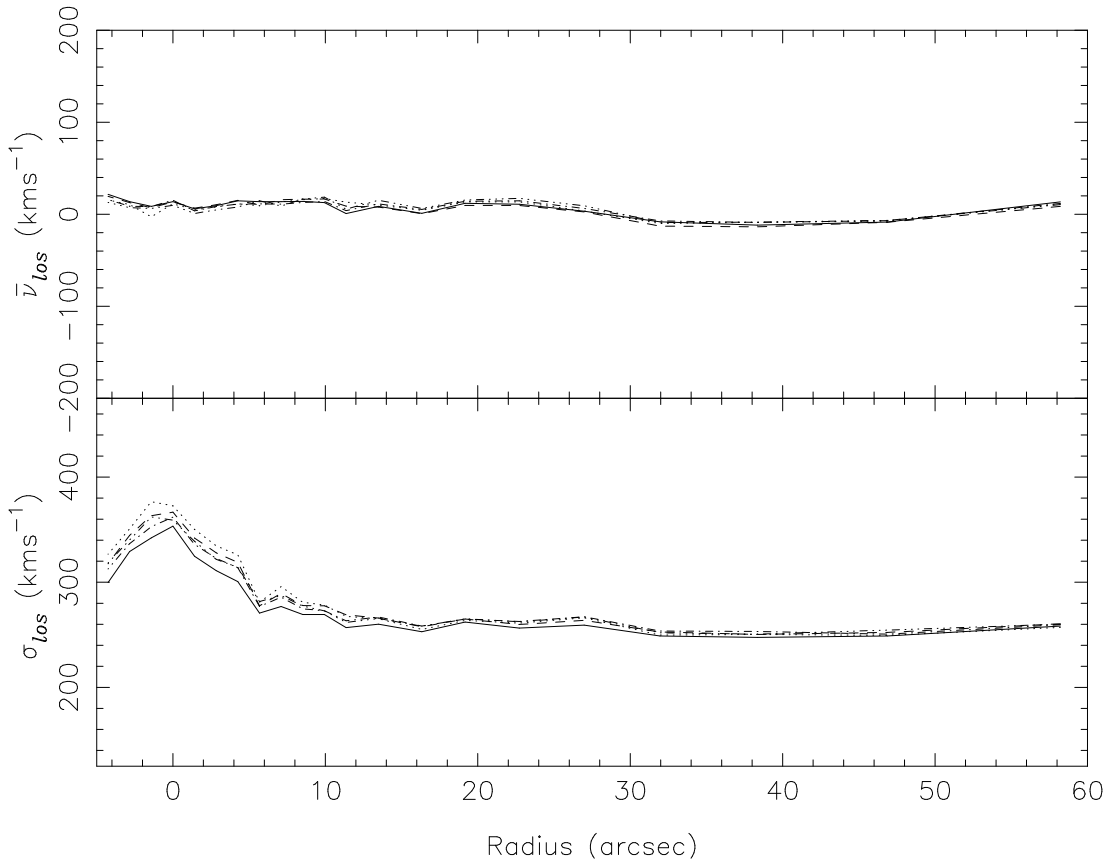


Figure 2.2: UGD analysis of the galaxy using different template stars (solid line: G2, dashed line G5, dotted line G8, dot-dashed K0, dot-dot-dash K2).

ponents as well as a range of different template stars. The results were found to be robust – the final result was not strongly dependent on the parameters used during the analysis. Figure 2.2 shows the variation in kinematical parameters for different template stars. Analysis using a wide range of different template stars alters the result by a maximum of $\sim 20\,\mathrm{km\,s^{-1}}$ in the central region and by a negligible amount in the outer regions. For the final analysis a type K0 was used, which is generally considered to approximate the spectrum of a typical elliptical galaxy.

The data were also analysed using van der Marel's Gauss-Hermite Fourier Fitting Software. The line profiles were modelled with a 4th order Gauss-Hermite series

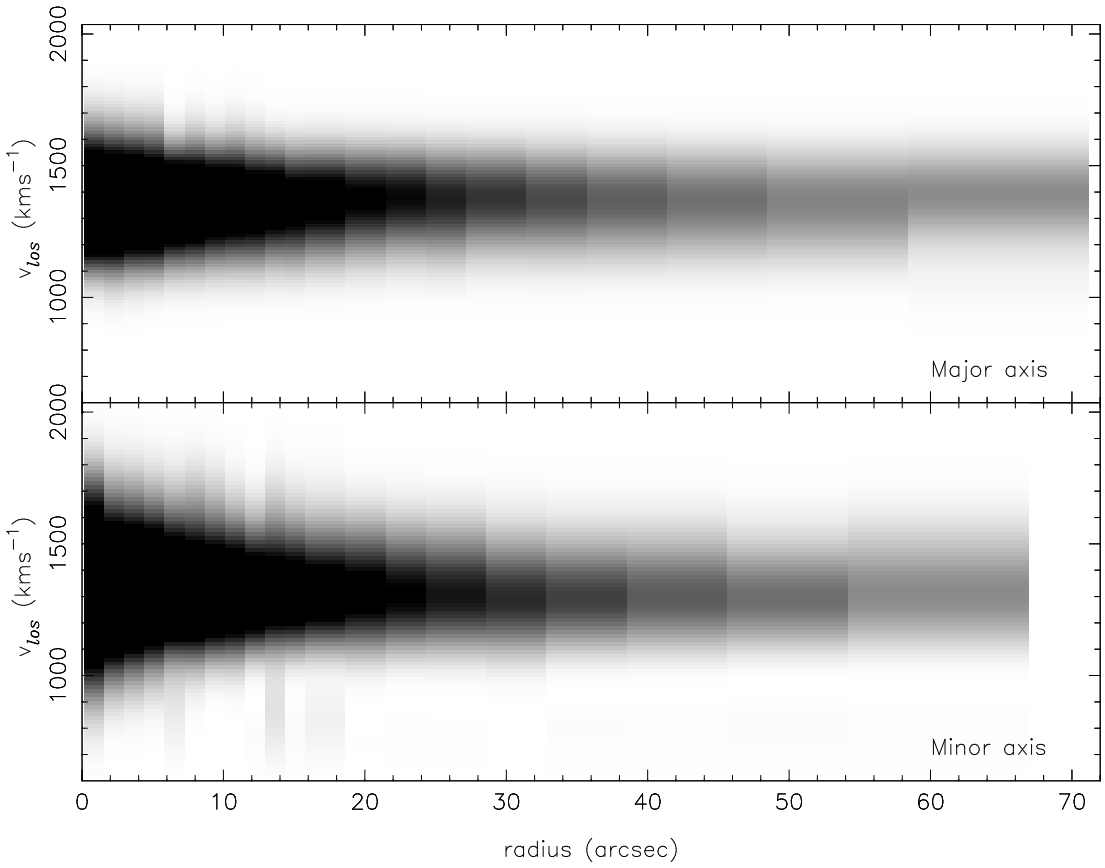


Figure 2.3: UGD line-of-sight velocity profiles for the blue data along the major and minor axes of M87. The greyscale represents the density of stars as a function of velocity and radius.

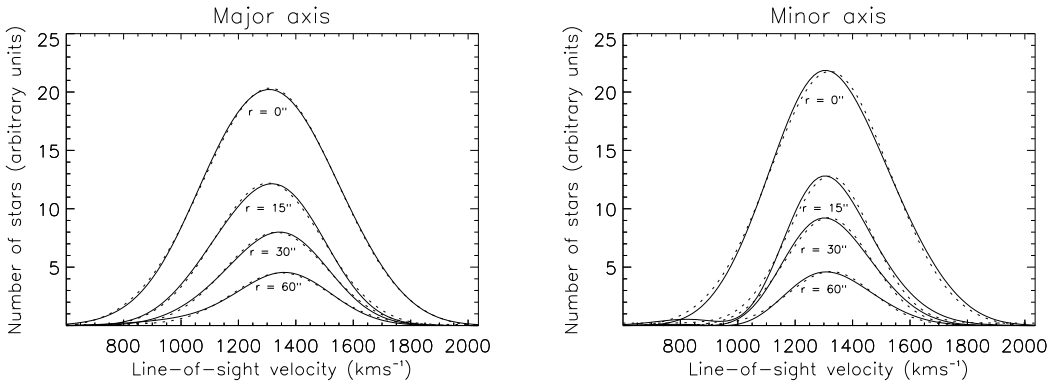


Figure 2.4: Cuts through the UGD line-of-sight velocity profiles at radii of 0, 15, 30 and 60 arcsec (solid lines) and their corresponding best-fit Gaussian distributions (dashed lines).

of the form

$$F(v) = \gamma \frac{1}{\sigma\sqrt{2\pi}} e^{-(v-V)^2/2\sigma^2} \left\{ 1 + \sum_{j=3}^{4} h_j H_j((v-V)/\sigma) \right\}, \qquad (2.1)$$

where $F(v)$ is the line-of-sight velocity distribution as a function of velocity $v$ and $\gamma$, $V$, $\sigma$, $h_3$ and $h_4$ are the parameters of the model (line strength, mean velocity, velocity dispersion and asymmetric and symmetric higher order moments respectively). The functions $H_j((v-V)/\sigma)$ are Hermite polynomials of degree $j$, see van der Marel & Franx (1993) for details.

This parameterisation produced mean velocities, velocity dispersions and the higher order moments $h_3$ and $h_4$, but the latter results were found to be extremely sensitive to changes in the continuum subtraction fit so have not been included.

For both the UGD and Fourier fitting, analyses were performed using the wavelength range $4370 - 4615$ Å. The range $4224 - 4370$ Å, which includes a strong G-band feature, a strong sky line and H$\gamma$ emission was excluded. The G-band region was excluded because it proved impossible to generate a good fit while including this region. This could arise from a template mismatch (the G-band is due to molecular CH while the other strong absorption lines are due to Fe absorption – see Figure 2.5), or be caused by the difficulty in performing a correct continuum subtraction in this region of the spectrum. As shown in Figure 2.5 the continuum subtraction is particularly difficult because of the number of densely packed lines and M87's unusually high velocity dispersion. Several fits to the spectrum at the centre of the galaxy are shown.

The line-of-sight velocity distribution (LOSVD) obtained during the UGD analysis is shown in Figure 2.3. Figure 2.4 show some cuts through the velocity profile (solid lines) and their corresponding best-fit Gaussians (dashed lines). The average RMS residuals were small (0.13 on the major axis and 0.25 on the minor axis). This level of Gaussianity is in agreement with van der Marel (1994), who found no deviation in the $h_3$ and $h_4$ parameters in the inner 25 arcsec.

Figure 2.6 shows the mean velocity and velocity dispersion profiles of M87. The results from this work are shown in black as filled circles (UGD analysis) and open circles (Fourier fitting method). The error bars show the formal errors which are output by these programs. While the errors on the mean velocity are expected to provide a reasonable estimate of the uncertainty, the same cannot

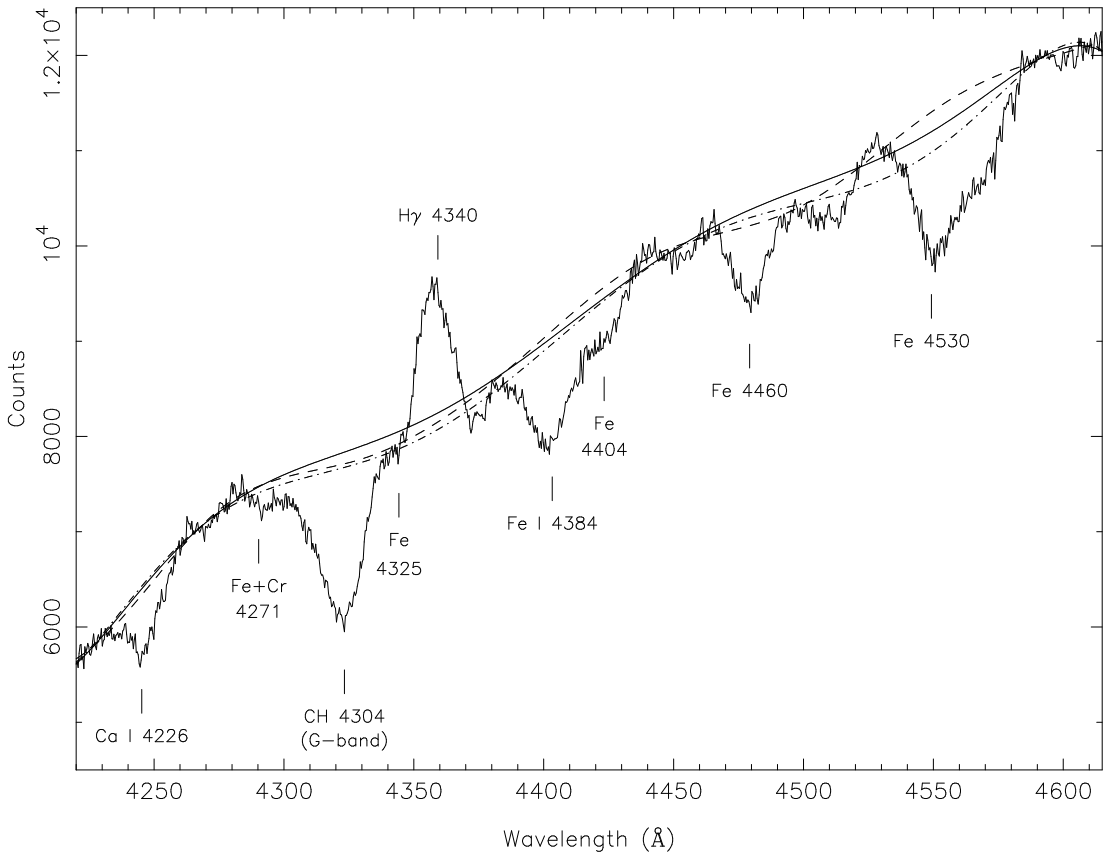


Figure 2.5: Example spectrum from the centre of M87. The smooth lines show various possible continuum fits. The solid line is the fit used. Strong spectral features are labelled with the source elements and rest-frame wavelengths from Williams (1976).

be said of the errors on the velocity dispersion. Unless the shape of the line-of-sight velocity profile is assumed to be Gaussian, the formal error on the velocity dispersion depends on the 4th order moment. Since estimates of this quantity are difficult to determine with any accuracy, the error on $\sigma$ is ill-defined. Kuijken & Merrifield's UGD package acknowledges this limitation and does not attempt to even estimate the error on the velocity dispersion. Van der Marel's Fourier fitting routine does provide errors, but they should be interpreted with caution.

On the major axis the results from this work are compared with the stellar kinematics from Sembach & Tonry (1996) (grey squares) and a single point from Winsall & Freeman (1993) (open triangle). On the minor axis, data from van der Marel (1994) are shown (grey squares). Velocity dispersion measurements from a

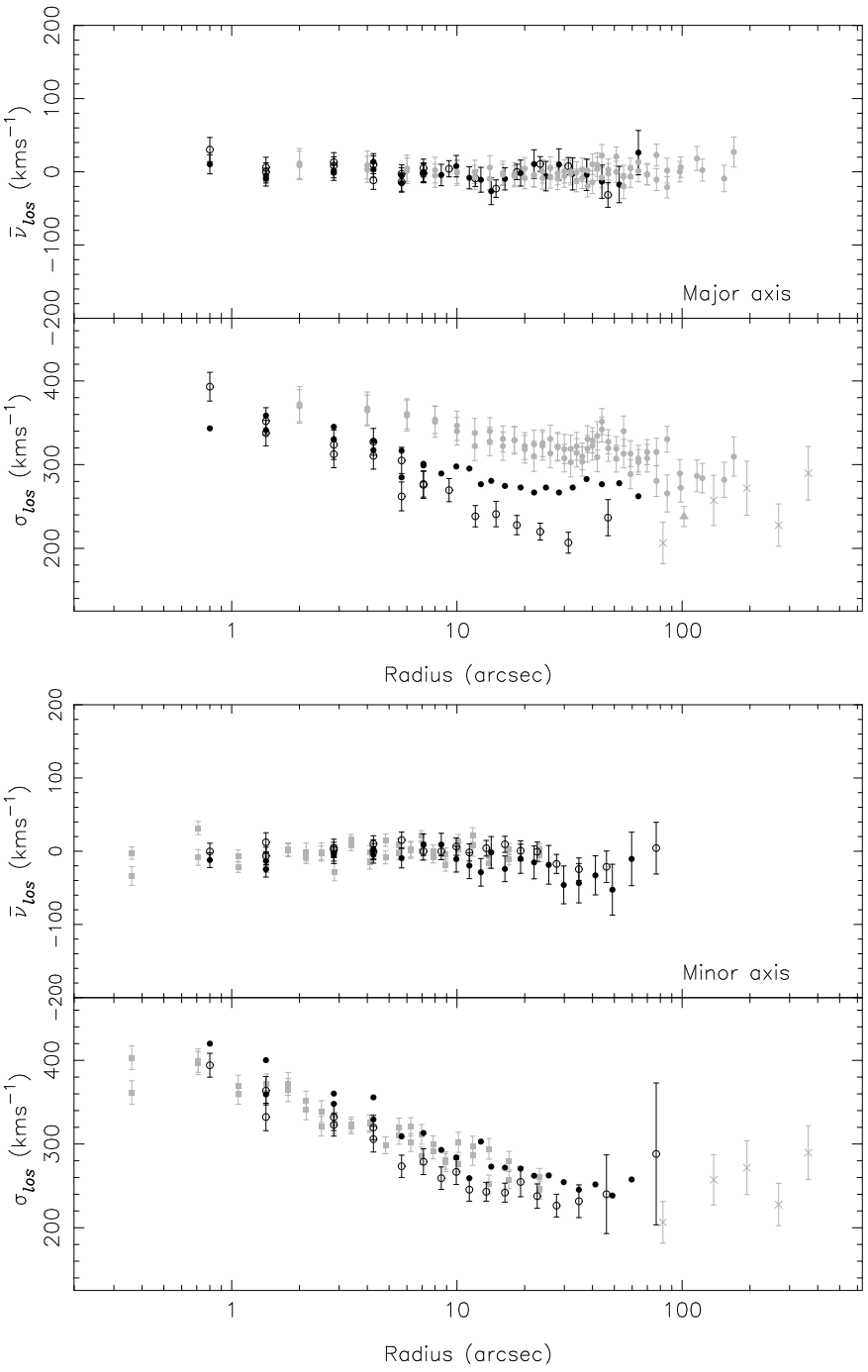


Figure 2.6: Major axis (top panel) and minor axis (bottom panel) kinematics of M87. The longslit data from this work analysed using UGD is shown by the filled circles. The same data analysed using van der Marel's Fourier fitting technique is shown by the open circles. Data from other authors is shown in grey. For the major axis data are from Sembach & Tonry (1996) (circles) and Winsall & Freeman (1993) (single triangle). For the minor axis, data are from van der Marel (1994) (squares). Velocity dispersions obtained from planetary nebulae kinematics by Romanowsky et al. (2003, in preparation) are shown on both plots (crosses). The data are folded around the galaxy centre where appropriate.

sample of 200 planetary nebulae (Romanowsky et al, 2003, in preparation) have also been included on both axes (grey crosses).

The mean velocity profiles show excellent agreement between the two methods and with existing kinematics and indicate that M87 has essentially no rotation around either axis. The minor axis velocity dispersion profile also appears to show a consistent picture, with the dispersion rising sharply in the centre. On the major axis the dispersion shows less agreement - the UGD analysis indicates shallower slope and lower central dispersion, while the Fourier fitting method gives results that are consistent with the minor axis profile. The results of Sembach & Tonry suggest a larger velocity dispersion at all radii; however, they state that their dispersion measurements suffer from a zero point offset of at least $6-7\%$. They cite a combination of their large slit width and velocity effects due to spectrograph flexure as an explanation for the difference. In reality the offset appears to be even great (at least 20% or more). Sembach & Tonry employed a novel approach to subtract the sky from their spectra in the outer regions which could have resulted in a systematic offset. Since the results from this work are consistent all the other kinematic data available it is assumed that the Sembach & Tonry data are in error.

At large radii, the velocity dispersion shows good agreement with the planetary nebulae kinematics and to the single data point from Winsall and Freeman. The smooth transition to a gently rising profile provides an important consistency check since the planetary nebulae kinematics were obtained completely independently using an entirely different kinematical tracer population.

Overall, the results obtained using the Fourier fitting method were found to be more robust than the UGD analysis (small changes to the input parameters had less effect on the resulting stellar kinematics). Existing stellar kinematics suggest that the line-of-sight velocity profiles of M87 are close to Gaussian in form, with no kinematically distinct components, so should be well fit by a Gauss-Hermite series. Finally, the Fourier fitting data was found to be more consistent with the apparent spherical symmetry of M87. For these reasons, the stellar kinematics obtained using the Fourier fitting method were used in the subsequent dynamically modelling. Since the planetary nebulae data extends the velocity dispersion beyond the extent of the stellar kinematics, they have also been included in the analysis.

## 2.3 Dynamical Modelling of the Stellar Kinematics

### 2.3.1 Photometry of M87

In order to model the dynamics it is necessary to determine the stellar density distribution of the galaxy (see Equation 2.4). The light profile was parameterised using a Nuker law fit (Lauer et al. 1995) to $V$-band HST surface photometry from Byun et al. (1996). The Nuker law has the form

$$I(R) = I_b \, 2^{(\beta-\gamma)/\alpha} \left(\frac{r}{r_b}\right)^{-\gamma} \left[1 + \left(\frac{r}{r_b}\right)^{\alpha}\right]^{-(\beta-\gamma)/\alpha}. \tag{2.2}$$

This projected light profile is a combination of two power laws with slopes $\gamma$ and $\beta$ in the inner and outer regions respectively. The radius of the transition between the two slopes is given by $r_b$, while $\alpha$ determines the sharpness of the break. $I_b$ is the luminosity density at $r_b$.

For a spherical system, $I(R)$ can be deprojected to obtain the luminosity density $\nu(r)$ using an Abel transform (e.g. Binney & Tremaine 1987, hereafter BT)

$$\nu(r) = -\frac{1}{\pi} \int_r^{\infty} \frac{dI}{dR} \frac{dR}{\sqrt{R^2 - r^2}}, \tag{2.3}$$

where $r$ and $R$ are the intrinsic and projected radii respectively. A distance of 16.1 Mpc taken from the surface brightness fluctuation survey of Tonry et al. (2001) was used to convert the luminosity density to physical units.

The assumption of spherical symmetry is used throughout the modelling process. The ellipticity of the luminosity profile is small enough ($\epsilon = 0.09$, Peletier et al. 1990) to make this approximation valid, assuming that the galaxy is not intrinsically highly flattened and viewed face-on.

### 2.3.2 Dynamical Modelling

For a spherical galaxy in hydrostatic equilibrium, the Jeans equation defines the relationship between the velocity dispersion, the shape of the stellar orbits and

the potential, $\Phi$, of the system (see BT)

$$\frac{1}{\nu}\frac{d(\nu\,\overline{v_r^2})}{dr} + 2\frac{\beta\overline{v_r^2}}{r} = -\frac{d\Phi}{dr}, \tag{2.4}$$

where $\overline{v_r^2}$ is the mean square radial velocity and $\beta$ is a parameter describing the anisotropy of the stellar orbits. $\beta$ is defined as:

$$\beta \equiv 1 - \frac{\overline{v_\theta^2}}{\overline{v_r^2}}, \tag{2.5}$$

where $\overline{v_\theta^2}$ is the mean square velocity in the tangential direction. Thus, for isotropic orbits $\beta = 0$, for radially anisotropic orbits $0 < \beta \leq 1$ and for tangentially anisotropic orbits $\beta < 0$.

The mean square radial velocity can be transformed into the observable projected velocity dispersion $\sigma_p$ using a luminosity weighted integral along the line of sight

$$\sigma_p^2(R) = \frac{2}{I(R)}\int_r^\infty \left(1 - \beta\frac{R^2}{r^2}\right)\frac{\nu\,\overline{v_r^2}\,r\,dr}{\sqrt{r^2 - R^2}}. \tag{2.6}$$

Equation 2.4 can be used to determine a galaxy's mass-to-light ratio and orbital anisotropy from its stellar velocity dispersion profile in two ways. The first approach is to deconvolve the observed velocity dispersion profile to account for the presence of seeing and spatial binning, which can then be used to directly determine the unique mass-to-light ratio and orbital anisotropy (Binney & Mamon 1982). Alternatively, the projected velocity dispersion profile can be predicted for a range of models, adjusted for seeing and binning, then compared to the observed kinematics. By statistically comparing the data to a range of models the best-fit values can be obtained. Since the deconvolution technique required by the former approach can prove difficult in the presence of noisy data, the latter of the two methods was adopted, which is described in more detail below.

The potential used in Equation 2.4 is obtained as follows. The mass density of the system $\rho(r)$ can be obtained from the luminosity density, assuming a constant mass-to-light ratio $\Upsilon$. If $\Upsilon$ is defined in terms of the solar mass-to-light ratio as

$$\Upsilon \equiv (M/L)/(M/L)_\odot, \tag{2.7}$$

then the density profile is given by

$$\rho(r) = \nu(r)\Upsilon. \tag{2.8}$$

From the density, the mass enclosed can be calculated by summing concentric shells of radius $dr$

$$M(r) = \int_0^\infty 4\pi\, r^2 \rho(r)\, dr. \tag{2.9}$$

At this stage it is straightforward to add a massive central black hole simply by increasing $M(r)$ by a constant black hole mass at all radii. The mass distribution can then be used to determine the potential

$$\Phi(r) = -\int_r^\infty \frac{GM(r)}{r^2}\, dr. \tag{2.10}$$

The projected velocity dispersion of the model is then calculated using Equations 2.4 and 2.6.

### 2.3.3 Seeing and Spatial Binning

The effects of seeing are modelled by convolving the velocity dispersion profile with a Gaussian. For a velocity dispersion profile in the absence of seeing, $\sigma_p(R')$, the seeing corrected profile, $\sigma_{\rm conv}(R)$, is given by (e.g. Binney & Merrifield 1998)

$$I_{\rm conv}(R)\,\sigma^2_{\rm conv}(R) = \int_0^\infty dR'\, R'\, I(R')\,\sigma_p^2(R')\, I_0\left(\frac{RR'}{s^2}\right)\frac{1}{s^2}\exp\left(-\frac{R^2+R'^2}{2s^2}\right), \tag{2.11}$$

where $s$ is the RMS width of the Gaussian seeing kernel and $I_0$ is a modified Bessel function of order zero.

When $RR'/\sigma^2$ is large, the modified Bessel function is approximated by

$$I_0(x) \approx \frac{1}{\sqrt{2\pi x}}\exp(x), \tag{2.12}$$

(see Press et al. 1992) so Equation 2.11 can be written as

$$I_{\rm conv}(R)\,\sigma^2_{\rm conv}(R) = \int_0^\infty dR'\, R'\, I(R')\,\sigma_p^2(R')\frac{1}{s\sqrt{2\pi\, R\, R'}}\exp\left(-\frac{1}{2s^2}(R-R')^2\right). \tag{2.13}$$

The velocity dispersion, $\sigma_p$, is binned radially by taking the luminosity weighted average

$$\sigma^2_{\rm bin} = \frac{\displaystyle\int_{R_{\rm min}}^{R_{\rm max}} I(R)\,\sigma_p^2(R)\, dR}{\displaystyle\int_{R_{\rm min}}^{R_{\rm max}} I(R)\, dR}, \tag{2.14}$$

where $R_{\rm min}$ and $R_{\rm max}$ are the radial boundaries of the bin.

### 2.3.4 NFW Density Profile Models

Substantial dark halos are thought to exist around some if not all elliptical galaxies (see Ashman (1992) for a review). Equally, it has long been known from X-ray gas observations that clusters of galaxies contain significant quantities of dark matter (e.g. Henry, Briel & Nulsen 1993). Indeed, the earliest prediction of dark matter was in the context of 'missing matter' in the Coma Cluster (Zwicky 1933; Zwicky 1937).

In the case of M87, which is the dominant central galaxy in the rich Virgo Cluster, both the galaxy and cluster halo are likely to contain significant quantities of dark matter. The smooth transition from the flat stellar velocity dispersion to the gently rising planetary nebulae profile may suggest that the potential of the cluster begins to exert an influence on the kinematics of M87 at a radius of $\gtrsim$ 100 arcsec. The shape of the profile could indicate that the velocity dispersion is rising to match that of the cluster.

In order to take both mass contributions into account the density profile was modelled as a two component system, consisting of the constant mass-to-light ratio component described above and a more extended dark matter halo. The universal density profile of Navarro, Frenk & White (1997), hereafter NFW, was used to represent the halo:

$$\rho(r) = \frac{\rho_{\rm crit}\delta_c}{(r/r_s)(1+r/r_s)^2}, \tag{2.15}$$

where $r_s$ is a scale radius, $\rho_{\rm crit}$ is the critical density for closure given by

$$\rho_{\rm crit} = \frac{3H_0^2}{8\pi G}, \tag{2.16}$$

and $\delta_c$ is a characteristic density

$$\delta_c = \frac{200}{3}\frac{c^3}{\ln(1+c) - c/(1+c)}. \tag{2.17}$$

The concentration parameter, $c$, is related to the scale radius by

$$c = \frac{r_{200}}{r_s}, \tag{2.18}$$

where $r_{200}$ is the radius at which the density profile is truncated. This is necessary to keep the model physical at large radii, since $\rho(r) \propto r^{-3}$ when $r \gg r_s$ which would result in $M(r)$ diverging as $\ln r$ for large $r$ if the profile was not truncated. $r_{200}$ is defined as the radius of a sphere within which the mean density is 200 times the mean density of the Universe.

Numerical simulations suggest a good correlation between the concentration and the total mass of the halo. The dependence of $c$ on $M$ was modelled using the method of Seljak (2000)

$$c = c_0(M/M_*)^\beta \tag{2.19}$$

where $c_0 = 10$ and $\beta = -0.2$ from Seljak (2000) and $M_* \simeq 1.5 \times 10^{13}\, h^{-1} M_\odot$ from Bullock et al. (2001) for a ΛCDM universe. The exact values of $c_0$ and $\beta$ depend on the details of the cosmological model. Fortunately, the predicted velocity dispersion profile was found to be only weakly dependent on the concentration of the NFW profile.

## 2.4 Results

### 2.4.1 Models with Central Black Holes

Figure 2.7 shows the constraints on $\Upsilon$ and $\beta$ provided by the stellar kinematics. The figure shows the error contours for two models, one without a central black hole and the other with a black hole of mass $2 \times 10^9\, M_\odot$. Figure 2.8 shows the best-fit parameters when the mass of the central black hole is allowed to vary in order to produce the best-fit. The greyscale indicates the black hole mass increasing as the orbits become more tangential. When the mass in the black hole reaches zero, mass can no longer be exchanged for anisotropy and the contour lines become more closely packed together. The black hole mass at $\chi^2_{\rm min}$ is $4.48 \times 10^8\, M_\odot$, although the $1\sigma$ contours allow a black hole in the mass range $0 - 3.73 \times 10^9\, M_\odot$, which is consistent with existing measurements of $M_{\rm BH} = 2.4 \pm 0.7 \times 10^9\, M_\odot$ (Harms et al. 1994) and $M_{\rm BH} = 3.2 \pm 0.9 \times 10^9\, M_\odot$ (Macchetto et al. 1997).

Table 2.2 gives the values of $\Upsilon$ and $\beta$ obtained for different models. The best-fit mass-to-light ratio of $\Upsilon_V = 7.12 \pm 0.21$ compares well with the value of $\Upsilon_I = 2.941$ obtained by van der Marel (1994), which corresponds to $\Upsilon_V = 7.25$ when using

| Black hole mass | $\chi^2_{\rm min}$ | $\Upsilon$ | $\beta$ |
|---|---|---|---|
| Fixed 0 $M_\odot$ | 31.7 | $7.07 \pm 0.21$ | $0.64 \pm 0.024$ |
| Fixed $2 \times 10^9\, M_\odot$ | 32.0 | $7.08 \pm 0.17$ | $0.56 \pm 0.025$ |
| Best-fit ($4.48 \times 10^8\, M_\odot$) | 31.6 | $7.12 \pm 0.21$ | $0.61 \pm 0.13$ |

Table 2.2: Results for models with a range of central black hole masses. Mass-to-light ratios are $V$-band in solar units.

a $(V-I)$ colour of 1.73 mag from Lauer et al. (1992). Van der Marel obtained a slightly lower value for $\beta$, 0.478 rather than $0.61 \pm 0.13$ from this study.

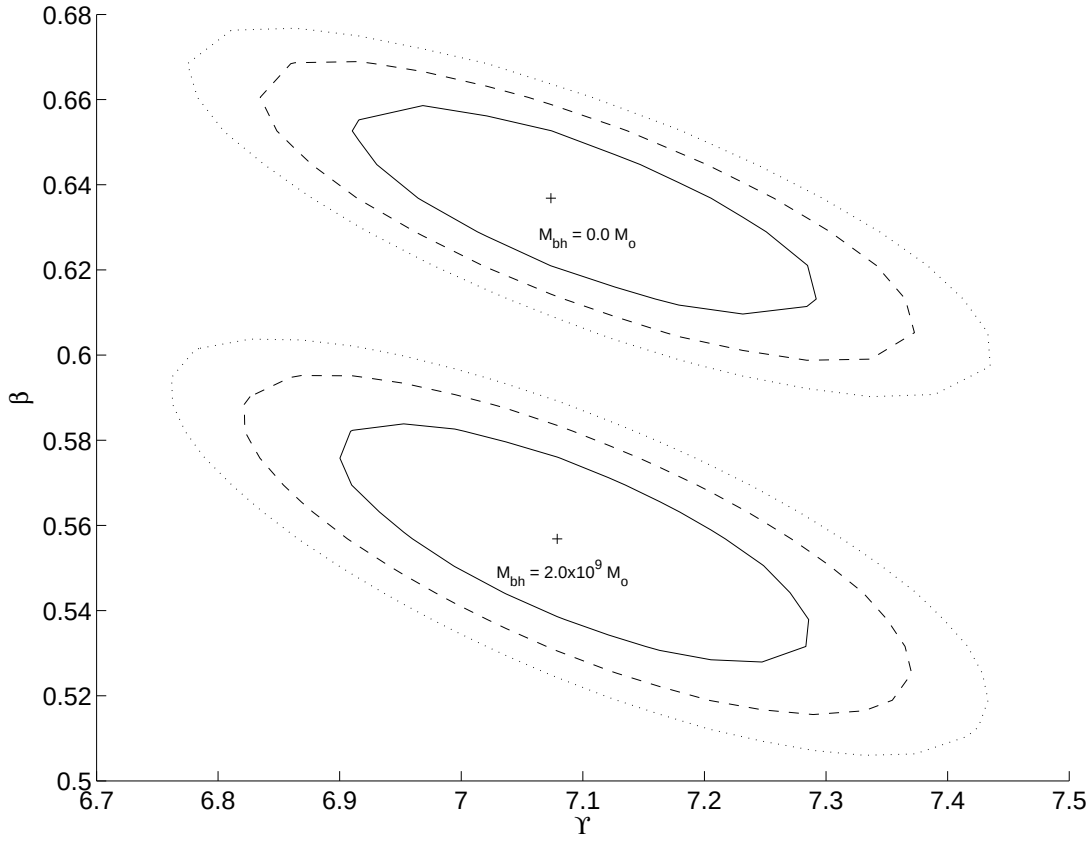


Figure 2.7: Constraints on mass-to-light ratio and anisotropy from the stellar kinematics with and without a $2 \times 10^9\, M_\odot$ central black hole. Solid, dashed and dotted lines indicate the $1\sigma$, $2\sigma$ and $3\sigma$ contours respectively.

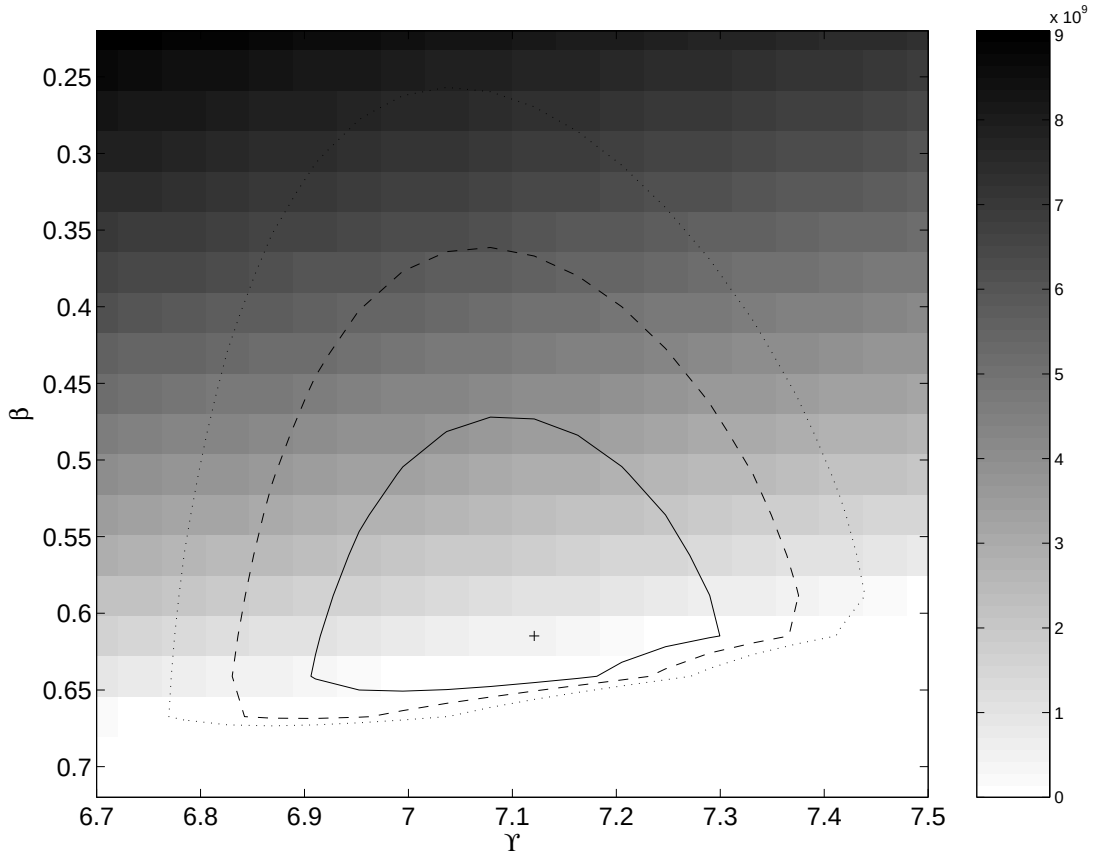


Figure 2.8: Mass-to-light ratio and anisotropy where the black hole mass is chosen so as to provide the best-fit to the data. The best-fit is shown by the cross, the greyscale shows the black hole mass in solar masses and the solid, dashed and dotted lines indicate the 1, 2 and $3\sigma$ contours respectively.

### 2.4.2 Models with Dark Halos

The data were also fitted with the two component model described in Section 2.3.4, in an attempt to determine the mass of the galaxy's dark halo and investigate the transition between M87 and the Virgo Cluster.

The mass of the dark halo was fitted to the data for a range of values of the stellar mass-to-light ratios and orbital anisotropy. The best-fit results are shown in Figure 2.9. The greyscale indicates the mass of the NFW halo. The minimum $\chi^2$ occurs at $\Upsilon = 5.34 \pm 0.34, \beta = 0.71 \pm 0.03$. The corresponding halo mass is $M_{\rm halo} = 2.64 \pm 0.92 \times 10^{12}\, M_\odot$.

The solid line in Figure 2.10 shows the velocity dispersion profile of the best-fit

model. The profile fits the data well in the inner region, but is not as successful at matching the gentle rise in the velocity dispersion given by the planetary nebulae data. Quantitatively, the best-fit model has $\chi^2 = 60.2$, which indicates it is inconsistent with the data at 98% confidence level. Examination of the fit by eye suggests that the large value of $\chi^2$ could be caused not only by the poorness of fit in the outer regions, but also because of a few discrepant data points from the stellar kinematics. The points are inconsistent with the rest of the data over a spatial scale where the dispersion profile is expected to be smooth. Alternatively, it could be due to some unknown but astrophysically real phenomena. For example if one of M87's many globular cluster systems happened to fall on the slit, it could result in a drop in the observed velocity dispersion. This conclusion is confirmed by removing the poorest fitting data points from the sample and recalculating $\chi^2$. Sequentially removing the three most discrepant data points reduces the value of $\chi^2$ from its inital value of 60.2 to 52.0, 44.5 and 39.8 respectively.

### 2.4.3 Comparison of the Mass Distribution with Results from the Literature

M87 is probably one of the most studied galaxies in the sky, hence there have been many previous observations which have attempted to constrain its mass distribution. To see if this work is consistent with existing measurements of the cluster mass the approach of Cohen & Ryzhov 1997 was followed. This involved plotting the enclosed mass over a wide range of radii (Figure 2.11). The plot includes constraints obtained using a range of techniques. The diamonds were obtained from stellar kinematics by Sargent et al. (1978) in a similar fashion to this work. The crosses with error bars and the single square show the mass predictions from globular cluster kinematics of Cohen & Ryzhov (1997) and Mould et al. (1990) respectively. This is obtained by dividing the discrete globular cluster velocities into radial bins before computing the dispersion of each bin. Finally the dotted lines show the upper and lower mass limits obtained from the X-ray gas observations of Nulsen & Bohringer (1995) obtained using ROSAT. The temperature and density of hot gas in the halo is used to determine the mass of the cluster, under the assumption that the gas is in hydrostatic equilibrium.

Although the best-fit model does not provide a good fit to the X-ray data at

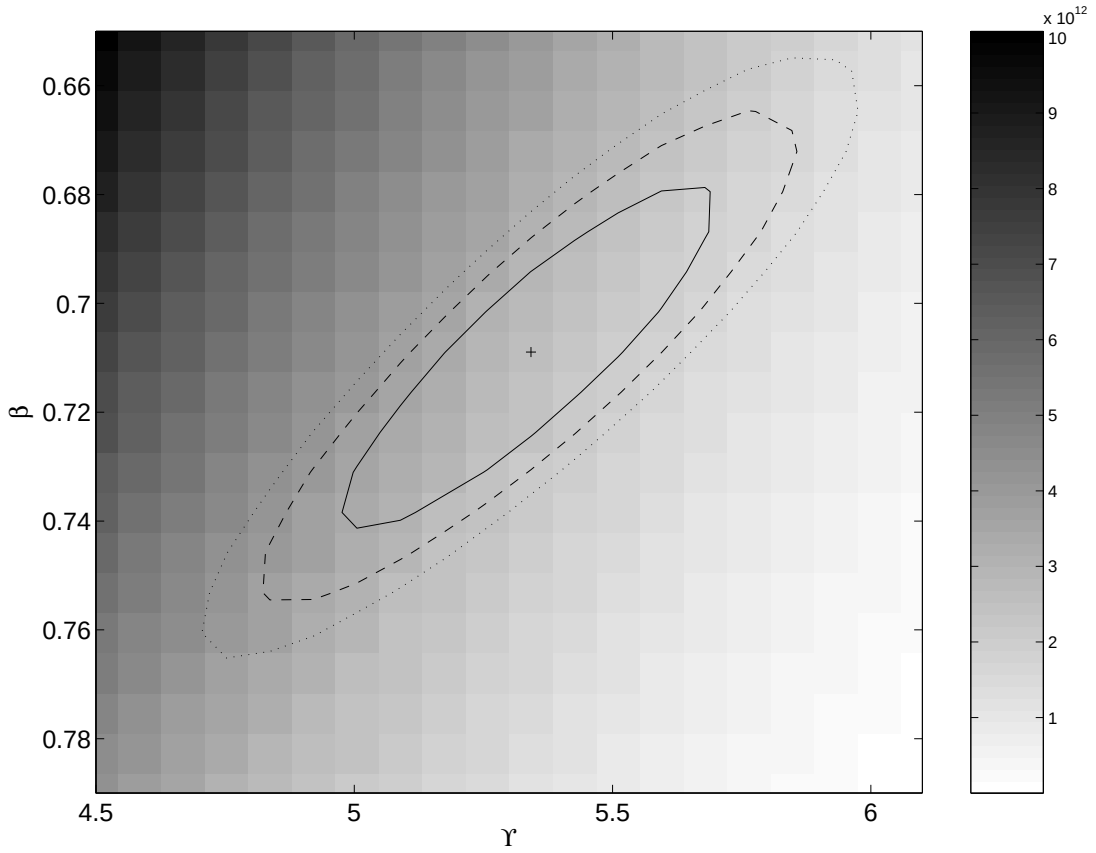


Figure 2.9: Mass-to-light ratio and anisotropy for a two component mass model. The halo mass is shown by the greyscale. The solid, dashed and dotted lines indicate the 1, 2 and $3\sigma$ contours respectively.

large radii, it is possible to generate a mass model that fits the full range of mass data while still providing a reasonable fit to the stellar kinematics. The dashed line shows a model with $M_{\rm halo} = 7.6 \times 10^{13}\, M_{\odot}$ with $\beta = 0.8$ in the centre and $\beta = -1.0$ in the outer regions. Figure 2.12 shows the velocity dispersion profile with this new model included as a dashed line. The fit to the data is not significantly worse than the best-fit model ($\chi^2 = 73.9$).

It should be noted that the high mass model is not physically motivated, it was simply constructed to fit the stellar kinematics and X-ray data simultaneously. It does however serve to illustrate that the problem is ill-constrained, as models with masses that differ by a factor of ten can both be made to fit the data by adjusting the galaxy's orbital anisotropy.

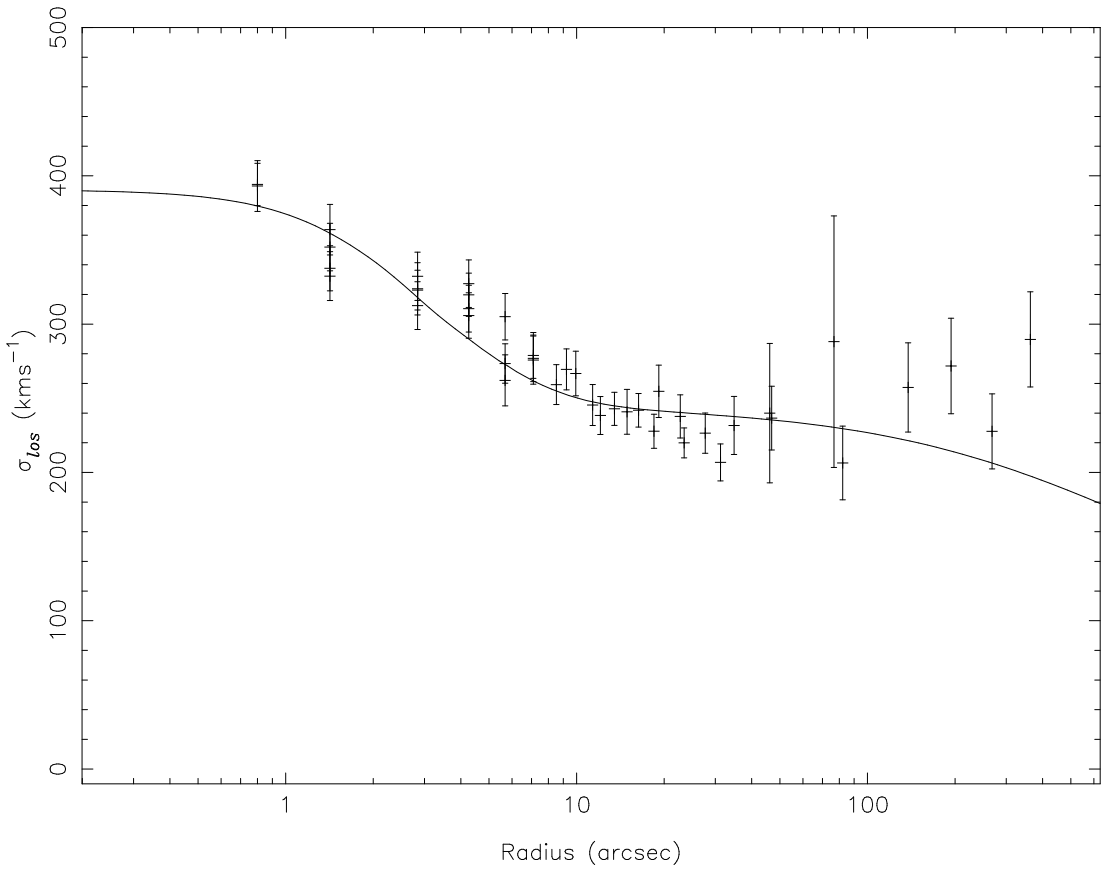


Figure 2.10: Velocity dispersion profile for the best-fit model (solid line). Both the stellar kinematics obtained using the Fourier fitting method and the planetary nebulae data of Romanowsky et al. (2003) are used to obtain the fit.

## 2.5 Summary

Stellar and planetary nebulae kinematics were used to constrain the mass distribution of M87. A three parameter model was fitted to the stellar kinematics to obtain a best-fit mass-to-light ratio, anisotropy and central black hole mass. A second model treated the mass distribution as a two component system, fitting the mass-to-light ratio, anisotropy and dark halo mass to longslit and planetary nebulae data over a large spatial scale.

The first model found the mass-to-light ratio $\Upsilon$ to be 7.12±0.21 and the anisotropy parameter $\beta$ to be $0.61 \pm 0.13$. The black hole mass was only poorly constrained, with values between $0\,M_{\odot}$ and $3.73 \times 10^{9}\,M_{\odot}$ lying within the $1\sigma$ contour. The predictions are largely consistent with existing results. The poor constraint on

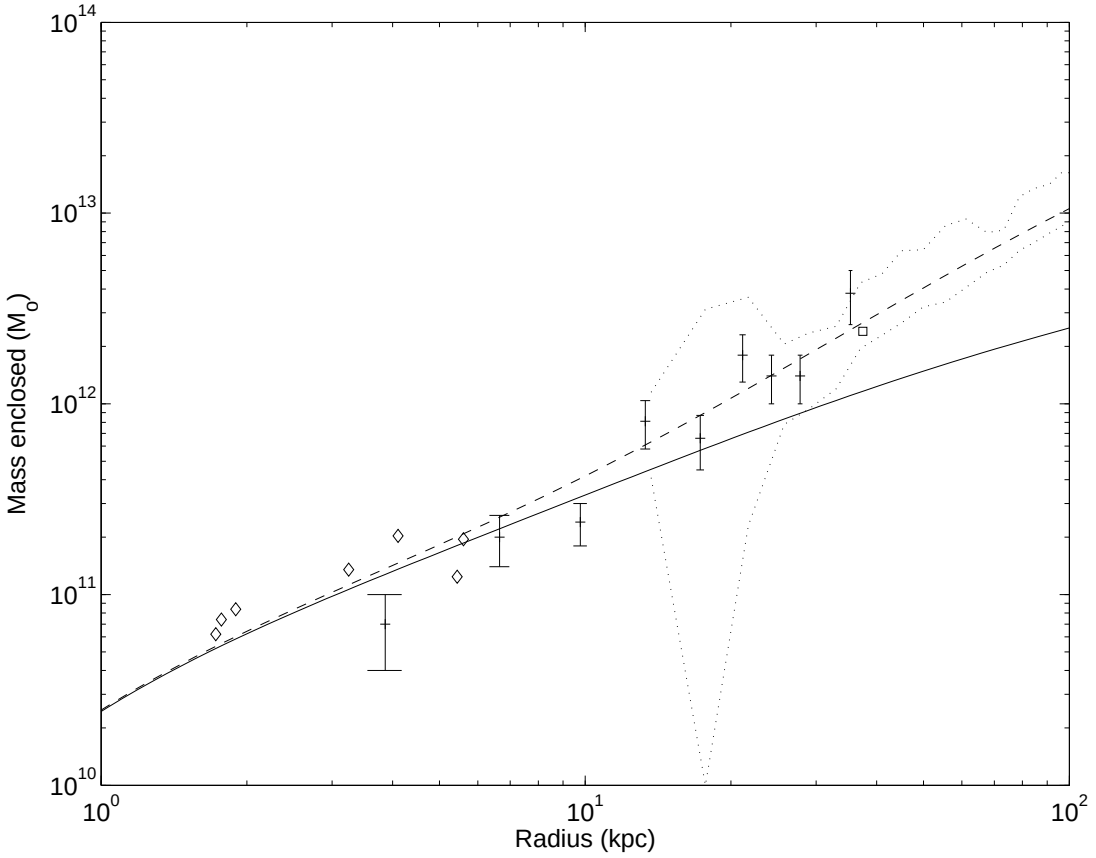


Figure 2.11: Comparison of mass models to existing data. Data are from stellar kinematics (Sargent et al. 1978, diamonds), globular cluster kinematics (Cohen & Ryzhov 1997, crosses with errors and Mould et al. 1990, single square point) and X-ray gas (Nulsen & Bohringer 1995, dotted lines show upper and lower mass limits). The solid line shows the best-fit model to the new stellar kinematic data. The dashed line shows an alternative, high-mass model that also fits the new data.

the black hole mass was expected due to the spatial resolution limit imposed by atmospheric seeing.

The two component model gave $\Upsilon = 5.34 \pm 0.34, \beta = 0.71 \pm 0.03$ for the stellar component and $M_{\rm halo} = 2.64 \pm 0.92 \times 10^{12}\, M_\odot$ for the mass of the dark halo. The model did not fit the planetary nebulae data in the outer region, nor did it agree with X-ray gas mass estimates. The poor fit is likely to be due to the simplicity of the model, since neither the mass-to-light ratio nor the anisotropy are permitted to vary with radius. An alternative model was constructed with radial orbits in

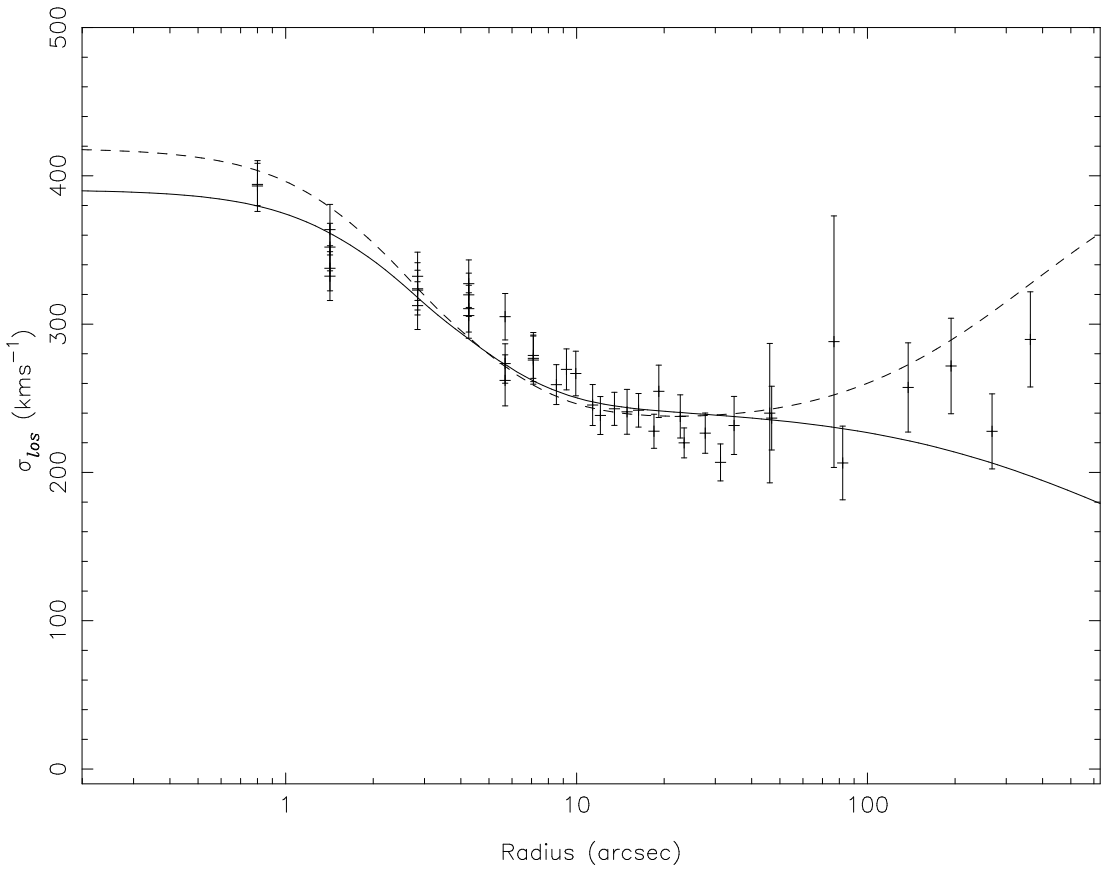


Figure 2.12: The dashed line shows the velocity dispersion profile of an alternative mass model ($M_{\rm halo} = 7.6 \times 10^{13}\, M_{\odot}$ with tangential orbits in the outer regions). The best-fit model shown previously in Figure 2.10 is also included for reference (solid line).

the inner regions and tangential orbits further out, which was able to provide a reasonable fit to data across three orders of magnitude in radius.

This chapter provides an example of some of the problems faced when attempting to constrain galaxy mass distributions using stellar kinematics. Stellar kinematics cannot be obtained in the outer halo of elliptical galaxies and kinematics from discrete sources provide only limited information regarding the distribution of dark matter in this region. Even when reliable velocity dispersion measurements can be obtained, uncertainty in the distribution of stellar orbits prevents an accurate determination of the mass distribution. In the next chapter gravitational redshift is used to attempt to lift this mass-anisotropy degeneracy.

# Chapter 3

# A Statistical Approach to Measuring Gravitational Redshift

As the last chapter showed, measurements of a galaxy's mass distribution from stellar kinematics are limited by the degeneracy between the mass and the structure of the stellar orbits. In other words, it can be common for a velocity dispersion profile to be equally well fit by a range of different mass models. Although higher order moments of the line-of-sight velocity distribution can be used to help constrain orbital anisotropy (e.g. van der Marel & Franx 1993), they can be difficult to obtain reliably.

Gravitational redshift offers an independent method of directly probing a galaxy's mass distribution, without needing to consider its orbital structure. The theory behind gravitational redshift is rather straightforward. As a photon emerges from the potential well created by a large mass distribution it loses energy so that, to an observer outside the potential, it appears to be redshifted relative to the outer regions. In the Newtonian limit the velocity shift corresponding to the intrinsic gravitational redshift is determined directly from the potential (e.g. Landau & Lifshitz 1975)

$$v_{\rm grav}(r) = -\Phi(r)/c, \tag{3.1}$$

where $r$ is the radius from the centre of the potential, $c$ is the speed of light and $\Phi(r)$ is the potential defined such that $\Phi(r) \to 0$ as $r \to \infty$.

The observed gravitational redshift, $\overline{v}_{\rm los}(R)$, can then be found by integrating the

luminosity weighted redshift along the line of sight through the galaxy

$$I(R)\,\overline{v}_{\rm los}(R) = 2\int_0^\infty \nu(r)\,v_{\rm grav}(r)\,dz, \tag{3.2}$$

where $I(R)$ is the projected luminosity density, $\nu(r)$ is the intrinsic luminosity density and $z = \sqrt{r^2 - R^2}$. $R$ is the projected distance from the centre, while $r$ is the intrinsic physical radius. Measurements of the magnitude of this signal at a range of angular radii provide a direct measurement of the strength of the gravitational potential and hence the mass distribution. Formally, it is possible to solve Equation 3.2 for $v_{\rm grav}$ and hence $\Phi$ using an Abel transform of the observed $\overline{v}_{\rm los}$, directly analogous to Equation 2.3. In practice, this approach is not used since the calculation requires the differentiation of $v_{\rm grav}$, which leads to the amplification of noise in the velocity profile.

Unfortunately, the magnitude of the gravitational redshift for a typical elliptical galaxy is rather small when compared with the Doppler shifts associated with stellar motions. Over the range of radii that contain sufficient quantities of stellar light (typically 1 – 100 arcsec for galaxies within 20 Mpc), the projected gravitational redshift varies by only a few $\mathrm{km\,s^{-1}}$. The motions of the stars due to rotation on the other hand, can result in variations of a few hundred $\mathrm{km\,s^{-1}}$ across the extent of the galaxy. Fortunately, as will be shown later in this chapter, coherent rotation in a system in equilibrium can be distinguished from gravitational redshift by separating the antisymmetric (odd) and symmetric (even) components of the velocity profile.

There are some other effects which could lead to a spurious detection of a gravitationally redshifted core:

- Non-equilibrium motions.
  If a dwarf galaxy were in the process of merging with the target galaxy and its remains were still oscillating along the line of sight, the velocity near the centre could be greater than in the surrounding regions. Dusty disks, which have been found in the centre of many elliptical galaxies (Tran et al. 2001), could also produce a similar signature.

- Patchy dust in the central regions.
  If dust conspired to obscure just the approaching side of a rotating galaxy near its centre it could produce a similar signal to a gravitational redshift.

- Misaligned longslit.
  Stiavelli & Setti (1993) showed that in the case of longslit data, if the slit does not pass through the exact centre of the galaxy it would lead to an even component in the velocity profile. The effect is strongest in galaxies with steep rotation curves.

Careful target selection can reduce these problems (see Chapter 4 for details), but there is one feature common to all of these effects that allows them to be separated from a true gravitational redshift detection. Since Doppler shifts are equally likely to be caused by motion towards the observer, the above examples would all lead to an equal number of blueshifted cores, whereas gravitational redshifts by their very nature always result in redshifted cores. Therefore, while individual measurements may be biased by non-equilibrium motions or other effects, combining the sample offers a method for averaging out these effects leaving just the gravitational redshift signal.

This approach was taken by Stiavelli & Setti (1993), who claimed to have detected a gravitational redshift from a sample of longslit data. In this chapter the same data are fitted using an extension of the models described in Chapter 2, in order to critically reassess their result and to see if this approach can significantly constrain galaxy mass distributions.

## 3.1 The Sample

Stiavelli & Setti's sample consisted of 58 radial profiles from 23 galaxies. The sample was obtained from the literature by selecting kinematic data with error bars smaller than $10\,\mathrm{km\,s^{-1}}$. Position angles with steep rotation curves were rejected, since it was shown that they can produce similar looking artifacts if the slit is not correctly centred on the galaxy. Of the 58 profiles used, 24 were found to have statistically significant central shifts at more than the $1\sigma$ level. Of them, 21 were redshifted while just three were blueshifted. Such a distribution would only be expected to occur by chance in 0.01 per cent of cases. Even if the error bars were underestimated by a factor of 2.5 (which is very unlikely), the probability would still be 1 per cent.

Although this result was intriguing, Stiavelli & Setti did not extend their work to attempt to obtain an insight into the global mass distribution of the sample.

| Object | Photometry | | | | | | Kinematics | | Distance |
|---|---|---|---|---|---|---|---|---|---|
| | Source | $\mu_b$ | $r_b$ | $\alpha$ | $\beta$ | $\gamma$ | Source | PAs | ( Mpc) |
| NGC1052 | R01 | 11.91 | 0.40 | 1.05 | 1.43 | 0.11 | DB | 1 | 19.4 |
| NGC3379 | R01 | 12.80 | 1.58 | 1.82 | 1.45 | 0.18 | DB | 3 | 10.6 |
| NGC4261 | R01 | 13.58 | 1.62 | 2.38 | 1.43 | 0.00 | DB | 4 | 31.6 |
| NGC4278 | R01 | 12.80 | 0.97 | 1.63 | 1.39 | 0.02 | DB | 3 | 16.1 |
| NGC4291 | R01 | 12.31 | 0.48 | 2.07 | 1.48 | 0.02 | JS | 1 | 26.2 |
| NGC4374 | R01 | 13.35 | 2.39 | 2.15 | 1.50 | 0.13 | DB | 4 | 18.4 |
| NGC4406 | R01 | 12.98 | 1.00 | 3.31 | 1.16 | 0.00 | JS | 1 | 17.1 |
| NGC4472 | R01 | 13.52 | 2.63 | 1.89 | 1.29 | 0.04 | DB | 4 | 16.3 |
| NGC4636 | R01 | 14.60 | 3.44 | 1.69 | 1.56 | 0.13 | DB | 4 | 14.7 |
| NGC7626 | R01 | 13.24 | 0.59 | 1.84 | 1.30 | 0.36 | JS | 2 | 45.4$^\dagger$ |

Table 3.1: The data sample. Sources of data: DB: Davies & Birkinshaw (1988); JS: Jedrzejewski & Schechter (1989); R01: Ravindranath et al. (2001). Distances from Tonry et al. (2001) except $^\dagger$ which was estimated from its redshift given in RC3 (de Vaucouleurs et al. 1991). $\alpha$, $\beta$, $\gamma$, $r_b$ (arcsec) and $\mu_b$ (mag arcsec$^{-2}$) are parameters of the Nuker law profile defined in Equation 2.2.

If a constant mass-to-light ratio is assumed, it is possible to use photometry to predict the magnitude of gravitational redshift expected and compare with the observed signal. Due to the size of the error bars in comparison with the expected signal, it is unlikely that any single galaxy will provide a convincing detection. Taken together however, the sample may constrain the mean mass-to-light ratio of the sample.

The galaxy models developed in Chapter 2 were extended to predict the gravitational redshift of a given mass distribution. Since the density profile is determined from the galaxy's light profile, it is vital to have consistent photometry of the target galaxies. Infrared observations are preferred since they are less affected by dust obscuration and contamination from gas and young stars, so they are more likely to accurately trace the galaxy's stellar mass. High spatial resolution photometric data are also required to produce an accurate model for the predicted gravitational redshift signal even if the kinematic data being modelled are relatively low-resolution ground-based observations. Therefore a subsample of the galaxies used by Stiavelli & Setti were selected for which $H$-band HST photometry was available.

The galaxies selected in this way are shown in Table 3.1. It should be noted that from the original sample of 23 galaxies, one galaxy gave a blueshifted core and

another gave a mixture of redshifts and blueshifts. Neither of these galaxies were included in this work because of a lack of $H$-band photometry.

In order to correctly estimate the mass-to-light ratios, the absolute distance to the galaxy must be known. The distances were taken from the surface brightness fluctuation measurements of Tonry et al. (2001), except for `NGC7626` which was not included in that sample. For `NGC7626` the distance was estimated using its systemic redshift assuming a Hubble constant of $H_0 = 75\,\mathrm{km\,s^{-1}\,Mpc^{-1}}$.

## 3.2 Fitting to the Data

### 3.2.1 Extracting the Even Velocity Component

In order to measure the gravitational redshift, the effect of galaxy rotation must be removed from the velocity profiles. This is done by extracting the even component of the velocity using the following procedure:

1. Radial bins were generated using an adaptive bin size. Starting from the centre, each bin was added beginning with a minimum size of 1 arcsec. If the bin did not contain at least one data point on either side of the galaxy, its size was doubled until it did.

2. The data in each bin were combined (in both radius and velocity) by taking the error weighted mean

$$\langle v \rangle = \frac{\sum_i v_i/\sigma_i^2}{\sum_i 1/\sigma_i^2}, \tag{3.3}$$

   where $v_i$ are the data points to be combined and $\sigma_i$ the errors on each point. The error on the resulting point $\langle v \rangle$ is given by

$$\sigma^2(\langle v \rangle) = \frac{1}{\sum_i 1/\sigma_i^2}. \tag{3.4}$$

   This resulted in one data point per bin, on either side of the galaxy's centre.

3. These two points were then combined by taking the mean of the two values. The new error was calculated by assuming both points had errors equal to the larger of the two errors (therefore $\sigma(\langle v \rangle) = \sigma_{\mathrm{largest}}/\sqrt{2}$).

This approach was taken as it was found that the error weighted mean was not robust in cases where the size of the error bars was not symmetric and the profile contained significant rotation.

4. The centre of each bin was used to mark the radial position of the new data point. Radial binning was also considered and was found to result in a slight shift in the centre of the bin (typically $< 1$ arcsec). Because of the slow change in gravitational redshift as a function of radius the results would not be significantly affected.

To illustrate this process, Figure 3.1 shows the result for `NGC4621`. The data for a single slit position are shown as open triangles. The direction of the triangle indicates the side of the galaxy. The even component that results is indicated with the filled circles. The dotted lines show the boundaries of the bins.

### 3.2.2 Calculating Galaxy Mass-to-Light Ratios

The magnitude of the gravitational redshift was calculated assuming that the galaxies had a constant mass-to-light ratio, using the methodology developed in Chapter 2. Equation 2.3 was used to deproject the luminosity density, then the potential $\Phi(r)$ was calculated using Equations 2.9 and 2.10.

The best-fit mass-to-light ratio for each galaxy was obtained by minimising $\chi^2$ between the even component of the mean velocity and the model. If the galaxy has several slit positions, the model was fit to data from all of the slit positions simultaneously.

$\chi^2$ was calculated using the usual formula,

$$\chi^2 = \sum_i \frac{(v_{di} - v_{mi})^2}{\Delta_{di}^2}, \tag{3.5}$$

where $v_{di}$ is the value of the $i$th data point, $\Delta_{di}$ is the error associated with it and $v_{mi}$ is the model value at the same radius. Since the systemic velocity of the galaxy is determined by its intrinsic redshift, this quantity was also left as a free parameter in the fitting process, removing one additional degree of freedom. Formal errors on individual $\Upsilon_H$ values are calculated by determining the range of mass-to-light ratios for which $\chi^2 \leq \chi^2_{\rm min} + 1$.

The gravitational redshift models indicate that the most significant change in the observed redshift occurs in the central few arcseconds. It could be expected that the outer region contains little useful signal and hence the results would improve by considering only the kinematics from the very centre. For this reason the stellar kinematics were divided into three samples – one contained all the data, while the other two contained only the data points from within 10 and 20 arcsec of the centre. The best-fit mass-to-light ratios for each sample were determined individually using the method described above (see Table 3.3 for the results).

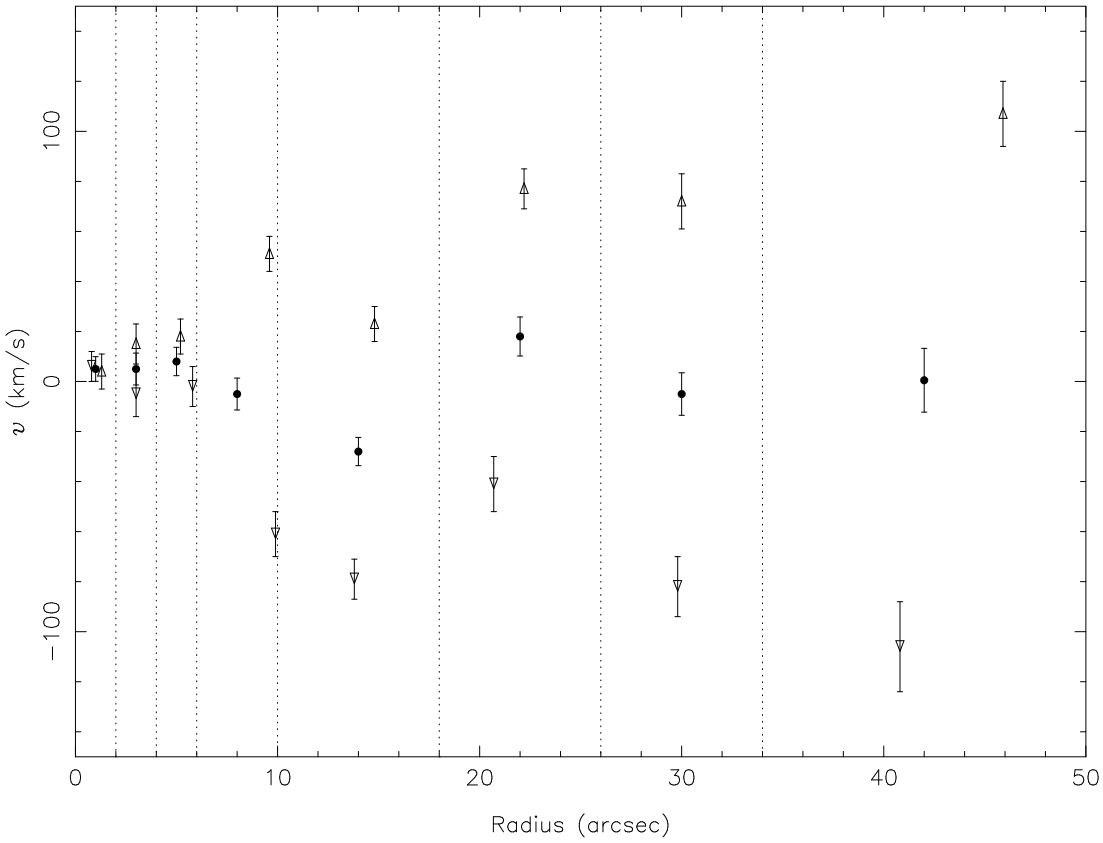


Figure 3.1: Extracting even velocity components. The different open triangles show the original mean line-of-sight velocity data on different sides of the centre of the galaxy for a single slit position of NGC4261. Data with negative radii have been mirrored. The filled circles show the even component of the profile. The dotted lines indicate the bin boundaries used to combine the data.

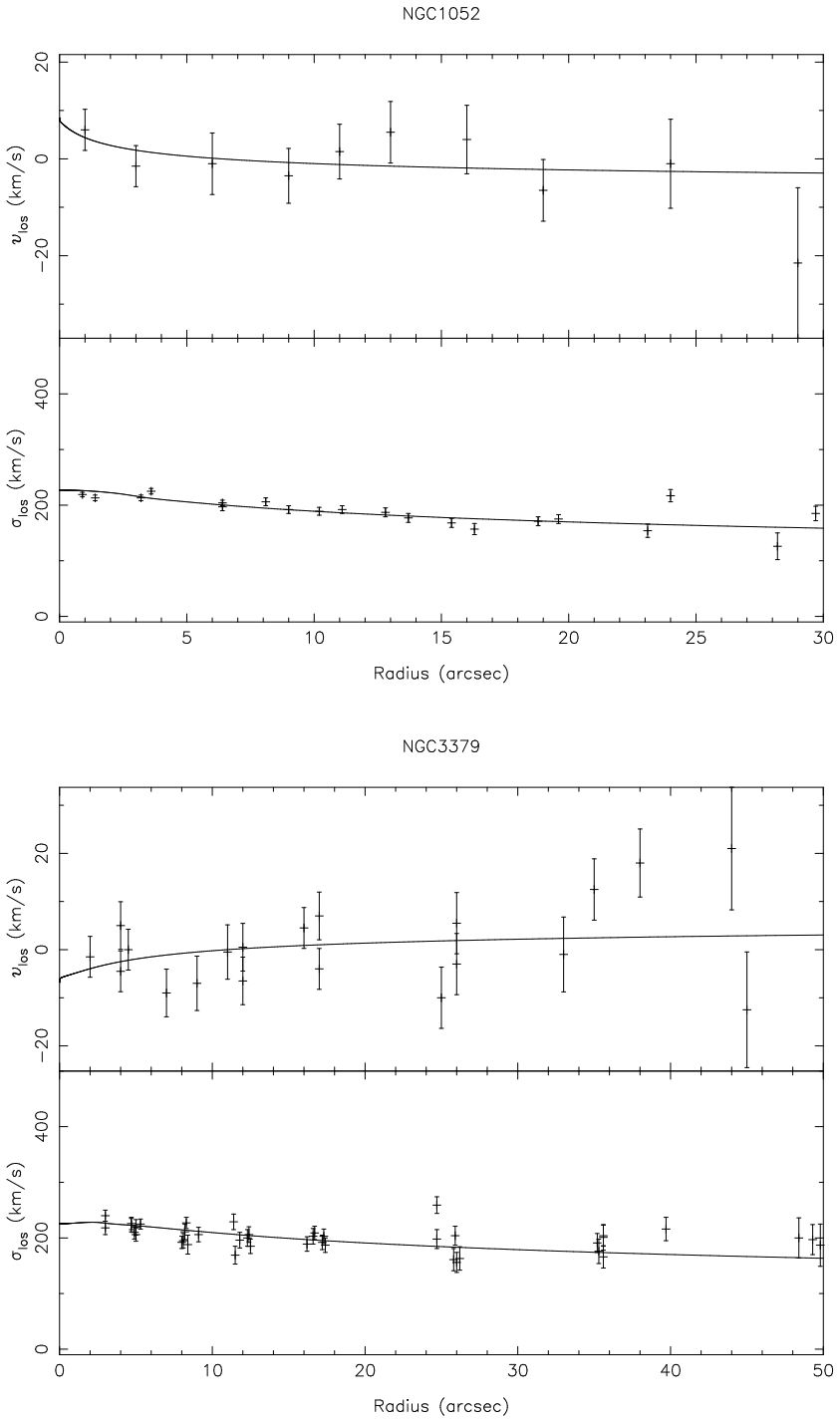


Figure 3.2: Best model fits to the data from the sample. Above: NGC1052 and NGC3379. The top panel shows the fit to the even component of the velocity, the bottom panel shows the fit to the velocity dispersion.

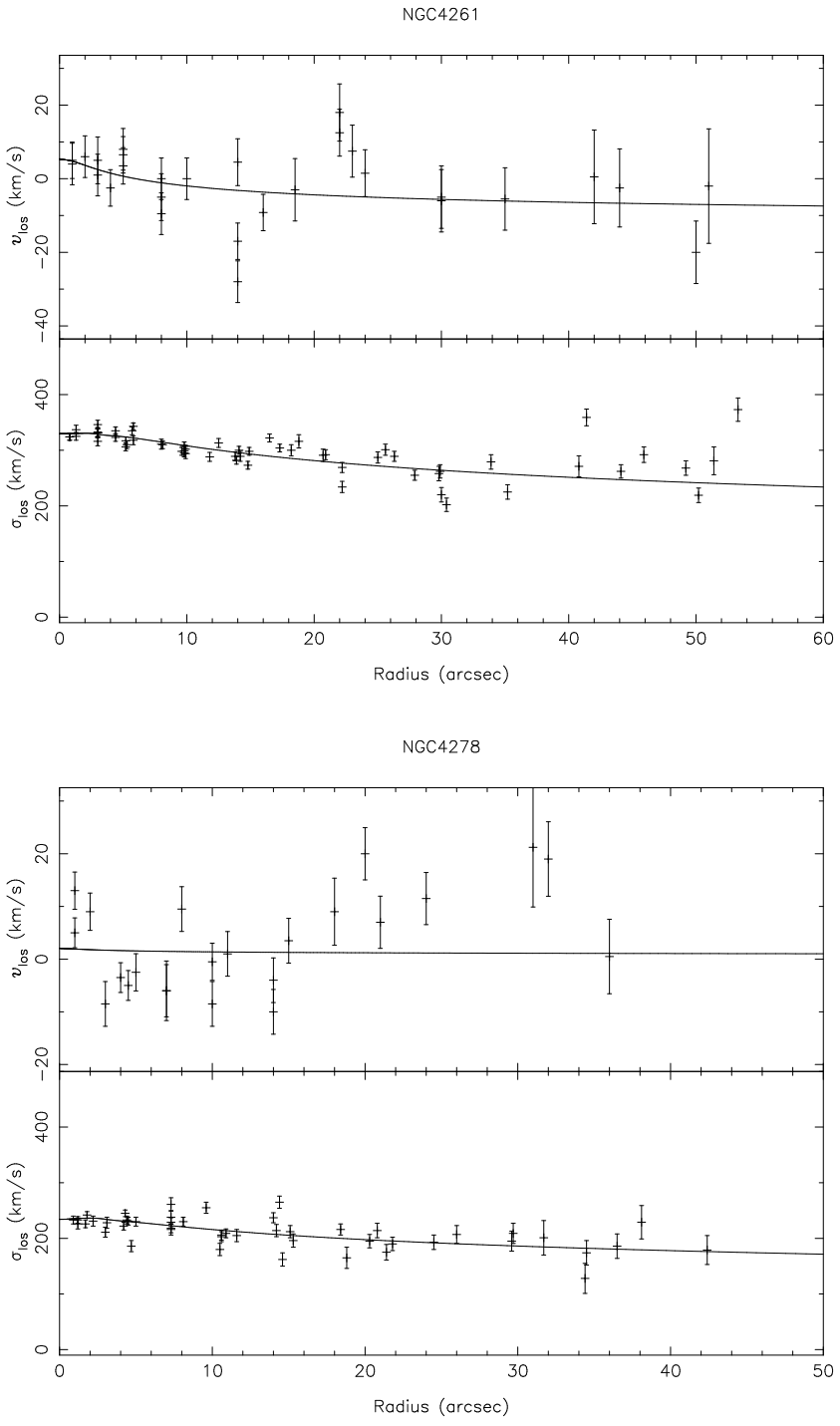


Figure 3.2: Continued: NGC4261 and NGC4278.

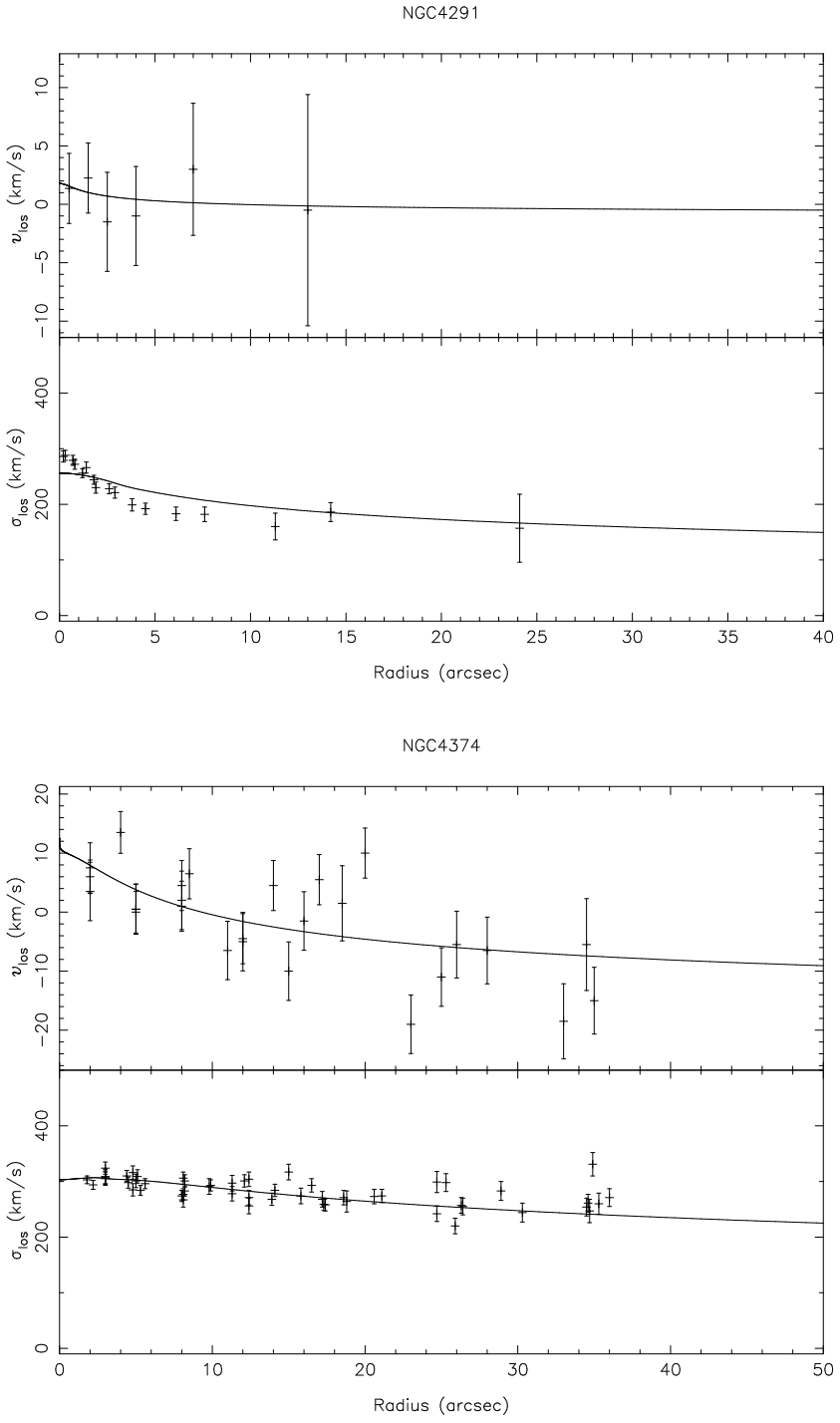


Figure 3.2: Continued: NGC4291 and NGC4374.

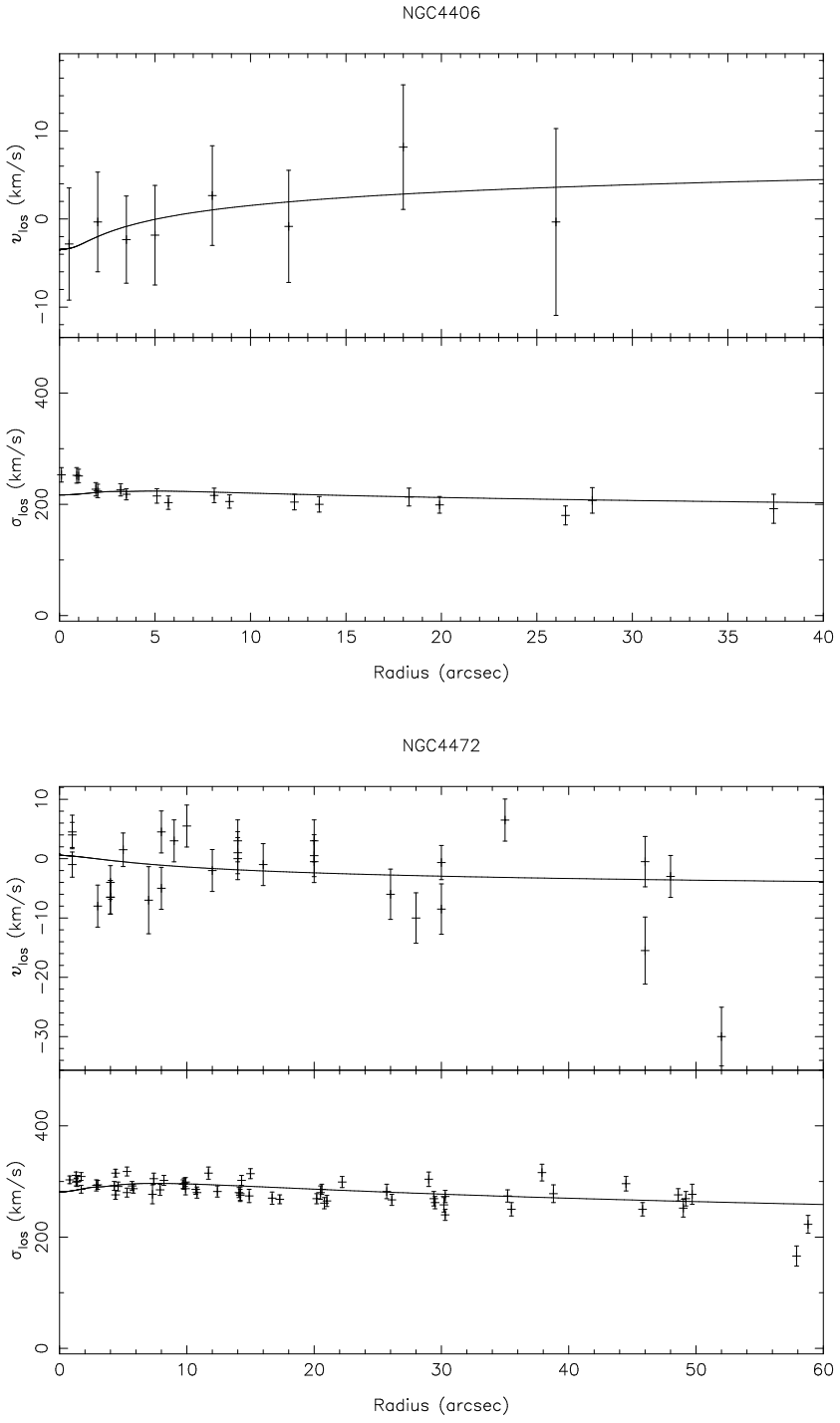


Figure 3.2: Continued: NGC4406 and NGC4472.

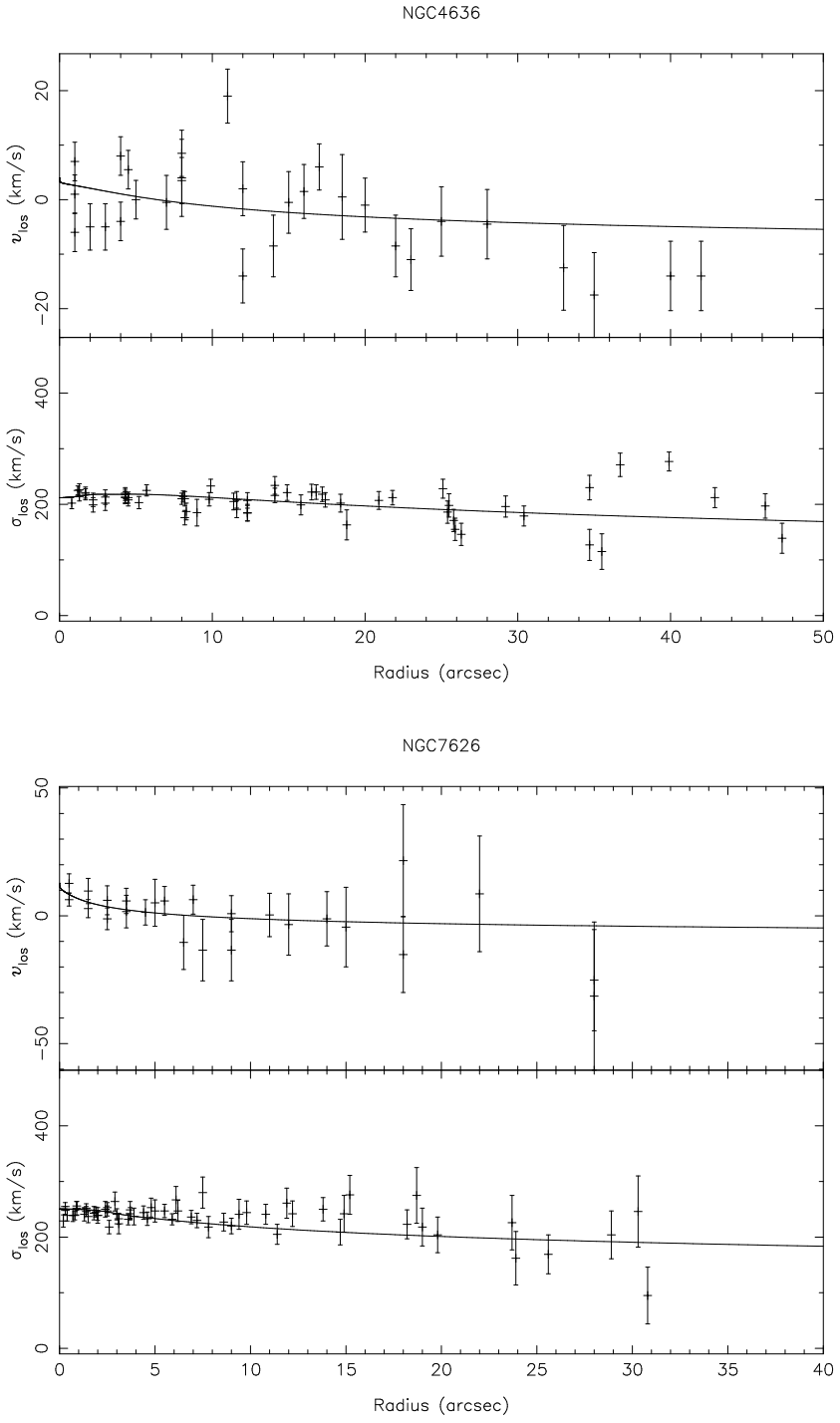


Figure 3.2: Continued: NGC4636 and NGC7626.

The velocity dispersion profile was used to independently determine the mass-to-light ratio, using the Jeans equation as described in Chapter 2. For this simple model only the isotropic case was considered. In most cases this was sufficient to provide a reasonable fit to the velocity dispersion profile, although a few of the targets (particularly NGC4291 and NGC4406) the fit would be improved if some anisotropy was introduced in the central regions. Figure 3.2 shows the quality of the fit to the data for both the even component and the velocity dispersion.

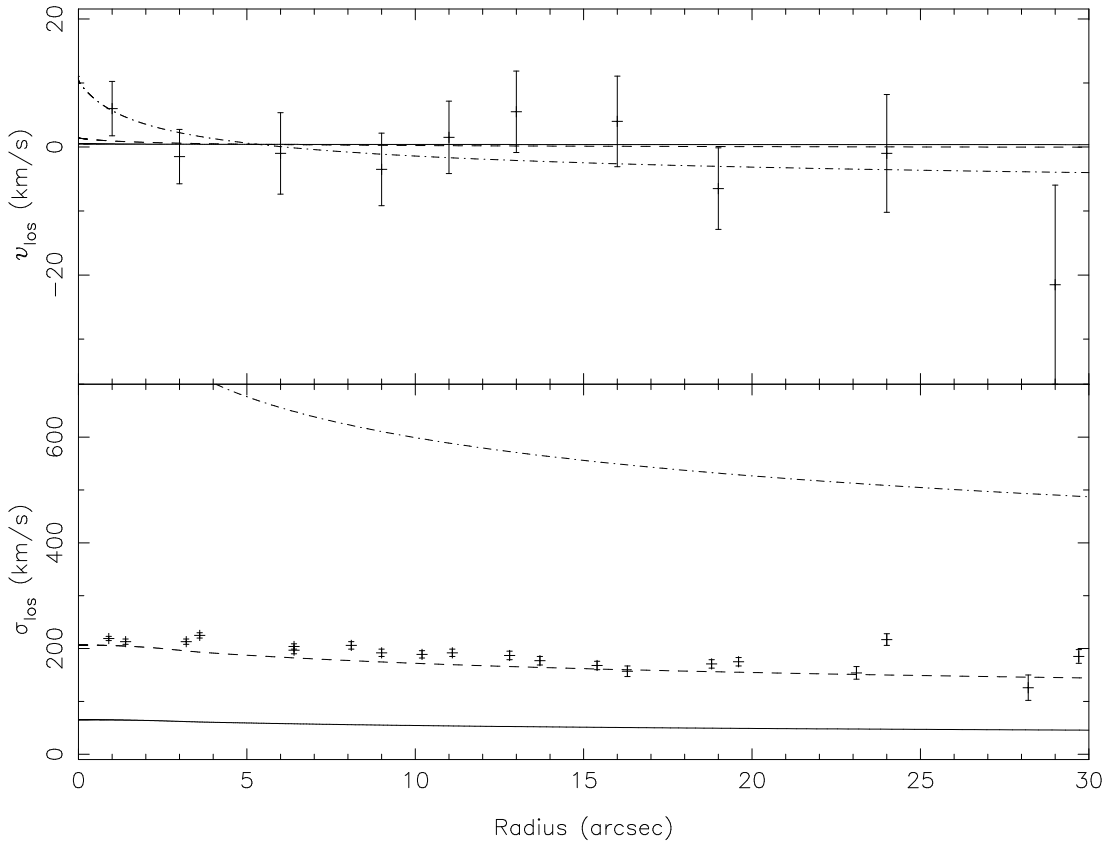


Figure 3.3: A range of mass models plotted with the data for NGC1052. The lines correspond to models with $H$-band mass-to-light ratios of 0.1 (solid line), 1 (dashed line) and 10 (dot-dashed line).

Figure 3.3 shows the variation in the model profile for mass-to-light ratios $\Upsilon_H \in (0.1, 1, 10)$ obtained from both gravitational redshift predictions and by solving the Jeans equation assuming isotropic orbits. The concentration of the predicted gravitational redshift signal towards the inner regions discussed above is clear from the top panel, as is the small amplitude of the predicted signal.

The large extent of the error bars clearly make it impossible to confirm a positive detection for the case of a single galaxy. Although some galaxies do appear to contain a central shift, there are also signs of sinusoidal residuals at a similar magnitude to that of the expected signal, which may be an artifact introduced when splitting the velocity profile into odd and even components.

### 3.2.3 Obtaining a Mean Mass-to-Light Ratio

As discussed previously, the mass-to-light ratio for individual galaxies can be unreliable, since they are easily affected by a number of effects that appear similar to gravitational redshift (non-equilibrium motions, miscentred longslit, etc.). The mean of the individual $\Upsilon_H$ values was taken to provide an overall mass-to-light ratio for the sample. This value should offer a more robust determination of the overall mass-to-light ratio of the sample, since redshifts *and* blueshifts that are not due to gravitational redshift will tend to average out. The error on the mean mass-to-light ratio, $\overline{\Upsilon}$, was calculated based on the spread of the means by invoking the central limit theorem to give

$$\Delta\Upsilon_H = \frac{\sqrt{\sum_i (\Upsilon_i - \overline{\Upsilon})^2}}{N-1}, \tag{3.6}$$

where $\Upsilon_i$ is the mass-to-light ratio of the $i$th sample member and $N$ the number of objects in the sample.

## 3.3 Results

### 3.3.1 Comparison of Mass-to-Light Ratio Results from Different Models

Table 3.2 compares the results obtained by the two methods. The mean results for the whole sample ($\overline{\Upsilon}_\sigma = 1.67 \pm 0.10\, M_\odot/L_{\odot H}$ and $\overline{\Upsilon}_v = 4.84 \pm 2.67\, M_\odot/L_{\odot H}$) have uncertainties which are too large to rule out the hypothesis that the two mass-to-light ratios are the same.

The gravitational redshift method resulted in a much larger scatter in the individual galaxy mass-to-light ratios than the velocity dispersion measurements.

| Object | $v_{\rm grav}$ | | | $\sigma$ | | |
|---|---|---|---|---|---|---|
| | N | $\chi^2_{\rm min}$ | $\Upsilon_H$ | N | $\chi^2_{\rm min}$ | $\Upsilon_H$ |
| NGC1052 | 10 | 5.06 | $7.43 \pm 6.00$ | 20 | 54.7 | $1.22 \pm 0.02$ |
| NGC3379 | 20 | 27.9 | $-8.63 \pm 5.41$ | 42 | 73.2 | $1.44 \pm 0.03$ |
| NGC4261 | 29 | 59.8 | $8.95 \pm 3.12$ | 60 | 312.0 | $2.11 \pm 0.02$ |
| NGC4278 | 23 | 84.4 | $0.76 \pm 3.41$ | 48 | 155.0 | $1.56 \pm 0.02$ |
| NGC4291 | 6 | 0.81 | $1.81 \pm 6.03$ | 17 | 74.8 | $1.64 \pm 0.03$ |
| NGC4374 | 27 | 50.1 | $14.0 \pm 2.54$ | 54 | 106.5 | $1.72 \pm 0.02$ |
| NGC4406 | 8 | 1.27 | $-8.63 \pm 9.43$ | 19 | 34.8 | $1.44 \pm 0.04$ |
| NGC4472 | 30 | 85.2 | $3.51 \pm 1.60$ | 62 | 206.5 | $1.67 \pm 0.01$ |
| NGC4636 | 30 | 67.3 | $18.0 \pm 6.53$ | 60 | 141.4 | $2.36 \pm 0.04$ |
| NGC7626 | 25 | 15.2 | $11.2 \pm 3.87$ | 63 | 60.6 | $1.55 \pm 0.02$ |
| Average | | | $4.84 \pm 2.67$ | | | $1.67 \pm 0.10$ |

Table 3.2: Best-fit constant mass-to-light ratio models obtained from the even velocity component ($v_{\rm grav}$) and the velocity dispersion ($\sigma$). Columns show the number of data points used in the fit (N), the value of $\chi^2$ for the best-fit model ($\chi^2_{\rm min}$) and the value of the best-fit $H$-band mass-to-light ratio ($\Upsilon_H$). Also shown are the average mass-to-light ratios for both models. The negative values for NGC3379 and NGC4406 indicate that the best-fit gave a *blueshift* rather than a redshift.

Two galaxies (`NGC3379` and `NGC4406`) resulted in blueshifts, although both are essentially consistent with having no shift within the formal error. Stiavelli & Setti found no evidence of any signal in those two galaxies. Differences such as this in the significance of central shifts found by the two methods suggests that the results are sensitive to the exact method used to extract the even component of the velocity, a result which is undesirable as well as perplexing. Unfortunately, Stiavelli & Setti did not elaborate on how they extracted the even component so our methods could not be directly compared.

The formal error bars on the mass-to-light ratio results obtained from $v_{\rm grav}$ are also consistently larger than those obtained from the velocity dispersion. The reason for this is obvious from Figure 3.3. Because the galaxy's systemic velocity is a free parameter in the fit, the velocity models have an extra degree of freedom that allows the data to be fit by a much wider range of mass models than is possible for the velocity dispersion.

Consideration of $\chi^2_{\rm min}$ (the value of $\chi^2$ for the best-fit models) suggest that the models are a poor fit to the data, since many of the fits give results that lie outside 99.5% of the $\chi^2$ distribution. Visual inspection however, suggests the majority

of the models do provide a good fit to the data. For example, consider the fit to the velocity dispersion for NGC4261 in Figure 3.2. The fit indicates $\chi^2 = 312.0$, but it is clear that in the outer regions no smooth curve could provide a good fit to the data. By eye the model does indeed appear to fit the data well. This suggests that the error bars on the stellar kinematics in the literature have been underestimated.

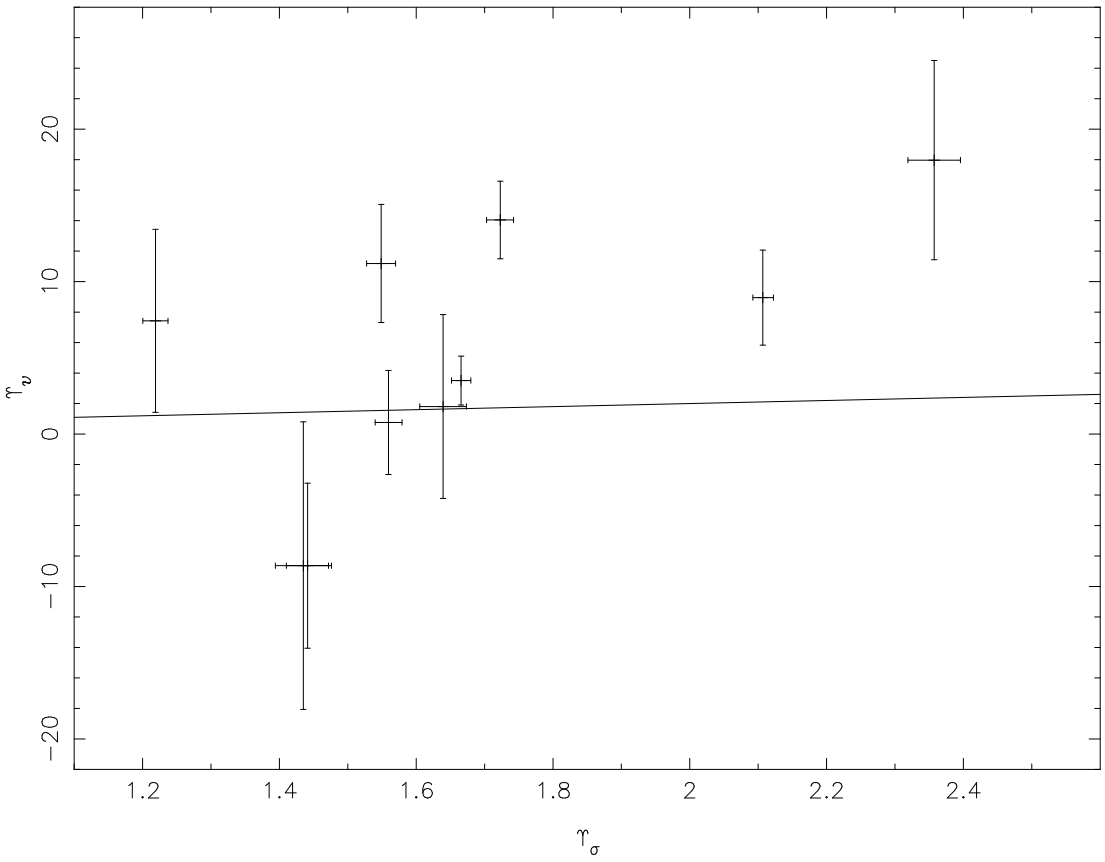


Figure 3.4: Comparison between the mass-to-light ratios obtained from the mean velocity ($\Upsilon_v$) and velocity dispersion ($\Upsilon_\sigma$). The solid line shows the line of equality between the two models.

The mass-to-light ratios obtained from the mean velocity ($\Upsilon_v$) and velocity dispersion ($\Upsilon_\sigma$) are compared directly in Figure 3.4. The plot appears to show some hint of a positive correlation. If both methods were accurately measuring the mass-to-light ratio then the points would be expected to follow the line of equality, not show a positive slope. This may indicate that $\Upsilon_v$ is not an accurate measure of the mass-to-light ratio for this sample. Regardless of whether or

not this is the case, the error bars are rather too large to draw any meaningful conclusions about the mass distribution.

| Object | All | | $< 20''$ | | $< 10''$ | |
|---|---|---|---|---|---|---|
| | $v_{grav}$ | $\sigma$ | $v_{grav}$ | $\sigma$ | $v_{grav}$ | $\sigma$ |
| NGC1052 | 7.43 | 1.22 | 6.31 | 1.21 | 13.9 | 1.21 |
| NGC3379 | -8.63 | 1.44 | -3.50 | 1.40 | 19.1 | 1.40 |
| NGC4261 | 8.95 | 2.11 | 19.5 | 2.10 | 11.8 | 2.08 |
| NGC4278 | 0.76 | 1.56 | 13.7 | 1.56 | 23.7 | 1.56 |
| NGC4291 | 1.81 | 1.64 | 1.81 | 1.64 | 1.71 | 1.64 |
| NGC4374 | 14.0 | 1.72 | 9.84 | 1.70 | 6.86 | 1.67 |
| NGC4406 | -8.63 | 1.44 | -10.3 | 1.45 | -7.52 | 1.48 |
| NGC4472 | 3.51 | 1.67 | -0.60 | 1.70 | 5.84 | 1.73 |
| NGC4636 | 18.0 | 2.36 | -7.80 | 2.31 | -27.5 | 2.28 |
| NGC7626 | 11.2 | 1.55 | 10.4 | 1.55 | 10.2 | 1.54 |
| Mean | 4.84 | 1.67 | 3.95 | 1.66 | 5.80 | 1.66 |
| Error on mean | 2.67 | 0.10 | 2.90 | 0.10 | 4.38 | 0.95 |

Table 3.3: $\Upsilon_H$ calculated using different samples of data (The full sample, the central $20''$ only and the central $10''$ only). Negative values indicate that the best-fit gave a *blueshift* rather than a redshift.

As discussed previously, as well as fitting models to the full range of stellar kinematics, the models were fit to a restricted radial range in order to see if the outer points were simply adding noise without contributing to the signal. Table 3.3 shows how the $\Upsilon_H$ values changed depending on the data sample used. Three cases were considered: the full data sample, kinematics from the inner $20''$ only and kinematics from the inner $10''$ only. Within the errors, none of the mass-to-light ratios varied depending on the sample, although the errors do increase significantly in the case of the velocity data. It seems that the reduced number of data points makes it increasingly difficult to obtain an accurate zero-point from which to determine the gravitational redshift. Overall there does not appear to be any advantage to be gained from limiting the range of stellar kinematics used in the analysis.

## 3.4 Discussion

One obvious question is whether these results are consistent with the expected mass-to-light ratios of the luminous stellar population, or whether a dark matter

component is either required or can be ruled out. The average mass-to-light ratio obtained was compared to $H$-band values from stellar population models. Worthey (1994) models with a Salpeter IMF over the mass range $0.2 - 10\,M_{\odot}$ gave $H$-band mass-to-light ratios in the range of $0.6 - 0.8$ for a range of possible ages, metallicities and IMF slopes. Unimodal SSP models from Vazdekis et al. (1996) give $\Upsilon_H \sim 0.9$ for an IMF slope of 2.3, solar metallicity and an age of $10 - 13$ GYr. For a steeper slopes (2.8) the predicted $\Upsilon_H$ is $\sim 1.5$.

Given the uncertainty in both the observed mean mass-to-light ratio and the predictions from stellar population models, the velocity dispersion results cannot rule out a stellar-only population with no dark matter. The mass-to-light ratio from the velocity measurements were rather high but given the larger errors it is not inconsistent with the velocity dispersion result.

Table 3.2 shows that the sample contains an excess of redshifted cores, in broad agreement with the result of Stiavelli & Setti. Given the size of the error bars and the predicted magnitude of the gravitational redshift signal from the model in this work, it seems unlikely that a measurement of the true gravitational redshift has been made at the level of significance claimed by Stiavelli & Setti.

Although the results obtained are not accurate enough to provide any strong constraints on the mass distribution in the sample there are still reasons to be optimistic about using gravitational redshift to probe elliptical galaxy mass distributions. The kinematic data used in this chapter was obtained almost 15 years ago and had error bars of $\sim 10\,\mathrm{km\,s^{-1}}$. Given the small magnitude of this effect it is unsurprising that the results could not easily be constrained.

One method of further constraining the mass-to-light ratio would be to increase the size of the galaxy sample. Even using data with $10\,\mathrm{km\,s^{-1}}$ error bars, increasing the sample size to 64 galaxies would allow the current result to be ruled out at the $3\sigma$ level (assuming the errors scale as $\sqrt{N}$).

Rather than simply trying to combine larger quantities of longslit data, an alternative approach would be to obtain higher quality data for a single galaxy. Many of the difficulties faced in this chapter are due to the large error bars and limited spatial information provided by longslit spectroscopy. Integral field spectroscopy provides full spatial coverage, so that even components due to slit misalignment would not occur. Small scale bulk streaming motions would be visible in the velocity field as coherent streams; either they could be rejected outright, or their effect

would be greatly diluted by summing the signal around the galaxy's isophotes.

In the next chapter a pilot study is described, where integral field spectroscopy was used to observe the centre of a bright elliptical galaxy in an attempt to make the first detection of gravitational redshift.

# Chapter 4

# Integral Field Spectroscopy of M60

This chapter describes integral field spectroscopy of M60 (NGC4649) designed to detect for the first time a gravitational redshift at the centre of an individual galaxy. This proof of concept study aims to assess the viability of measuring 2D velocity fields at the accuracy required for a positive detection. Recent developments in 2D spatial binning are tested and a new method for the extraction of the even velocity component for 2D data is developed.

## 4.1 Target Selection and Observation

### 4.1.1 Selection Criteria

The models developed in Chapter 3 provided a quantitative measure of the magnitude and form of the predicted gravitational redshift for a galaxy-mass object. This information was used to select a range of candidates where the effect could be most easily observed. Several additional criteria were considered when selecting possible target galaxies:

1. High surface brightness.
   In order to measure the centre of a line to the required accuracy of $1\,\mathrm{km\,s^{-1}}$, extremely high signal-to-noise ratio spectra are required (particularly as high spectral resolution is also important).

2. Centrally concentrated.

Centrally cusped light profiles increase the signal in the inner region and also result in a larger gravitational redshift signal.

3. High measured central velocity dispersion.
   Also an indication of mass and hence a larger gravitational redshift.

4. Existing longslit spectra show 'normal' rotation curve.
   The literature was searched for existing kinematic data in order to get some idea of the complexity of the central kinematics. Only galaxies with smooth, symmetric rotation curves were considered. In particular galaxies with signs of kinematically distinct cores or rapidly rotating central disks were rejected.

5. No sign of central dust.
   Patchy dust in a rotating galaxy could potentially be interpreted as a central redshift, if the dust conspired to obscure only the receding side of the galaxy in the outer regions. The literature was searched for studies of dust and disks in the centres of elliptical galaxies. The galaxies selected showed no sign of significant amounts of patchy dust obscuration.

6. No central emission.
   Weak central emission could alter the shape of absorption features, altering the mean velocity at a magnitude similar to that of a gravitationally redshifted core. Since emission arising from active nuclei and central star-forming regions is centrally concentrated, it could result in a gradient in the velocity field as a function of radius. Galaxies with observed central emission were excluded from the sample.

7. Not interacting.
   Photometry of possible galaxies was examined for evidence of recent mergers or interactions that could result in non-equilibrium motions in the galaxies' centre.

The combination of such a large number of constraints severely limited the sample of galaxies to choose from. Although elliptical galaxies have traditionally been considered as fairly featureless objects, it was found that most ellipticals are in some way peculiar. Nevertheless, a small sample of promising targets was found by excluding unsuitable targets from the RC3 catalogue (de Vaucouleurs et al.

1991). M60 (NGC4649) was selected as the primary target, while NGC5576, NGC5982 and NGC4621 were chosen as backup targets.

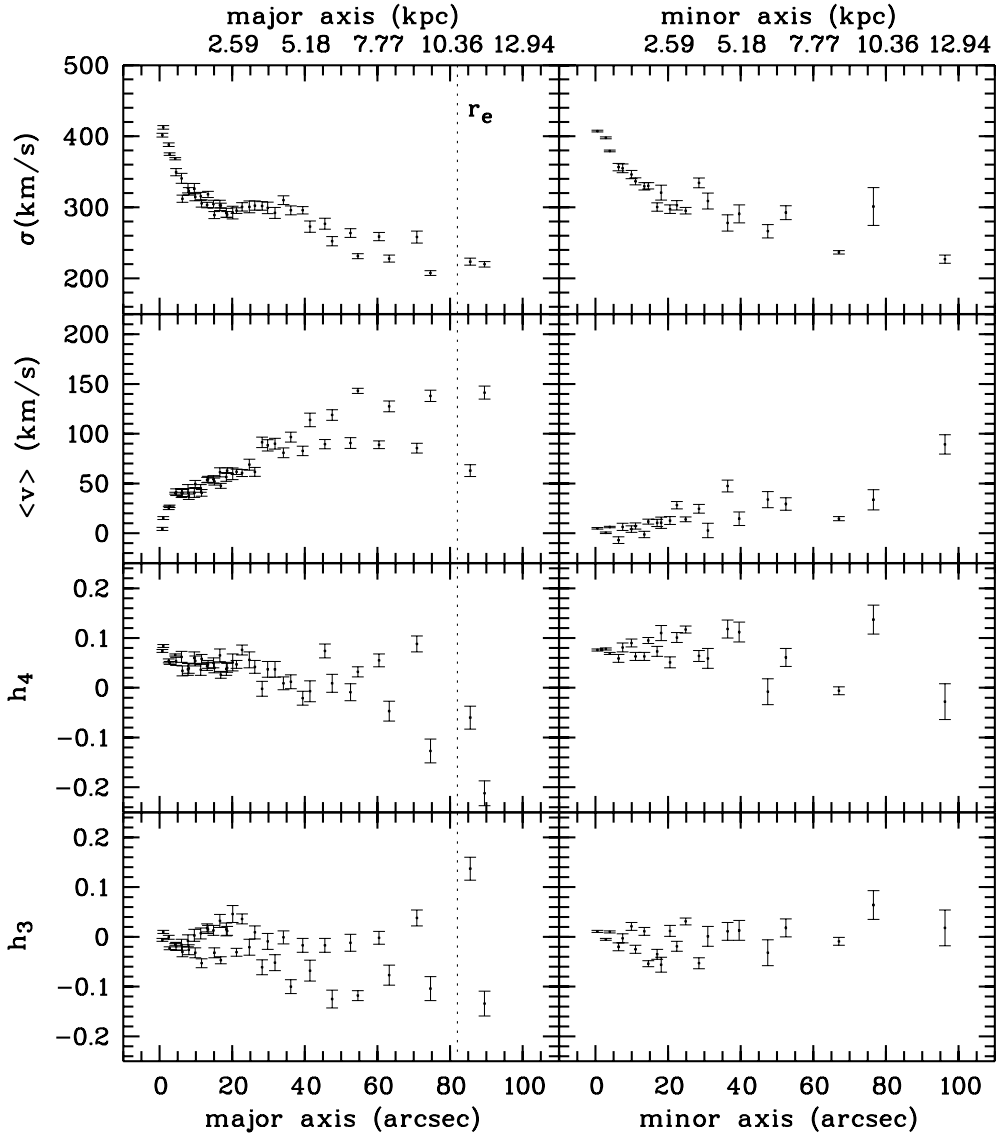


Figure 4.1: Major and minor axis longslit kinematics of M60 from De Bruyne et al. (2001) showing the symmetric rotation curves and large central velocity dispersion. Data are folded about the galaxy centre. The dotted line indicates a distance of one effective radius.

The preferred target, M60 is a luminous ($B_T$ magnitude 9.61, Prugniel & Heraudeau 1998) apparently round galaxy in the Virgo Cluster, at a distance of $16.5 \pm 0.6$ Mpc (Ferrarese et al. 2000). It is classified as an E1/E2 galaxy in the

Second Reference Catalogue of Bright Galaxies (de Vaucouleurs, de Vaucouleurs & Corwin 1976) and $S0_1$ in the Revised Shaply-Ames Catalog of Bright Galaxies (Sandage & Tammann 1987). Wide-field photometry has indicated an effective radius of 70 arcsec (5.6 kpc) (de Vaucouleurs et al. 1991) and slightly boxy isophotes outside $0.12R_e$ (Peletier et al. 1990). HST photometry by Byun et al. (1996) indicates a reasonable fit to a double power-law in its inner regions. Several studies (Lauer (1985), Veron-Cetty & Veron (1988), van Dokkum & Franx (1995)) have shown no evidence of a central disk component or any dust in the galaxy's nucleus. Previous longslit spectroscopy (Bender, Saglia & Gerhard (1994), Fried & Illingworth (1994), Fisher, Illingworth & Franx (1995), De Bruyne et al. (2001)) revealed smooth, symmetric rotation curves in the inner region with around $50\,\mathrm{km\,s^{-1}}$ rotation along the major axis and a few $\mathrm{km\,s^{-1}}$ along the minor axis. Data from De Bruyne et al. (2001) are shown in Figure 4.1. Spectroscopy also reveals an unusually high central velocity dispersion (up to $420\,\mathrm{km\,s^{-1}}$ in the centre falling to $300\,\mathrm{km\,s^{-1}}$ at a distance of 20 arcsec). Note the large discrepancy between the effective radius in Figure 4.1 ($R_e = 82$ arcsec $= 10.4$ kpc) and the value quoted above ($R_e = 70$ arcsec $= 5.6$ kpc). This is partly caused by a revision in the effective radius due to improved photometry, but is mainly because of a change in the distance estimate for `M60` (from 26.6 Mpc to 16.5 Mpc). $R_e = 70$ arcsec is used in this thesis since it is calculated from a more recent and reliable determination of distance. Visual inspection of photometry indicates one nearby companion, the spiral galaxy `NGC4647` 2.5 arcmin away, but there are no signs of any interaction between the two galaxies.

None of the other galaxies were found to be quite as suitable as `M60`. All of the alternatives were less luminous, with significantly lower central velocity dispersions. `NGC5576` has a smooth, symmetric rotation curve (Bender, Saglia & Gerhard 1994) and no sign of dust or central emission (Tran et al. 2001), but its position meant it could only be observed for half of the night. `NGC5982` has an oscillating velocity field (Wagner, Bender & Moellenhoff (1988), Statler (1991), Oosterloo, Balcells & Carter (1994)) and also shows some [O II] emission (Caldwell (1984), Bettoni & Buson (1987)). `NGC4621` revealed a symmetric, but rapidly rotating velocity field (Wagner, Bender & Moellenhoff (1988), Bender (1990), Bender, Saglia & Gerhard (1994)) and some evidence of a weak stellar disk (Lauer (1985), Bender (1990)).

Although M60 did not have a particularly steep inner light profile, it was the most suitable target in most other ways and its unusually large central velocity dispersion suggested a large associated mass.

### 4.1.2 Observational Setup

M60 was observed for two nights on 2001 March $19-20$, using INTEGRAL / WYFFOS on the WHT, La Palma. INTEGRAL is an integral field unit that feeds the WYFFOS spectrograph to allow spectra to be obtained over an extended 2D area of the sky (see Arribas et al. 1998). INTEGRAL is mounted on an optical bench at the GHRIL Nasmyth platform of the WHT, affording it extraordinary stability in comparison to Cassegrain mounted spectrographs. It contains a rotating swing plate mounted in the focal plane, which permits selection of a different fibre bundle with only a few seconds overhead. This allows the observations to be optimised to suit the prevailing seeing conditions. The SB1, SB2 and SB3 bundles offer a trade off between either high spatial resolution or large field of view and increased throughput. For this work the SB2 fibre bundle was used, which consists of 189 fibres of 0.9 arcsec diameter covering a rectangular field of view of $16.0 \times 12.3$ arcsec and an additional 30 sky fibres set in a ring of diameter 90 arcsec.

The fibres were fed into the WYFFOS spectrograph, which was set up in $5^{\text{th}}$ order echelle mode, giving a dispersion of $0.34\,\text{Å}\,\text{pix}^{-1}$ and a spectral resolution ($\sigma$) of $18.7\,\text{km}\,\text{s}^{-1}$. The wavelength range covered was $5110 - 5435\,\text{Å}$ which corresponded to the region around the magnesium triplet at the redshift of M60. The ability to collect integral field spectroscopy at such a high spectral resolution is currently unique to the INTEGRAL/WYFFOS configuration. Most integral field units are optimised to the velocity dispersion of a typical galaxy, so do not allow such a high dispersion.

### 4.1.3 The Observing Run

The weather conditions during the run were less than ideal. High winds resulted in the loss of some exposure time on the first night and the seeing was poor throughout the run ($\sim 3$ arcsec).

The beginning and end of the nights were used to obtain spectra of template stars, as well as a range of calibration frames. The majority of the rest of the

nights were spent exposing on the galaxy, with occasional sky and calibration frames. The extraordinary stability of the bench-mounted WYFFOS spectrograph, meant that very few arc calibration frames were required between exposures.

The galaxy frames were split into 30 minute exposures in order to minimise the number of cosmic ray hits on each individual integration. Between galaxy exposures the telescope was moved by a fraction of a fibre diameter. This dithering was required to provide complete coverage across the field of view (since the filling factor of the fibre bundle was only 0.61) and to protect against systematic errors that vary as a function of fibre number. The same dithering was used for the template stars so that possible changes to the line profile across different fibres could be investigated.

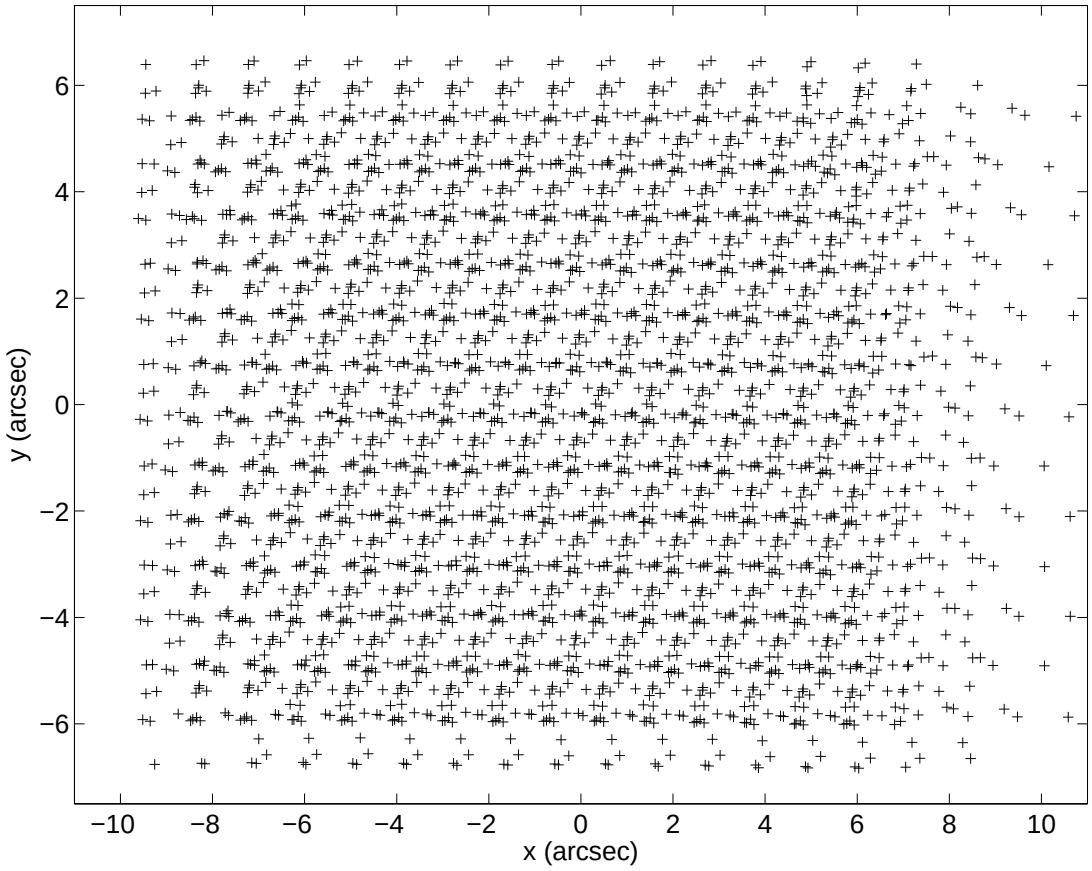


Figure 4.2: Dithering of the fibre bundle on the plane of the sky. Each cross shows the location of a fibre centre during an individual 30 minute exposure. North is up and East is to the left.

A total of 17 usable half-hour exposures were eventually recorded. Figure 4.2

shows a schematic representation of the fields observed during the run. A further six frames were also observed but were not used due to problems including the loss of the guide star due to cloud cover, telescope rotator limit being reached during the exposure and very low altitude above the horizon.

## 4.2 Data Reduction

The data were reduced using NOAO's `IRAF` image reduction and analysis facility. The frames were trimmed to remove the overscan region of the CCD. The bias level was found to be approximately constant across the whole field, so the mean number of bias counts was subtracted from the rest of the observed frames.

### 4.2.1 Aperture Definition and Extraction

The optical design of the `WYFFOS` spectrograph results in the light from each fibre being projected onto the CCD along a narrow, slightly curved path (see Figure 4.3 for an example CCD frame). In order to complete the rest of the data reduction, the spectra from the individual fibres must be extracted and placed into a so-called multispectral format in which each row of the image corresponds to an individual fibre, with the spectral information running in the perpendicular direction. Comparison of the tungsten flat-field frames indicated that the positions of the fibres on the CCD were constant over the course of a night, but varied slightly between the two nights. Flat frames were used to illuminate the fibre apertures on the CCD, which were then fitted with a low-order polynomial and extracted. Because of the inherent stability of the instrument, the same fibre apertures could then be used to extract the galaxy spectra.

### 4.2.2 The Scattered Light Problem

`WYFFOS`, like many spectrographs, suffers from stray light hitting the CCD due to internal reflection and other optical defects. Often this light can be strongly localised and have significant structure and may include sharp edges that can prove difficult to completely remove. Figure 4.3 shows a template star frame, where the structure of the scattered light is clearly visible (see regions (d), (e) and (f)). The standard method of removing scattered light is performed after the

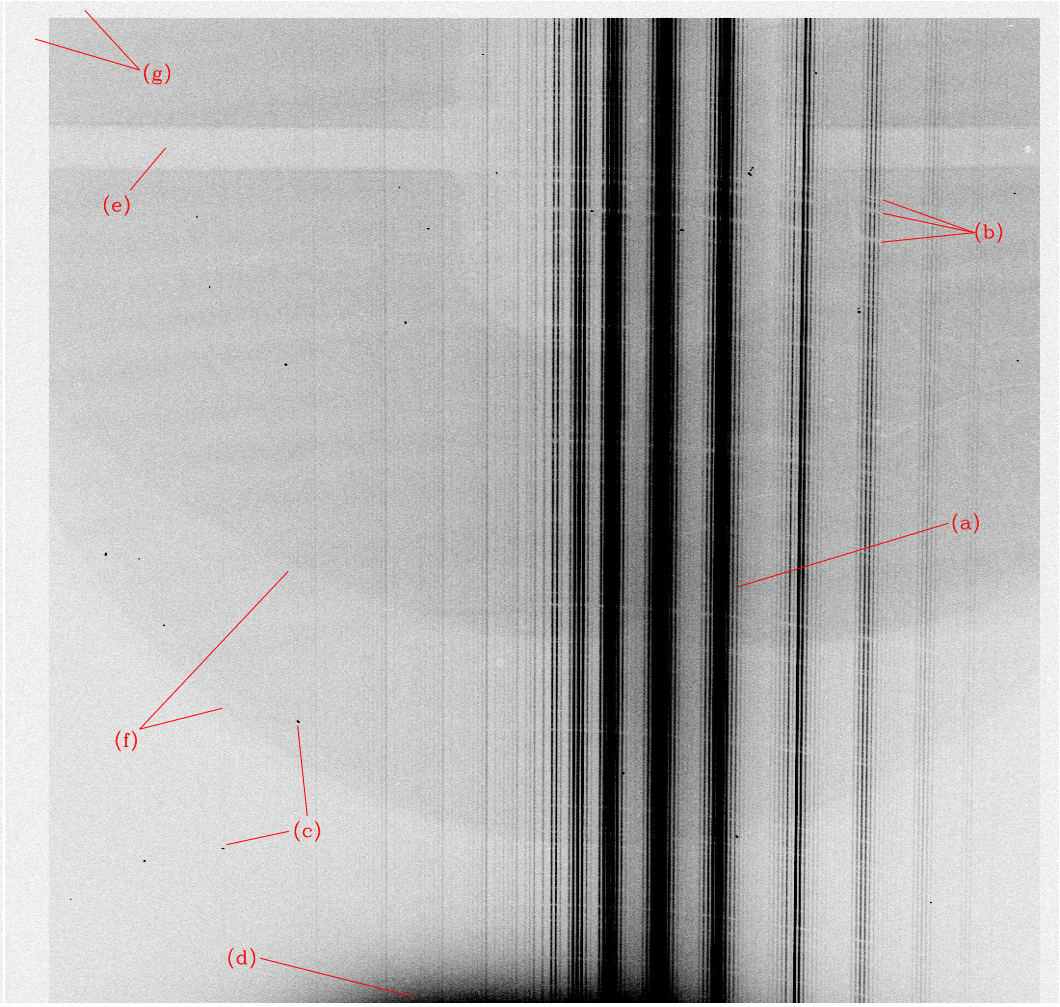


Figure 4.3: A raw CCD frame of a template star showing several common features: (a) Spectra from individual fibres, running vertically down the image. (b) curved absorption features appearing within the fibres. (c) cosmic ray hits. (d) a strong, smooth scattered light feature. (e) a sharp, trench-like scattered light feature. (f) other sharp-edged, large-scale scattered light features. (g) the overscan region.

fibre apertures have been defined but before the spectra are extracted. Narrow apertures are defined and a 2D surface is fitted to the regions of the CCD between the fibres, which are free from fibre light but still contain the scattered light features. This scattered light 'surface' is then subtracted and the extraction is performed as normal.

Unfortunately, the focus of the fibres in `WYFFOS` varies over the surface of the

CCD. In the corners of the frames where the focus was worst, the fibres blended together, leaving no region to use to calculate the scattered light profile. This was compounded by the fact that the scattered light profile varied over the course of the run, depending on the intensity and direction of the light source. This made it impossible to determine a single universal scattered light profile which could be subtracted from the remaining images.

Fortunately the amount of scattered light is dependent on the quantity of light received through the fibres. In the case of the target galaxy frames, the number of counts is sufficiently low that the scattered light can be ignored. Except for the strong feature at the bottom of the frame, which was excluded from the analysis, the scattered light contributed so little to the galaxy images that it could not be distinguished from the noise. However, this is not true in the case of the tungsten flat-field frames, which are required in order to remove the pixel-to-pixel variations due to the response of the CCD, so a separate procedure was developed to process these images.

### 4.2.3 Flat Fielding and Throughput Correction

Figure 4.4 shows some examples of features found on a flat field frame after it has been extracted into multi-spectral format. Some of the features are caused by the response of the CCD, while others are a result of scattered light. The aim was to fit a low-order surface to the tungsten continuum and large-scale scattered light features, then remove the remaining scattered light features while preserving as many of the pixel-to-pixel variations as possible. Since the profile of the scattered light varied between frames, it was possible to determine which features were introduced by the scattered light and which were intrinsic to the CCD.

In order to calculate the pixel-to-pixel response of the CCD, the following steps were taken:

1. The 'trench' was removed by averaging the extracted frame in the fibre direction, fitting to the sides and scaling the 'trench' region to the level of the surrounding data.

2. The sharp edges of the scattered light arcs tended to result in oscillations

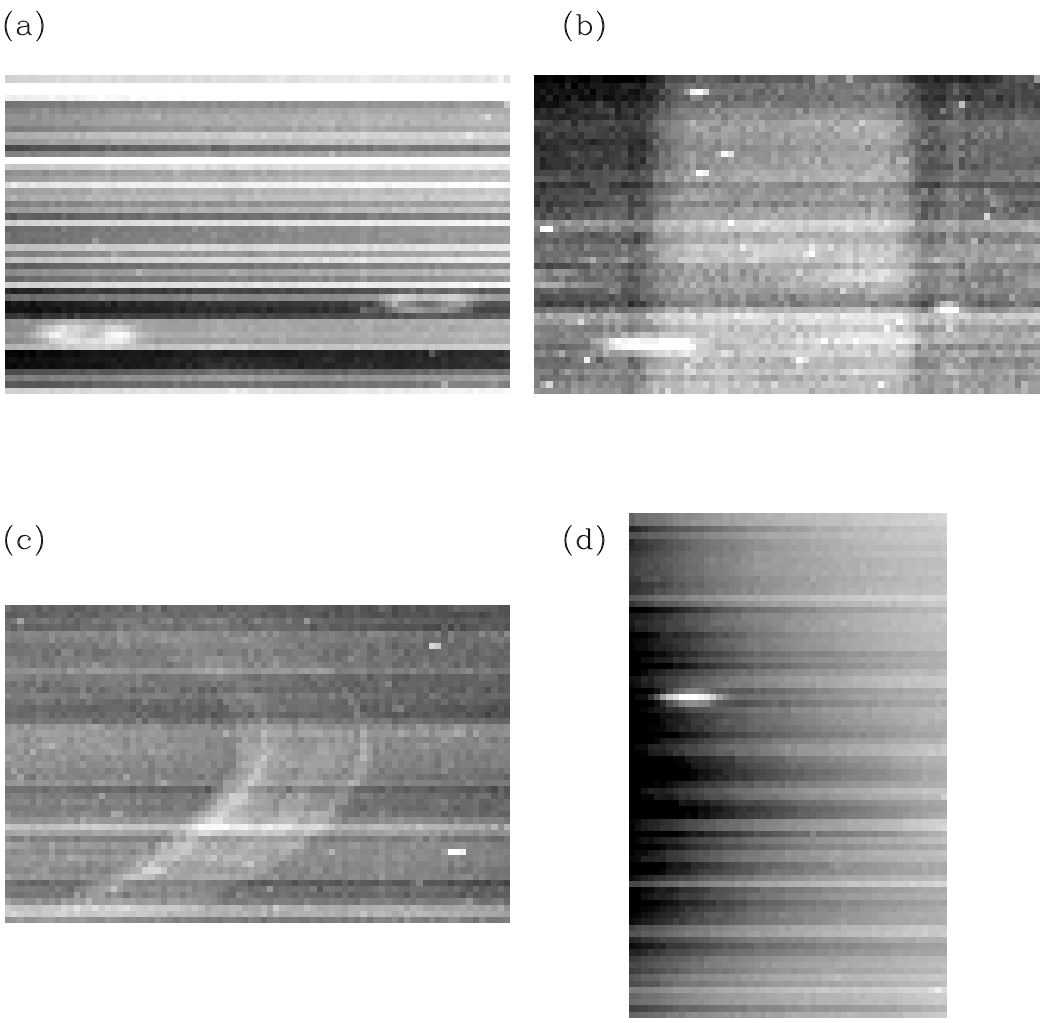


Figure 4.4: Close-ups of features found on an extracted tungsten lamp exposure. (a) Various pixel sensitivity features: Fibre-to-fibre variations, pixel-to-pixel variations and 'bad' sections of the CCD. (b) A 'trench' in the scattered light runs across the length of the CCD. (c) Sharp-edged 'arcs' of scattered light. (d) A strong smooth feature near the edge of the CCD. Note: The fibre-to-fibre variations have been removed from the images (b), (c) and (d) above in order to make the features more visible.

when attempting to fit the surface of the light distribution. They were therefore interpolated over using `imedit` before the surface fit was performed.

3. The 'bad' CCD regions also needed to be interpolated over in order to obtain the fit, but were required for obtaining the final response. Therefore they

were removed separately from the scattered light, using the same technique.

4. A 1D fit was made to the individual rows to obtain the fit to the spectrum of each fibre.

5. The frame obtained during step 2 was divided by the fit to the spectral response in order to obtain the CCD response.

6. The regions containing scattered light were masked out of the CCD response by setting the counts to 1.0 using `imedit`.

The median of several twilight sky frames was used to determine the variation in the throughput of the fibres. The final flat-field frames for the two nights were then determined separately, by combining scaled versions of the pixel-to-pixel flat field with the throughput correction. The CCD response and fibre throughput variations were then removed from the rest of the data frames by dividing the images by the flat-field.

### 4.2.4 Cosmic Ray Removal and Wavelength Calibration

Since the target frames were dithered around the field of view during observations, cosmic rays could not be removed by stacking sets of frames to form a single cosmic ray subtracted frame. Instead the `LACOS` task (van Dokkum 2001) was used to remove the majority of cosmic rays from individual frames. The algorithm identifies and removes cosmic rays of arbitrary shapes and sizes by the sharpness of their edges, using a Laplacian edge detection technique. A small number of remaining cosmic rays were removed by hand using the `imedit` task.

Examination of the calibration frames indicated that the wavelength solution was extremely stable over the course of the run, but did vary slightly between the two nights. An arc lamp frame from the middle of each night was used to perform the wavelength calibration. The positions of arclines were determined using the `identify` and `reidentify` tasks. The observations were then wavelength calibrated using `dispcor` and simultaneously binned in logarithmic units in the spectral direction. Six arclines from CuAr + CuNe lamps were used in the calibration, giving mean RMS residuals of 0.0042 Å, which translates to a velocity error of $0.24\,\mathrm{km\,s^{-1}}$. Although care was taken to minimise errors in the

wavelength solution, in practice small systematic errors should not affect the redshift determination (since gravitational redshift is a differential measurement). Systematic effects that vary as a function of fibre number would be more serious, but the effect of these was reduced by dithering the field of view across the galaxy.

The `rvcorrect` task was then used to shift the spectra to account for the heliocentric motion of the Earth around the Sun. The multispectral images of the stellar template stars were averaged into one-dimensional spectra and then velocity shifted to remove Doppler shifts due to peculiar motion using the `specshift` task.

### 4.2.5 Sky Subtraction

Because of the large angular size of the observed galaxy, the ring of sky fibres could not be used to perform the sky subtraction, since the contamination by galaxy light would be too great: at the radius of the ring the galaxy was still a factor of four brighter than the sky. Instead individual sky exposures were taken at various stages of the observing run. In practice, sky contamination was minimal, due to the high surface brightness of the centre of `M60`, the small number of strong sky lines in the observed region of the spectrum and the instrument's high spectral resolution.

From a single sky spectrum obtained by combining all available sky images and fibres it was clear that there were two strong features, a group of 3 lines at 5198 Å, 5200 Å and 5203 Å and a pair of almost unresolved lines at 5330 Å and 5331 Å. Since the individual lines could be so well resolved, it was decided to simply interpolate over the sky line regions of the spectrum and mask out the regions during the analysis.

### 4.2.6 Spatial Binning

In order to obtain reliable stellar kinematics free from systematic effects, the stellar spectra must have a reasonably high, uniform signal-to-noise ratio (e.g. van der Marel & Franx 1993). In the case of longslit data, this is achieved by averaging adjacent CCD rows until the desired S/N ratio is reached. An equivalent 2D binning method is more complex, since the shape of each individual bin must be considered.

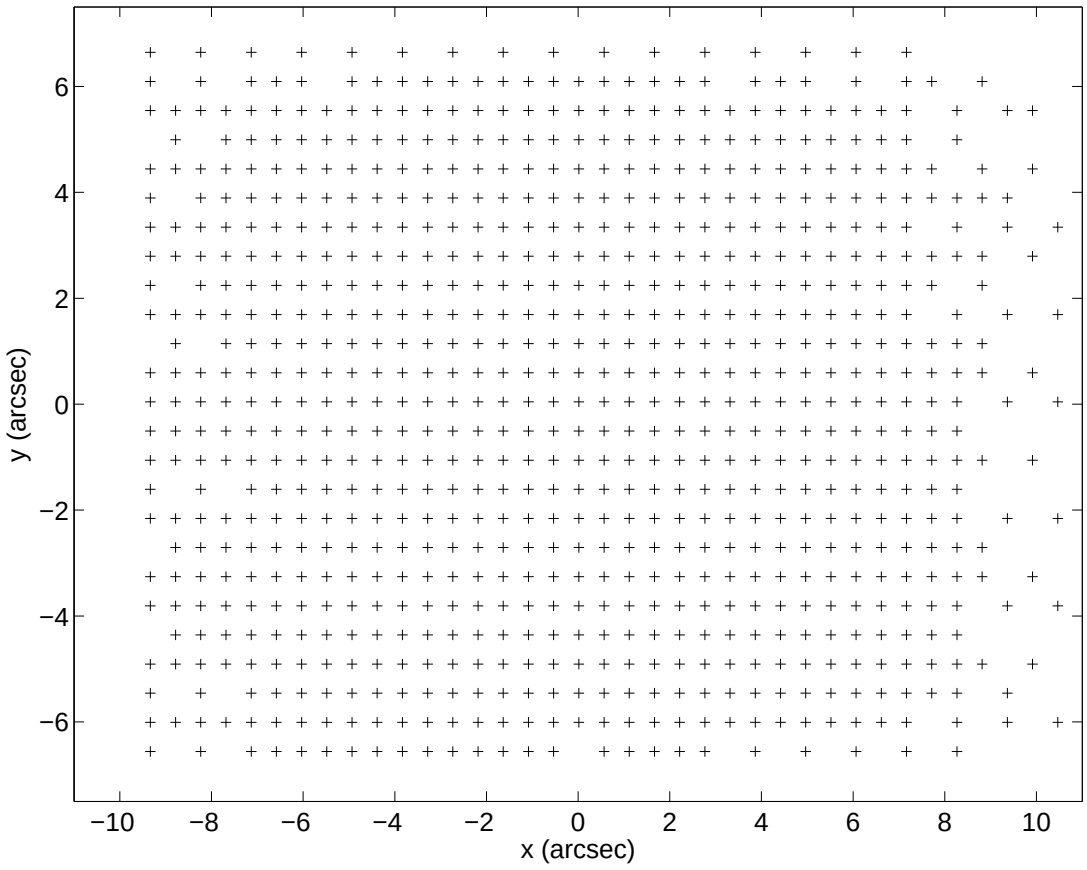


Figure 4.5: Locations of bins on the plane of the sky after the original exposures (Figure 4.2) were rebinned onto a regular grid with 0.55 arcsec pixels. North is up, East is to the left.

A two stage process was used to bin the data to a signal-to-noise ratio of $\sim 40$ per pixel. First the data were resampled on to a regular grid (see Figure 4.5). This was necessary since the second step described below required regularly spaced input. A pixel size of 0.55 arcsec was selected such that each pixel was as small as possible, but large enough to avoid producing gaps near the centre of the grid. Then an adaptive 2D binning technique based on Voronoi Tessellations (Cappellari & Copin 2003) was used to obtain the desired S/N ratio across the whole field of view. This method is advantageous as it naturally satisfies three important requirements:

1. The bins should join correctly at their boundaries, without overlapping or holes.

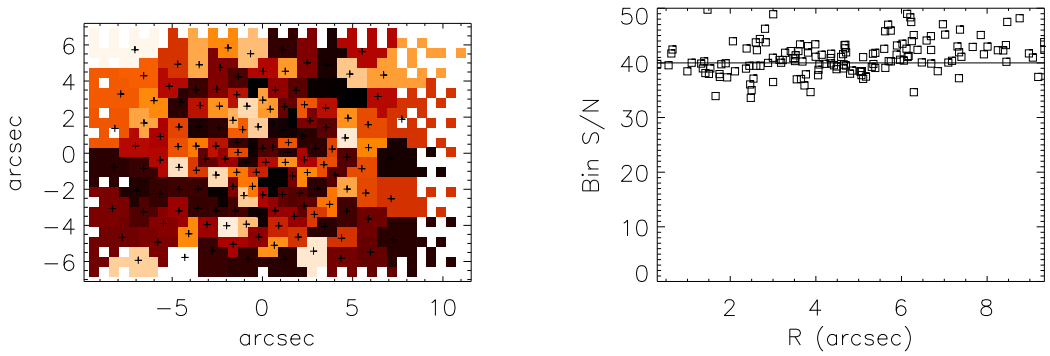


Figure 4.6: The coloured regions in the left panel show the individual bins as selected by the Voronoi binning routine. The black crosses show the flux-weighted centroids of the bins. The right panel indicates the scatter in S/N ratio around the desired value of 40, as a function of radius from the centre.

2. The bins should be as round as possible, so that each bin can be associated with a well defined spatial position.

3. The scatter of the signal-to-noise ratio around the desired value should be minimised as much as possible.

All spectra associated with an individual bin were summed to produce a single spectrum for that bin. Figure 4.6 shows the location of the bins and signal-to-noise ratio obtained by the routine.

Figure 4.7 shows a typical continuum subtracted spectrum from one of the Voronoi bins.

## 4.3 Data Analysis

### 4.3.1 Stellar Kinematics

The data were analysed using van der Marel's Gauss-Hermite Fourier fitting software (van der Marel & Franx 1993) in a similar way to the longslit data in Chapter 2. The continuum was subtracted by fitting a polynomial, then each spectrum was analysed using a K0 type star as the template. The magnesium triplet was found to be broadened to form a single feature which made it extremely difficult to determine the continuum level. Since it was also partially

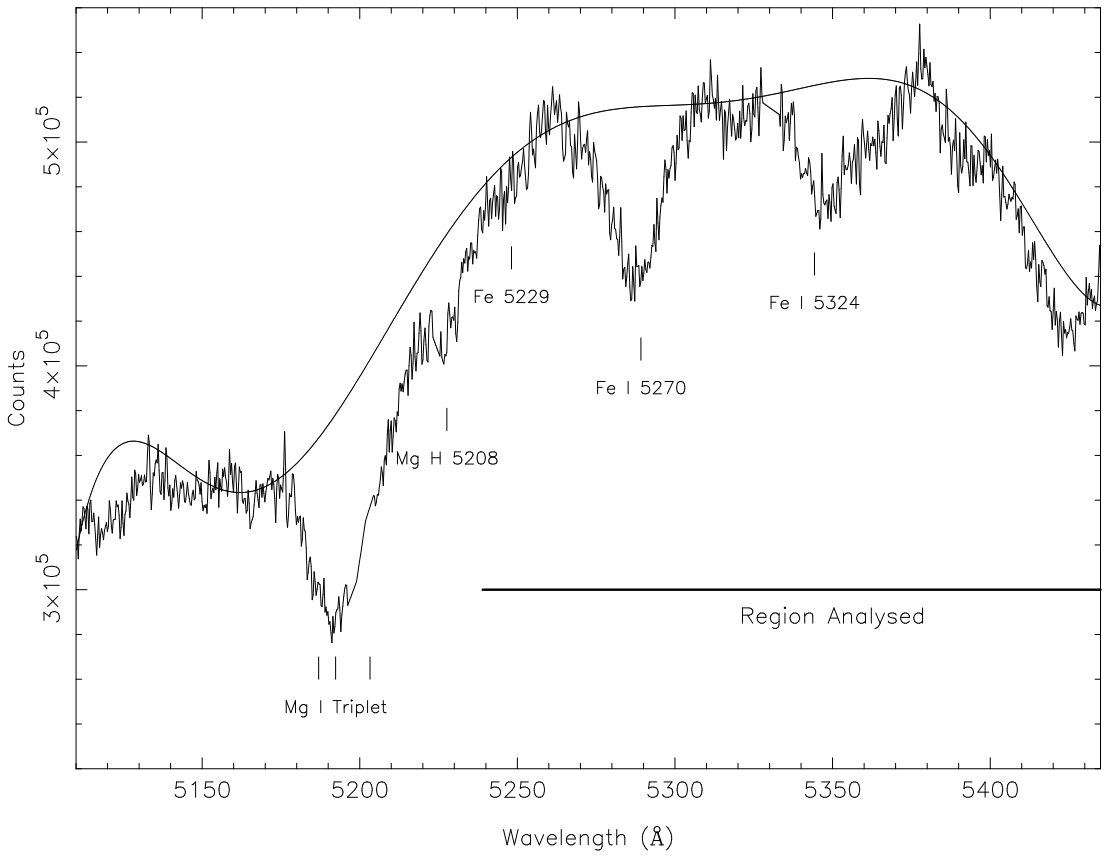


Figure 4.7: An example binned spectrum from near the centre of the galaxy. The continuum fit is indicated by the thin solid line. Strong absorption features are labelled. The bold horizontal line indicates the region used in the subsequent analysis.

obscured by a sky line it was excluded from the analysis. Without this feature, the analysis depended on two strong, isolated iron lines (see Figure 4.7).

Figure 4.8 shows the mean velocity, velocity dispersion and reconstructed surface intensity, for the galaxy. The field has been rotated such that the major axis lies along the x direction and minor axis along the y direction. The intensity map appears to show a slight misalignment between the position angle of the isophotes in the inner region and the major axis of 105°. This twisting of the central isophotes is consistent with the results of Peletier et al. (1990), who found that the position angle changed from 95° in the centre to 105° at 80 arcsec.

Figure 4.9 compares the integral field results with major axis longslit kinematics

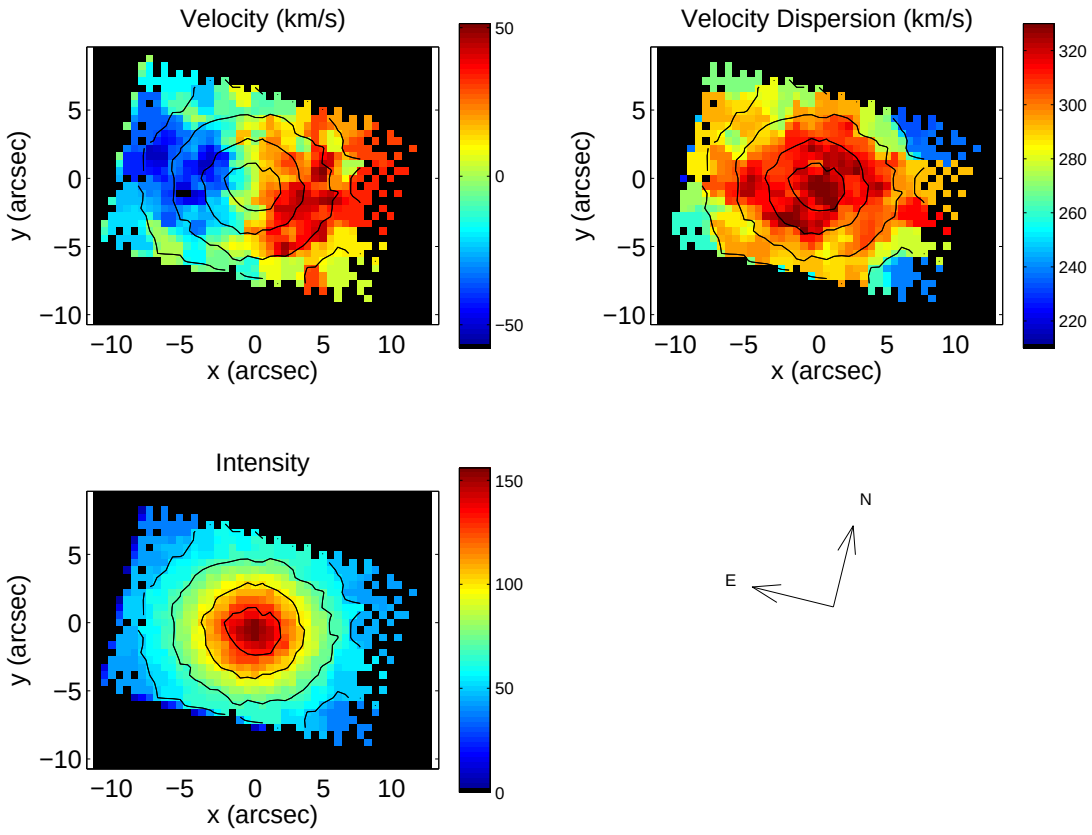


Figure 4.8: Mean velocity, velocity dispersion and intensity maps for M60. Maps have been rotated such that the major axis lies along the x direction. Black lines indicate reconstructed intensity contours.

observed by Fisher, Illingworth & Franx (1995). While the mean velocities show a good agreement, the velocity dispersion shows a significant discrepancy which is roughly consistent with a systematic offset of $\sim 40\,\mathrm{km\,s^{-1}}$ between the two datasets. Although the poor seeing during the observing run would reduce the magnitude of a sharp central peak, the seeing alone is not sufficient to explain the observed discrepancy. One common reason for systematically low velocity dispersion measurements is over-subtraction of the continuum, although in this case the continuum appeared well defined between the absorption features used. The discrepancy in the velocity dispersion should not affect the determination of the gravitational redshift, since it is measured using the mean velocity profile, which is in good agreement with existing data.

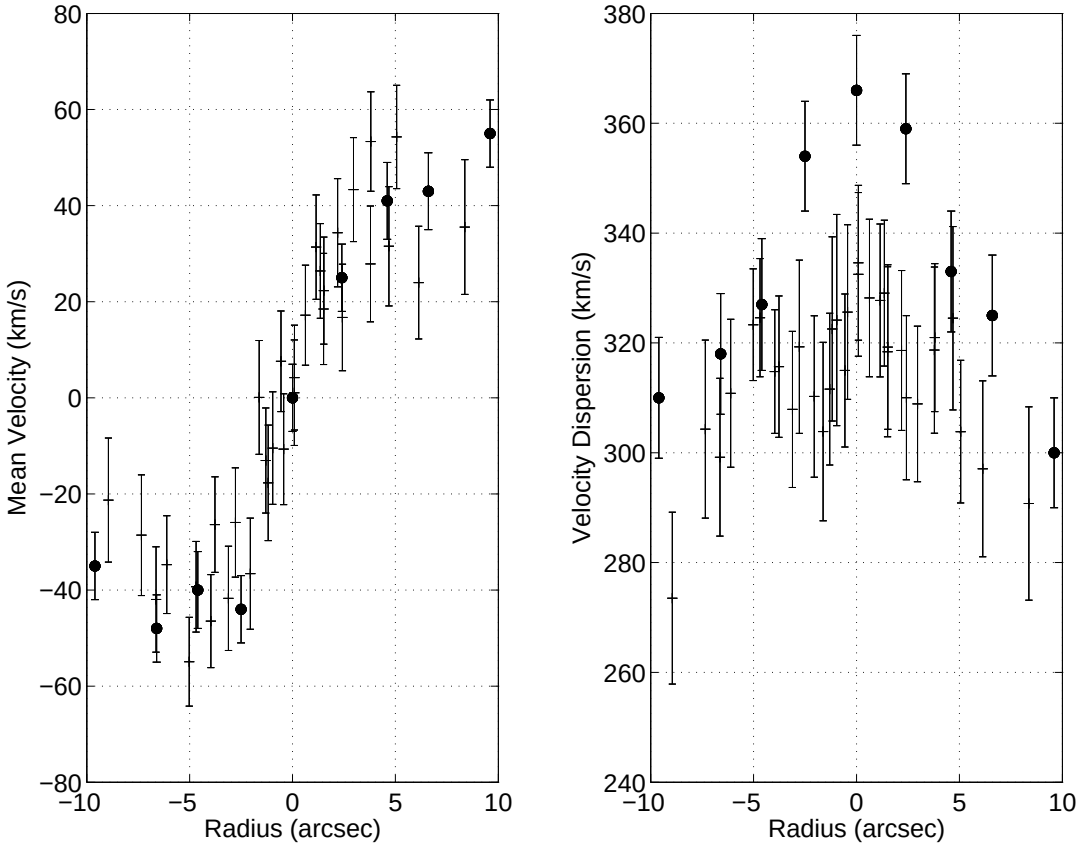


Figure 4.9: Comparison of major axis (PA = 105°) mean velocity (left panel) and velocity dispersion (right panel) measurements between integral field data (crosses) and longslit kinematics from Fisher, Illingworth & Franx (1995) (filled circles).

### 4.3.2 Determination of Atmospheric Seeing

The seeing during the observing run was determined by comparing the reconstructed light profile from the integral field data with $V$-band WFPC2 photometry from the HST archive (van Dokkum & Franx 1995). Since only a crude estimate was required, the data were used straight from the archive, without any cosmic ray removal or photometric calibration. The reconstructed light profile was rebinned onto a fine grid to match the 0.0455″ pixel scale of the HST planetary camera image. The HST data were then convolved with a range of Gaussians corresponding to different seeing conditions and compared to the reconstructed light profile. Vertical alignment was achieved by scaling the reconstructed intensity in such a way that the two profiles matched in the region which was

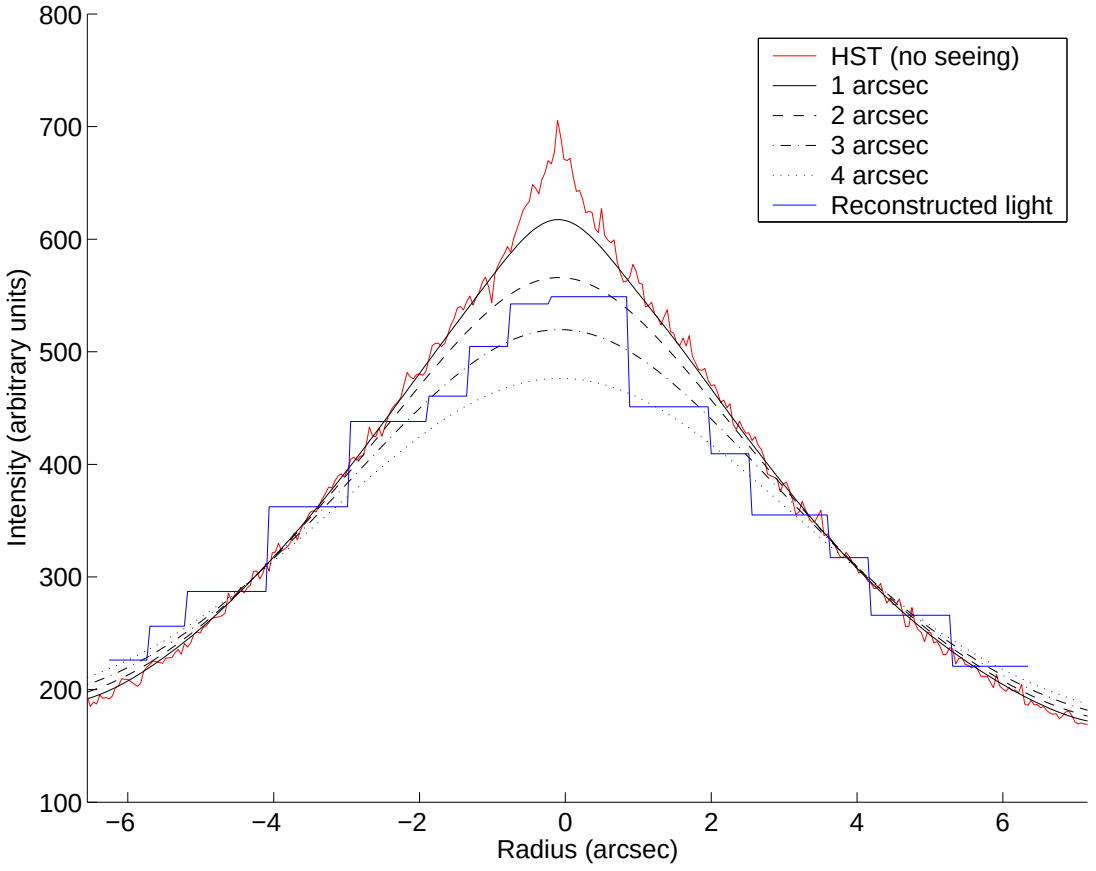


Figure 4.10: Comparison of the reconstructed light profile (blue line) to HST photometry (red line). The black lines show the HST photometry convolved with a range of seeing profiles. The solid, dashed, dot-dashed and dotted lines have widths of 1, 2, 3 and 4 arcsec FWHM respectively.

insensitive to changes in the seeing ($|R| \simeq 4$ arcsec).

The HST data were convolved with a range of Gaussians and the best-fit to the light profile was found. Figure 4.10 shows a cut through the centre of the galaxy comparing the integral field light profile with the HST profile in different seeing conditions. The best-fit seeing was found to be $\sim 3$ arcsec, although the exact value was sensitive to exactly how the two profiles were scaled in intensity. This figure is consistent with in situ measurements of stars, which implies that the reconstructed images have not been degraded by any of the analysis described above.

### 4.3.3 Searching for Stellar Streaming using Unsharp Masking

Before attempting to determine if a gravitational redshift signal could be found, the data were searched for evidence of coherent stellar streaming motions in the inner regions. Such non-equilibrium motions could conspire to create a signal similar to that of a gravitational redshift, but they are also interesting in their own right, as they could provide evidence of recent merger activity.

If such a coherent structure were located near the centre of M60, it might be expected to appear superimposed over the observed spectrum as a separate star-like spectrum, offset from the main galaxy spectrum, with its own (presumably smaller) velocity dispersion. Given the high spectral resolution of the INTEGRAL spectrograph, it might be possible to locate such motions across the plane of the sky. Indeed, locating a stream which occurs with a similar velocity over a range of fibres would add weight to the claim of a detection.

To search for such features, the spectrum of the galaxy was first removed by unsharp masking the data, which involves subtracting a smoothed version of each spectrum from itself. This removes the underlying broad absorption features but leaves small scale features within the residuals. This residual spectrum was then cross correlated with a template star to look for any remaining features, limiting the allowed velocity range to $\pm 500\,\mathrm{km\,s^{-1}}$ around the galaxy's mean redshift.

The height of the cross correlation peak above the noise should provide information about the relative luminosity of any material relative to the galaxy. It also gives the significance of the features in the cross correlation velocity map - if a coherent structure occurs which also results in large peak heights in that region, it is more likely to be a real structure.

Figure 4.11 shows the results of the above procedure. There is no obvious structure in the reconstructed images and the highest cross correlation peak heights are not significantly above the noise level. This is not entirely surprising, given that the galaxy was selected on the basis of its smooth kinematics, photometric appearance and the lack of nuclear activity. The result suggests there are no bright streams that would strongly affect the gravitational redshift measurements.

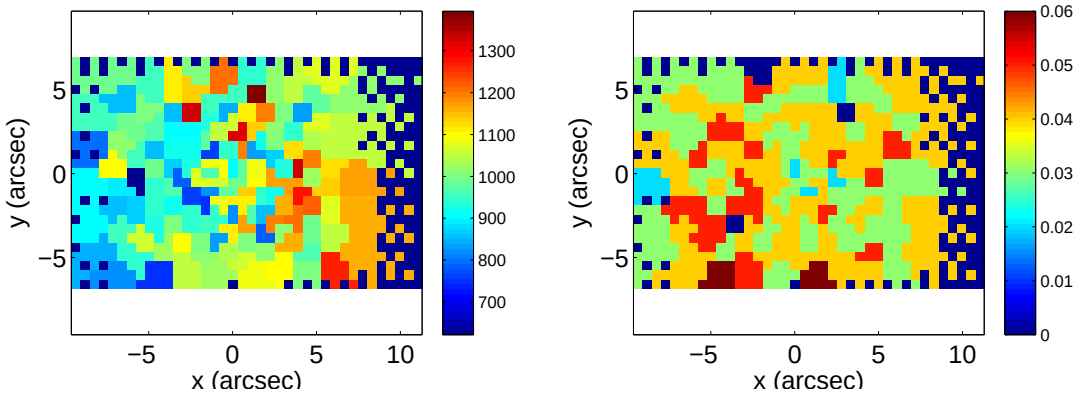


Figure 4.11: Left panel: Velocity of highest cross correlation peak. Right panel: Height of cross correlation peak. North is up and East is to the left.

### 4.3.4 Analysis of the Velocity Field for Gravitational Redshift

In Chapter 3 a method for determining gravitational redshift was introduced. For longslit data, the even component of the velocity must be extracted in order to remove the effect of rotation from the velocity profile. In the case of 2D data, the analogous approach is to average the velocity in bins that trace the galaxy's isophotes.

Radial bins were defined using the Nuker law fit of Lauer et al. (1995). Each Voronoi bin was assigned to a radial bin based on the location of its flux-weighted centroid. The velocity of each annular bin was found by taking the mean of the velocities of all Voronoi bins assigned to that annulus.

The error on each radial velocity was determined from the scatter of individual values according to

$$\Delta v = \frac{\sigma}{\sqrt{N}}, \tag{4.1}$$

where $\sigma$ is the standard deviation of a bin's velocities and $N$ is the number of velocities in that annulus. Figure 4.12 compares the shift found to the gravitational redshift model for this galaxy. The data points suggest a central rise in the mean velocity, although the error bars are too large to give a statistically significant result. The intrinsic scatter of the data points suggests that the error bars have been somewhat overestimated. Unfortunately the gravitational redshift given by

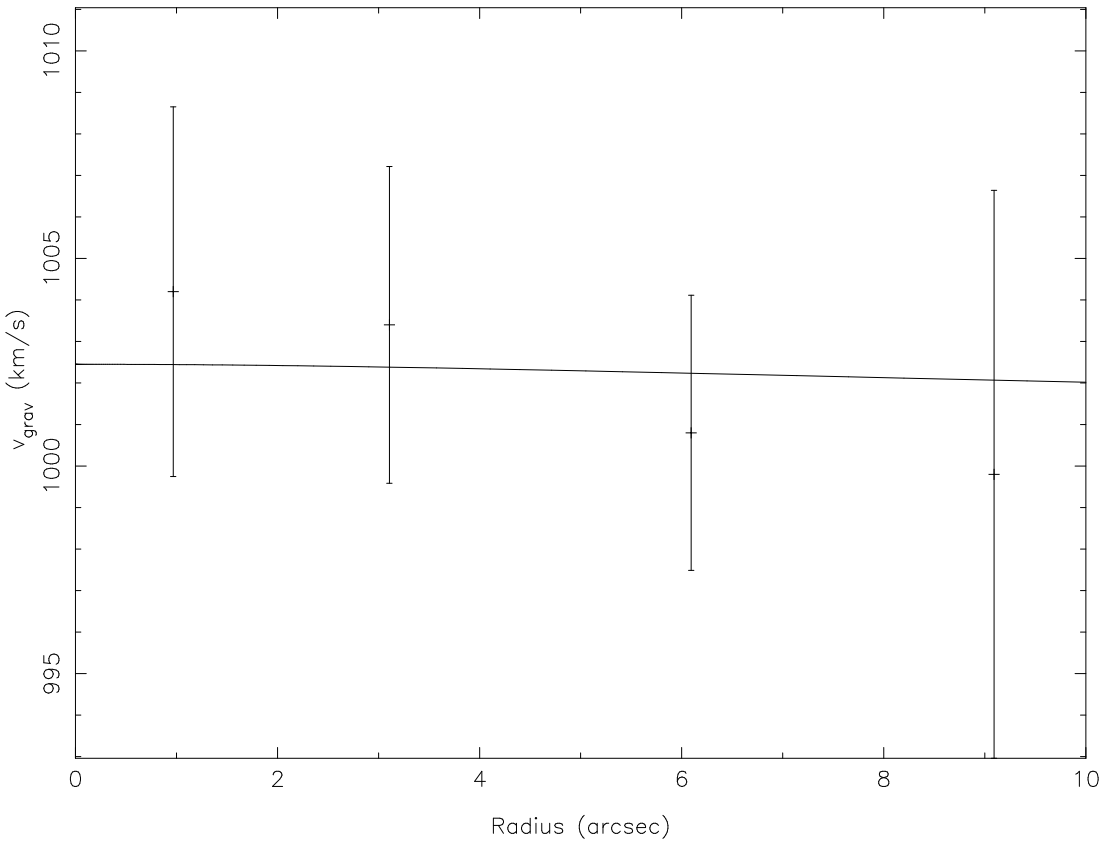


Figure 4.12: Velocity shift in the centre of M60. The solid line indicates the predicted gravitational redshift, including projection onto the plane of the sky and the effect of $3''$ seeing.

the model (solid line) turned out to be extremely small in this case ($\sim 0.5\,\mathrm{km\,s^{-1}}$). The reason for such a small shift is discussed in detail below.

## 4.4 Conclusions

Existing work by Stiavelli & Setti (1993) on detecting gravitational redshift predicted a signal of order $10-20\,\mathrm{km\,s^{-1}}$ in a typical elliptical galaxy. An isothermal density profile used to plan the observations also indicated shifts of $\sim 10\,\mathrm{km\,s^{-1}}$ should be expected. Why then should a massive elliptical galaxy such as M60 contain such an insignificant shift when using the model described in Chapter 3? The magnitude of the signal was slightly reduced by the poor atmospheric seeing, but this alone could not account for the difference.

Experimentation with a range of profiles revealed that the expected signal is strongly dependent on the degree of central concentration. For constant mass-to-light ratio models, the central density profile is defined by the light profile. In the case of M60, despite its unusually large central velocity dispersion, the central gradient is comparatively shallow, with an inner slope of $I(R) \propto R^{-0.153}$. In comparison, an isothermal profile has an $I(R) \propto R^{-2}$ dependence, while the model used by Stiavelli & Setti also gave a steep inner gradient ($I(R) \propto R^{-1.9}$). Both of these models will therefore overestimate the magnitude of the redshift expected in M60.

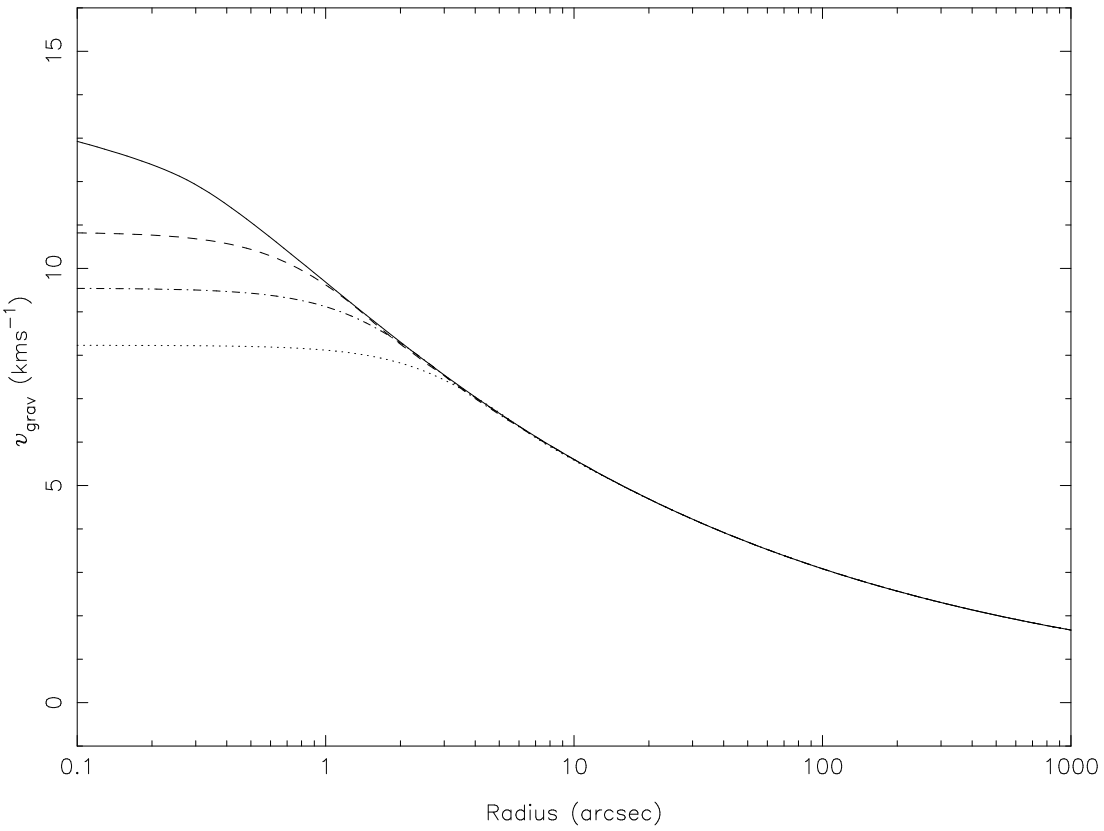


Figure 4.13: Predicted gravitational redshift for the compact elliptical galaxy M32. The solid line shows the projected gravitational redshift in the absence of seeing. The dashed, dot-dashed and dotted lines show how the signal is altered in the presence of 0.5, 1 and 2 arcsec seeing.

As well as increasing the intrinsic redshift signal, a cuspy light profile offers an additional benefit – less signal is lost during the deprojection since the central regions contribute more to the flux-weighted determination of the redshift. Since

the inner light profile is so important, it is logical to consider observing targets which are more centrally concentrated than a typical galaxy. Figure 4.13 shows the predicted gravitational redshift for the compact elliptical galaxy M32, given a constant $H$-band mass-to-light ratio of $2.0\,M_{\odot}/L_{\odot}$. M32 is a compact, nearby E3 galaxy with a central velocity dispersion of only $\sim 130\,\mathrm{km\,s^{-1}}$ (Joseph et al. 2001). This suggests that the central concentration is at least as important as the mass in producing a detectable signal, if not more so. Some of the difficulties in measuring the mean velocity were due to the width of the absorption features, which was caused by the unusually high velocity dispersion of M60. The target was selected precisely *because* it had a large velocity dispersion, implying a large mass. If a large mass is not a required to obtain a signal, galaxies with lower velocity dispersion can be chosen, resulting in less line blending and further improving the chance of a detection.

M32 is a high surface brightness companion of the nearby Andromeda galaxy and hence has been observed many times in the past. This includes integral field spectroscopy using the SAURON integral field spectrograph (Verolme et al. 2002) and high spatial resolution longslit spectroscopy using STIS on the HST (Joseph et al. 2001). Their work was examined for an indication of a central even component, but the size of the error bars were too large to determine the even component to the accuracy required. Using the higher spectral resolution and increased stability of INTEGRAL/WYFFOS, it should be possible to reduce the errors sufficiently to make a positive detection.

# Chapter 5

# Gravitational Redshift in the 2dF Groups Catalogue

It was shown in the previous chapter that the gravitational redshift expected in the cores of elliptical galaxies is non-zero, but at a level that is difficult to clearly detect using current technology. Stiavelli & Setti (1993) suggested that it may also be possible to observe the effect in clusters of galaxies. Clusters can contain hundreds of individual galaxies as well as large masses of hot X-ray gas and dark matter, providing deep potential wells that will result in a larger gravitational redshift signal. Simple dynamical arguments suggest that the expected gravitational redshift should scale roughly as $v_{\rm grav} \propto \sigma^2/c$. Since a typical elliptical galaxy has a velocity dispersion of order $\sigma \sim 300\,{\rm km\,s^{-1}}$, in comparison to $\sigma \sim 1000\,{\rm km\,s^{-1}}$ for a cluster, one should naively expect a factor of ten increase in the gravitational redshift (of the order $50 - 100\,{\rm km\,s^{-1}}$).

Cappi (1995) investigated the gravitational redshift in clusters by comparing the velocity of a sample of central cD galaxies to the mean velocity of the parent cluster and found 5 out of 6 clusters gave central redshifts. He developed a model for predicting the expected signal by assuming a de Vaucouleurs density profile and concluded that the gravitational redshift in clusters could exceed $100\,{\rm km\,s^{-1}}$ in rich clusters. Broadhurst & Scannapieco (2000) suggested a method of detecting gravitational redshift using X-ray gas spectroscopy. They also considered a similar sample of massive clusters with central cD galaxies and obtained a mean central redshift of $v_{\rm grav} = 260 \pm 58\,{\rm km\,s^{-1}}$.

Not all clusters contain a central cD galaxy which can be used to determine the central redshift. The following alternative method was developed which could be

used to obtain a central redshift for any cluster, given the locations and redshifts of a number of its members:

- The cluster is divided into two groups. Individual galaxies are assigned to a group based on their projected distance from the centre of the cluster. Galaxies within a cut off radius $R_{\rm cut}$ are assigned to the inner group. The remaining galaxies form the outer group. The details of how the cut off radius is selected are discussed later in this chapter.
- The median velocity of each of the samples is found. The median is preferred over the mean since it provides a more robust estimate of the centre of the distribution.
- The gravitational redshift of the cluster $v_{\rm grav}$ is obtained by taking the difference between the inner and outer median velocities. If the core region is redshifted compared to the rest of the cluster this should result in a positive value for $v_{\rm grav}$.

## 5.1 Feasibility Studies

Despite the increased magnitude of the expected signal, detecting gravitational redshift in clusters poses a different set of challenges to the approach used in the previous two chapters. Unlike elliptical galaxies, which are thought to be largely relaxed systems, clusters are unlikely to be in a state of dynamic equilibrium. The coherent motion of substructure within the cluster will contaminate the signal in the same way as non-equilibrium motions do in elliptical galaxies.

Secondly, velocity determinations in clusters take the form of discrete measurements of individual galaxies, rather than the mean velocity of a distribution of unresolved stars. Therefore the error on the determination of the mean velocity is dependent on the number of galaxy redshifts in the cluster.

In order to successfully measure the gravitational redshift, these sources of error must not outweigh the expected signal. Numerical simulations were developed to confirm that this was the case and to determine the sample size required for a positive detection.

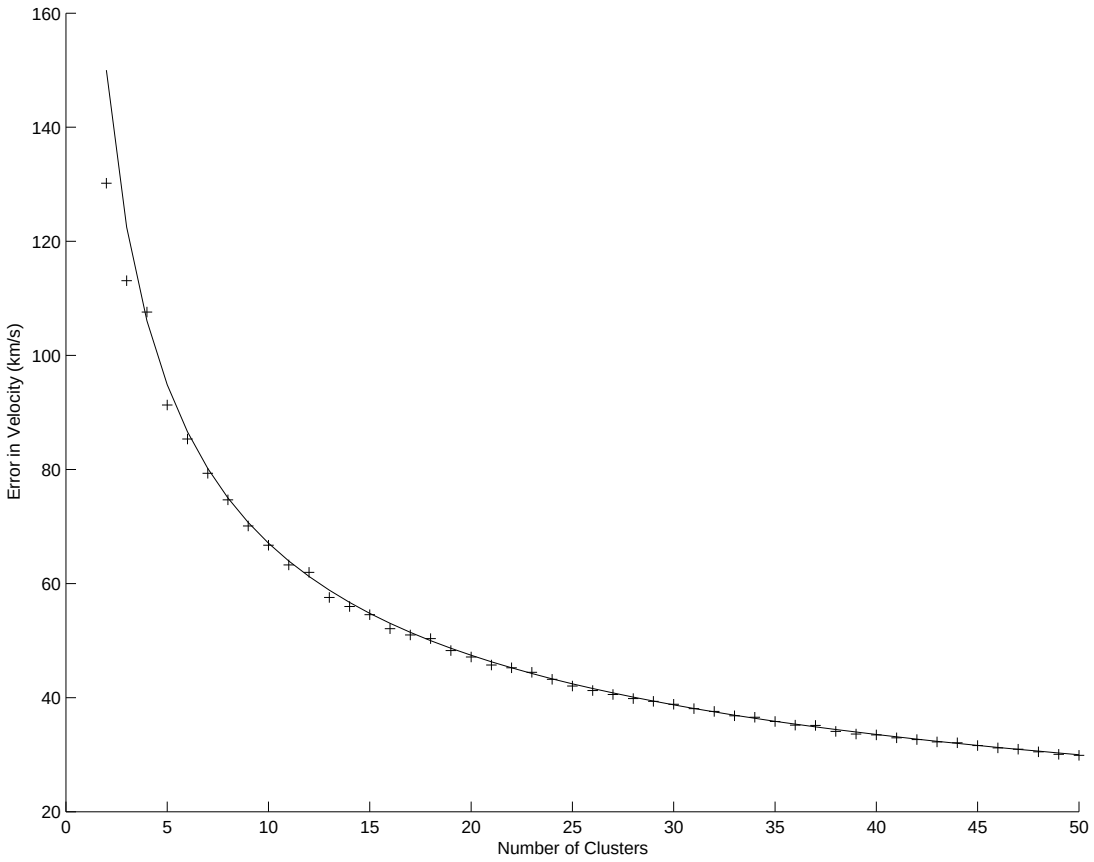


Figure 5.1: Monte Carlo simulations of the error on the mean velocity due to infall into the cluster. The points show the mean error obtained after 100 realisations for each cluster sample. The solid line shows the function described in Equation 5.1.

### 5.1.1 Scatter due to Infall along the Line of Sight

Although historically it was thought that galaxy clusters were relatively static systems, they are now known to have a significant amount of infall and substructure (e.g. Colberg et al. 1999; Hoekstra, Franx & Kuijken 2000). If infall happened to occur along the line of sight to the cluster, then it could result in a signal similar to a gravitational redshift or blueshift. Since the magnitude and sign of any spurious signal is dependent on the direction of infall relative to the line of sight (which is completely random), by averaging the signal over a number of clusters this effect will tend to zero, although it will result in a small increase in the intrinsic dispersion of velocities within the distribution.

In order to quantify the significance of this effect, a toy model was constructed and

simulations were run to determine the amount of scatter expected as a function of the number of clusters in the sample. In the model, galaxies were assumed to be falling towards the centre of the cluster from a single direction, which was at a random angle $\theta$ from the line of sight, where $0 \leq \theta \leq 180$ degrees.

The simulations showed that for an infall velocity $v_{\rm infall}$, the scatter expected in the mean velocity of the clusters is given by

$$\delta v_{\rm grav} = \frac{1}{\sqrt{2}} \frac{v_{\rm infall}}{\sqrt{N_c}}, \tag{5.1}$$

where $N_c$ is the number of clusters in the sample. So if an infall of $300\,{\rm km\,s^{-1}}$ is assumed then 18 such clusters viewed from random orientations would result in an error on the mean velocity shift of $50\,{\rm km\,s^{-1}}$ (see Figure 5.1).

This simple model relies on several assumptions. Firstly, the infall is assumed to occur from a single direction. This is unlikely to be the case, but represents the 'worst case' scenario: if infall occurs in a more homogeneous manner then it will tend to cancel out and the effect will be reduced. The more clumps of material that fall into a single cluster, the lower the scatter due to this effect.

The other assumption is the magnitude of the infall velocity $v_{\rm infall}$. This is a difficult quantity to estimate, hence the value used is somewhat arbitrary. From the conservation of energy, a particle falling from infinity to within 2 Mpc of a cluster of mass $10^{13}\,M_\odot$ would reach a speed of $\sim 200\,{\rm km\,s^{-1}}$. Another approach to this problem would be to calculate the mean velocity around clusters formed by numerical simulations. Since such simulations would not contain any gravitational redshift, deviations from zero would be solely due to infall. They would also be expected to better represent the true mass and frequency of infalling material than the simple model described above.

### 5.1.2 Scatter due to Cluster Velocity Dispersion

Since the galaxies have a random motion due to the velocity dispersion of the cluster, the accuracy of the median velocities for the inner and outer regions is limited by the number of discrete velocities in each sample.

For a Gaussian distribution of velocities of width $\sigma$, the error on the *mean* velocity is given by

$$\delta v = \frac{\sigma}{\sqrt{N}}, \tag{5.2}$$

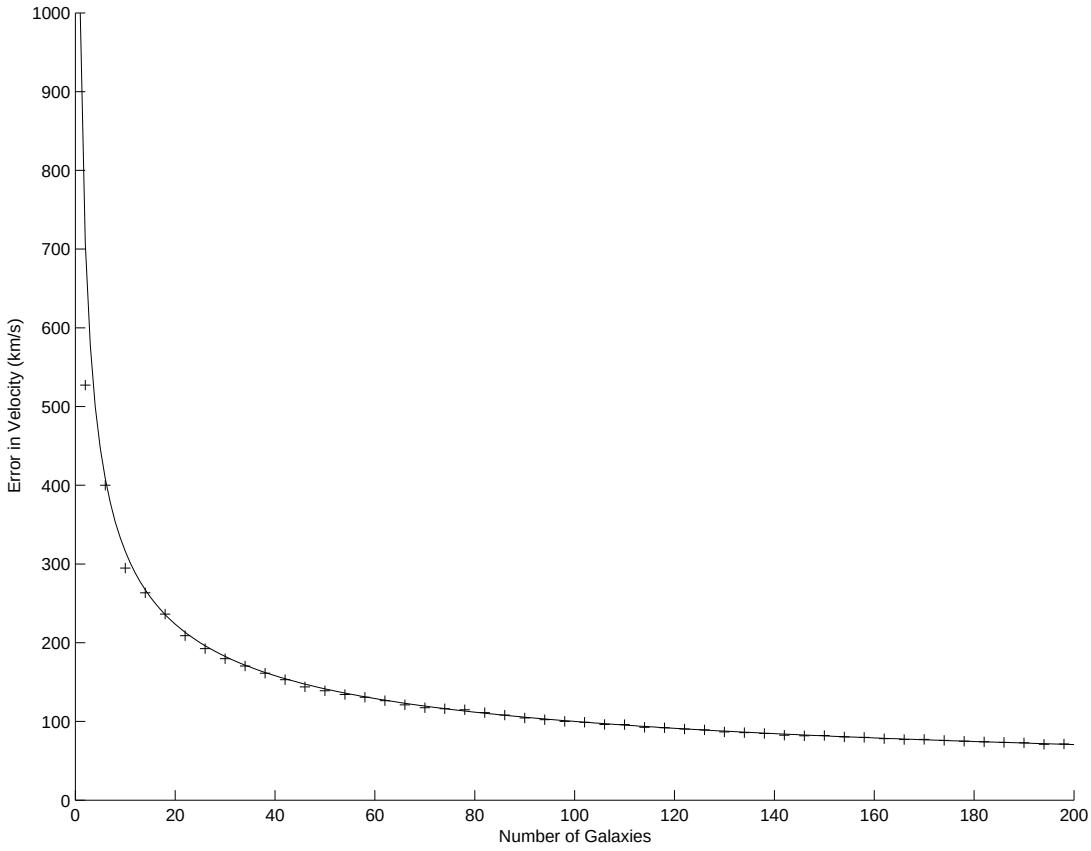


Figure 5.2: Monte Carlo simulations of the error on the mean velocity due to the intrinsic velocity dispersion of the cluster. The points show the mean error obtained after 100 realisations for each cluster sample. The solid line shows the function described in Equation 5.2.

where $N$ is the number of velocities in the sample. For this work it is assumed that the error on the median is given by the same formula. Since the intrinsic scatter of velocities within each group is determined by the velocity dispersion of the cluster, the above formula can be used to determine the errors on the median velocities.

Since the gravitational redshift is obtained from the difference between $v_{\rm inner}$ and $v_{\rm outer}$, the error on $v_{\rm grav}$ is given by the sum in quadrature of the errors on the inner and outer velocities

$$\delta v_{\rm grav} = \sqrt{\delta v_{\rm inner}^2 + \delta v_{\rm outer}^2}. \tag{5.3}$$

The smallest error on $v_{\rm grav}$ is obtained when $R_{\rm cut}$ is located such that both the

inner and outer samples contain $N$ galaxies and hence

$$\delta v_{\rm grav} = \sigma \sqrt{\frac{2}{N}} \tag{5.4}$$

This relationship was confirmed using Monte-Carlo simulations, which show that for a cluster with a velocity dispersion of $1000\,{\rm km\,s^{-1}}$ containing 200 galaxies, the redshift can be determined to an accuracy of $100\,{\rm km\,s^{-1}}$ (See Figure 5.2). Therefore if 100 such clusters were available, the velocity difference for the whole sample could be determined to $10\,{\rm km\,s^{-1}}$.

### 5.1.3 Projection Effects

The calculation of the velocity shift relies on the assumption that galaxies that lie a small projected distance from the centre of the cluster are intrinsically near to its core. In fact this is not always the case: galaxies in the outer regions may appear to be located near the projected centre, by chance alignments along the line of sight.

In order to account for this effect, it is necessary to determine the density distribution of the galaxies in the cluster. This can be done by smoothing a histogram of the number of galaxies as a function of radius from the centre. More detail of this method is given in Section 5.3.2. Simulations show that projection effects result in a slight dilution of the signal due to contamination by chance alignments along the line of sight, but only at the level of around 10%. The effect is small because clusters of galaxies are typically centrally concentrated systems.

## 5.2 Dataset

It is clear from the feasibility studies described above that it is advantageous to use a large sample, both in terms of the number of galaxies per cluster and the total number of clusters in the sample. It is also crucial to use a homogeneous sample in order to minimise the possibility of differences in the definition of a galaxy cluster.

The 2dF Percolation-Inferred Galaxy Group (2PIGG) catalogue (Eke et al. 2003, in preparation) was selected for use in this study, as it fulfills all the requirements described above. The survey contains 54,888 galaxies in 7,259 groups with 4 or

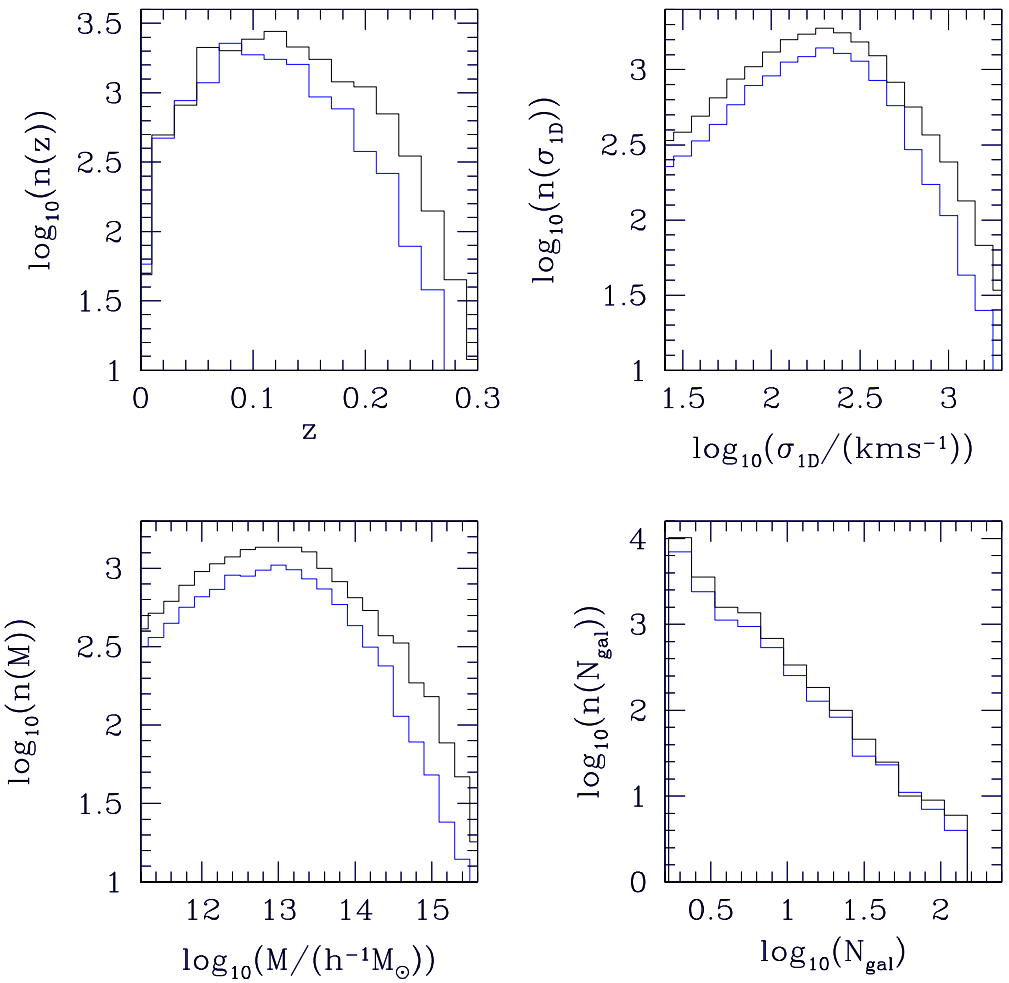


Figure 5.3: Properties of the 2dF groups catalogue for the northern (blue) and southern (black) 2dF samples. Histograms show the distribution of group redshifts, velocity dispersions, estimated masses and number of members.

more members and 23,183 galaxies in 1,217 groups with 10 or more members. Figure 5.3 shows the properties of the sample.

For a given cluster catalogue, it is necessary to select groups of galaxies from the sample which form gravitationally bound, physically significant units. The properties of these groups, such as their velocity dispersion and physical scale must then be determined. Identifying individual systems can be performed using a range of different methods (see e.g. Katgert et al. 1996; Zabludoff, Huchra & Geller 1990) and it can prove difficult to objectively select groups without relying on arbitrary assumptions.

The 2PIGG Catalogue uses a friends-of-friends percolation algorithm to identify cluster members (Eke et al. 2003, in preparation). This method forms groups of galaxies by associating galaxies to their nearest neighbours in three dimensional space. The most important factor in ensuring that physically significant groups are homogeneously selected across the whole sample is the 'linking length'. This is the maximum distance allowed between two galaxies before they are no longer considered to be part of the same group.

The analysis is complicated by the fact that completeness of the survey is not uniform as a function of redshift – faint galaxies that would be found in a nearby group are below the magnitude limit of the survey at greater distances. To account for this, the linking length must be chosen in such a way that the groups are selected in an unbiased fashion (i.e. the boundary of a particular group should occur at the same distance, independent of its redshift). To achieve this the linking length must be allowed to increase as a function of redshift.

The unbiased selection of groups is also affected by redshift-space distortions. Peculiar motions of galaxies along the line of sight will alter the observed redshift and hence the distance determination. This results in an increase in the observed separation of group members, but only in the direction parallel to the line of sight. In order to account for this effect, the linking length must be elongated, extending further along the line of sight than across the plane of the sky.

The 2dF group finder takes the effects described above into account and is calibrated using numerical simulations, such that the groups detected are unbiased indicators of the underlying dark matter halos. For more information on the exact details of the implementation of the group finder, see Eke et al. (2003).

The 2dF catalogue also provides several other useful group parameters: the velocity dispersion of the group, its projected radius and an estimate of the group mass. The velocity dispersion $\sigma$ was calculated using the gapper estimator of Beers, Flynn & Gebhardt (1990), which is a robust estimator that is insensitive to outlying velocities. The projected radius $R$ was defined as the root mean squared projected separation of the members from the group centre. It was then possible to estimate the mass $M$ of the group using the virial theorem

$$M = \alpha \frac{\sigma^2 R}{G}. \tag{5.5}$$

Numerical simulations run by the 2dF team showed that, for the sample to have

an unbiased median mass, the parameter $\alpha$ should have a value of 5.5. The mass, RMS radius and mean group redshift were used to generate models of the expected gravitational redshift (see Section 5.3.3).

## 5.3 Analysis

### 5.3.1 Defining Subsamples

As described in Section 5.1, the gravitational redshift of a group is calculated by taking the median of the redshifts in the inner and outer regions, then taking the difference between these values. In order to obtain a meaningful velocity shift there must be a reasonable number of galaxies in a group, so that the median is not too dependent on the velocity of an individual group member. Since the catalogue includes groups with as few as 4 members, it was necessary to impose a cut on the minimum number of galaxies in the groups to be considered.

While rejecting groups with few members resulted in more accurate determinations of the median, the properties of the sample meant that the number of groups with many members was much less than the number with fewer members (see Figure 5.3). Therefore imposing too high a cut would result in a large reduction in the number of groups in the sample. A value of $N_{\rm min} = 10$ was eventually selected, providing a compromise between accurate medians and sample size.

Once all groups with less than 10 members were removed, the sample was divided into three subsamples based on the velocity dispersion of the groups. The split was made such that each subsample had a roughly equal number of groups in it. Since the velocity dispersion of a cluster provides some indication of the underlying mass, dividing the sample up in this way allowed us to explore the properties of different kinds of systems while still binning the data sufficiently to reduce the intrinsic scatter (and hence the errors).

Table 5.1 shows some parameters of the subsamples. Note how the typical physical size of a cluster $\overline{R}_{\rm rms}$ increases with cluster mass.

| Subsample | $N_{\rm gal}$ | $N_{\rm grp}$ | $\overline{\sigma}(\,{\rm km\,s^{-1}})$ | $\overline{R}_{\rm rms}$ (kpc) | $\overline{M}(\times 10^{14} M_{\odot})$ |
|---|---|---|---|---|---|
| Low | 5745 | 405 | 213.1 | 675.4 | 0.39 |
| Medium | 7362 | 405 | 341.3 | 826 | 1.2 |
| High | 10076 | 407 | 596.9 | 1112 | 5.0 |
| All | 23183 | 1217 | 384.1 | 871.5 | 1.6 |

Table 5.1: Properties of the low ($\sigma < 278.8\,{\rm km\,s^{-1}}$), medium ($278.8\,{\rm km\,s^{-1}} < \sigma < 408.5\,{\rm km\,s^{-1}}$) and high ($\sigma > 408.5\,{\rm km\,s^{-1}}$) velocity dispersion subsamples. The columns show the number of galaxies ($N_{\rm gal}$) and groups ($N_{\rm grp}$) in each subsample, as well as their mean velocity dispersion ($\overline{\sigma}$), RMS projected radius ($\overline{R}_{\rm rms}$) and mass ($\overline{M}$).

### 5.3.2 Determining the Cluster Density Distribution

In order to calculate the expected magnitude of the projected gravitational redshift, it was necessary to determine a mean density profile for each of the cluster subsamples. This is required in order to project the intrinsic gravitational redshift on to the plane of the sky using Equation 3.2.

The average density distributions for the three subsamples were obtained using the following method:

1. Histograms of the radial number count $R/R_{\rm rms}$ were constructed for each group in the survey. Dividing the radial distance of each galaxy by the RMS radius of its parent group provided a measure of the radial distribution of galaxies in the group, independent of its physical size.

2. The individual histograms were summed together to produce one histogram per velocity dispersion subsample. This was possible because the radial number counts were constructed in a scale independent fashion.

3. The subsample histograms were converted into projected density distributions, by dividing by the area of the annulus enclosing the galaxies in each radial bin.

The results of this method are shown in Figure 5.4. There are two points to note about the density profile: (1) The shape of the density profile appears to be largely independent of the mean velocity dispersion of the subsample. (2) The density distribution is reasonably well fitted with an exponential profile of the

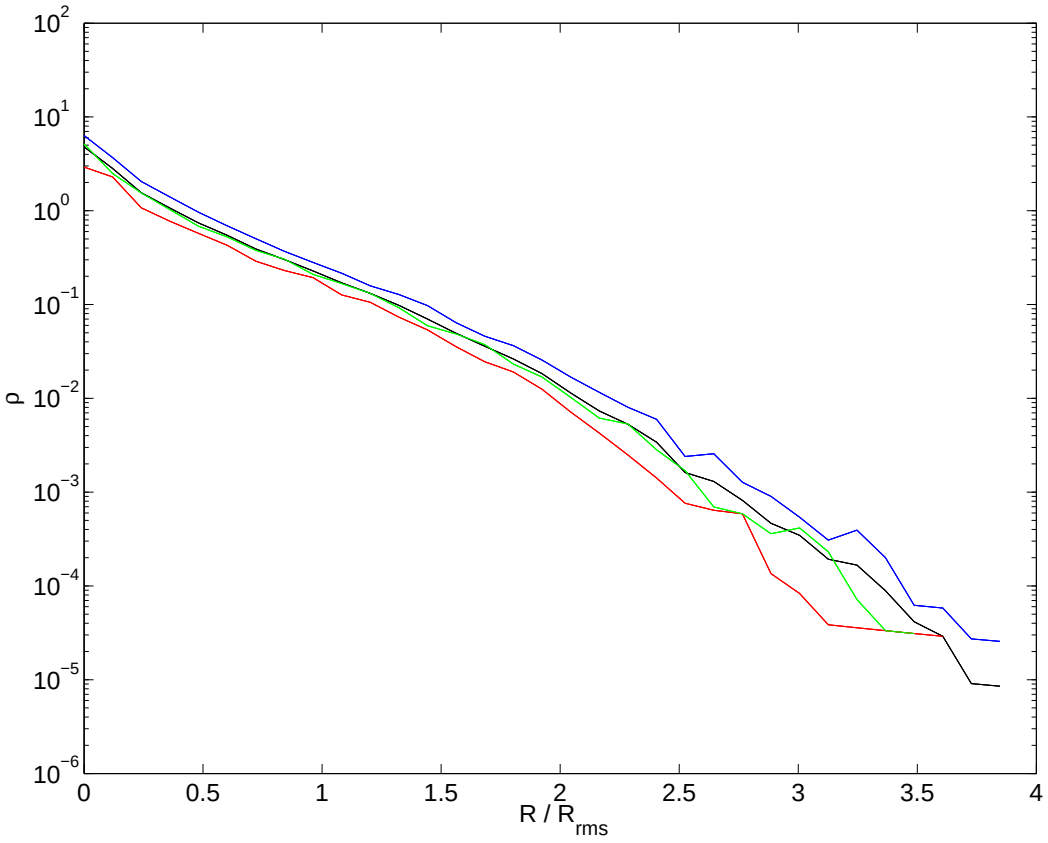


Figure 5.4: Density profile of the 2dF groups, divided into velocity dispersion subsamples. The red, green and blue lines show the low, medium and high velocity dispersion subsamples respectively. The black line represents the full sample.

form

$$\rho(R) \propto e^{-R/R_s}, \tag{5.6}$$

where $R_s = 0.305 R_{\rm rms}$. This result supports previous work which indicates that the inner regions of clusters follow an exponential density profile (Merrifield & Kent 1989) and hints that clusters of galaxies may have a universal density profile with a physical size that scales in relation to its mass.

Since the subsamples showed such homogeneity in their density profiles, the same overall profile was used when generating the models. The only difference was that the value of $R_s$ was scaled by the mean RMS radius of each subsample.

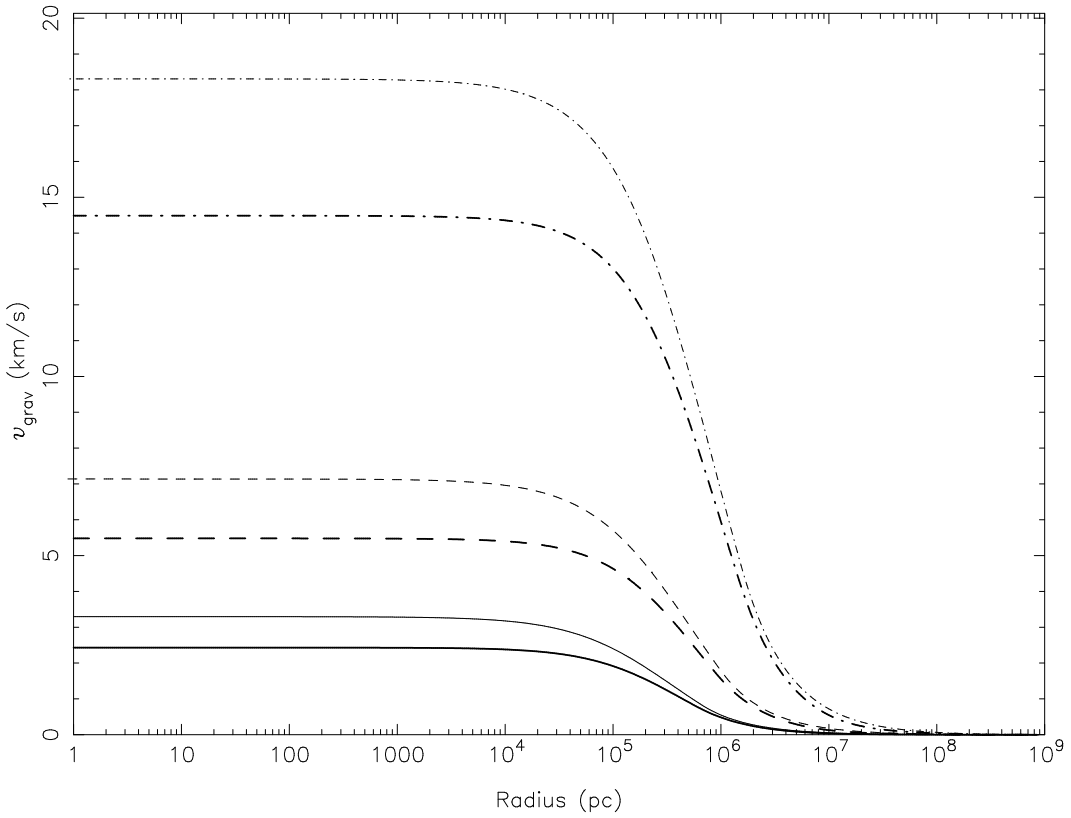


Figure 5.5: Predicted intrinsic (thin lines) and projected (thick lines) gravitational redshift for the three subsamples. Solid, dashed and dotted lines represent the low, medium and high velocity dispersion subsamples respectively.

### 5.3.3 Predicted Signal from Models

The expected gravitational redshift signal was calculated using the method developed in Chapter 4. For each subsample a NFW density profile (Navarro, Frenk & White 1997) was used, with a mass equal to the mean mass of the subsample. An exponential light profile, scaled by the mean RMS radius of the groups was used to project the intrinsic gravitational redshift and velocity dispersion onto the plane of the sky.

Figure 5.5 shows the predicted shift for the three subsamples. There are two features to note from the plot:

1. The level of the predicted gravitational redshift is an order of magnitude greater than the redshift predicted for `M60` in Chapter 4. It is not at the level of $100\,\mathrm{km\,s^{-1}}$ as predicted by Cappi (1995). A likely explanation for

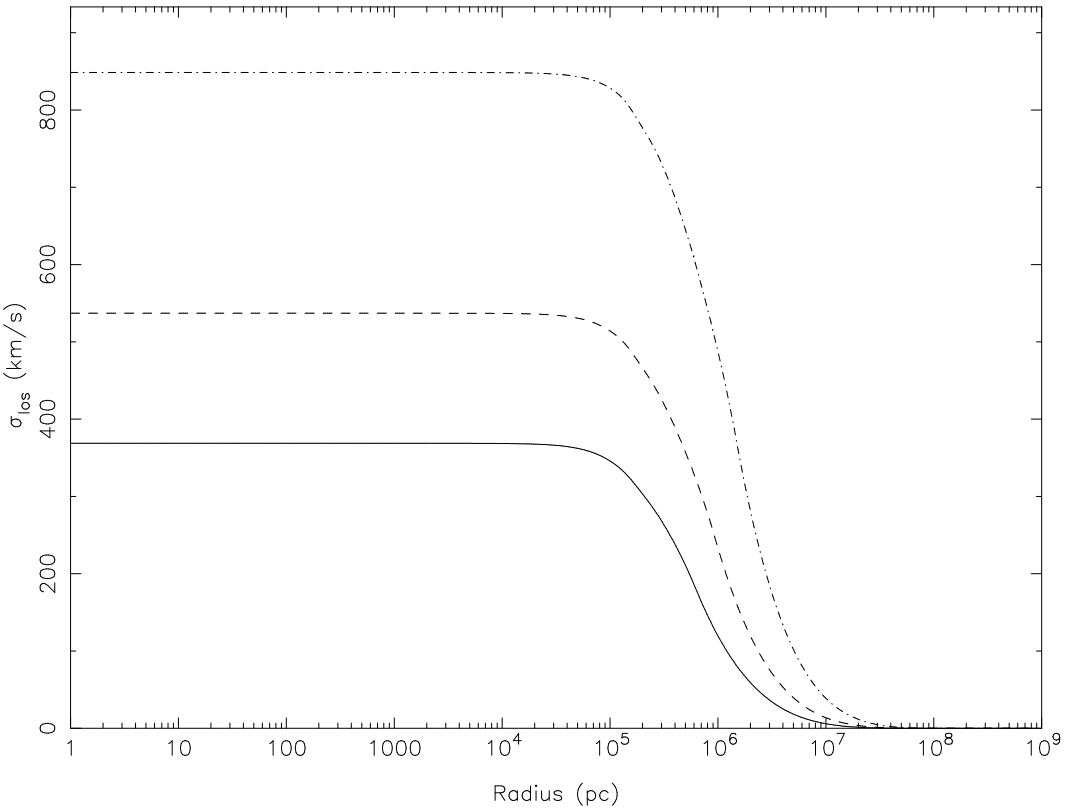


Figure 5.6: Predicted projected velocity dispersions for the three subsamples, assuming an isotropic distribution of orbits. Solid, dashed and dotted lines represent the low, medium and high velocity dispersion subsamples respectively. The magnitude and shape of the profiles are not significantly affected by introducing anisotropic orbits.

this difference is that the 2PIGG sample contains not only massive rich clusters, but a large number of smaller groups. In fact, these smaller groups dominate the sample (see Figure 5.3), reducing the mean signal expected. Unfortunately, limiting the sample to only those groups with a very large velocity dispersion would reduce the number of galaxies dramatically, which would lead to large errors on the observed gravitational redshift.

2. The gradient of the gravitational redshift signal is steepest at a physical scale of $\sim 1\,\mathrm{Mpc}$, roughly independent of the mass of the cluster. Since the gravitational redshift is measured by dividing each group into inner and outer regions, selecting the cut-off radius $R_{\mathrm{cut}}$ at this distance will maximise the amount of signal detected.

| $\sigma$ Subsample | min(r) $> R_{\rm cut}$ | max(r)$< R_{\rm cut}$ |
|---|---|---|
| Low | 0 | 106 |
| Medium | 0 | 59 |
| High | 12 | 16 |

Table 5.2: Number of groups rejected from subsamples due to either the inner or outer bin containing no galaxies.

Although a cut-off at $\sim 1$ Mpc will maximise the signal obtained, selecting a fixed distance is in conflict with the desire to minimise the statistical noise introduced by the velocity dispersion of the cluster (see Section 5.1.2). Ideally, an optimal cut-off radius would maximise the *signal-to-noise* by taking both of these effects into account. For this work however it was decided to simply maximise the signal and hope that the large number of clusters available would reduce the statistical noise to an acceptable level.

As well as predicting the level of the gravitational redshift, the code can also predict the velocity dispersion profile of the cluster subsamples. Figure 5.6 shows the predicted profiles for the three subsamples, obtained by assuming that the motions of the galaxies in the cluster are isotropic. The luminosity weighted average of these profiles gives overall velocity dispersions of $251\,{\rm km\,s^{-1}}$, $376\,{\rm km\,s^{-1}}$ and $609\,{\rm km\,s^{-1}}$ for the low, medium and high $\sigma$ subsamples. These compare well with the mean velocity dispersions provided by the 2dF team of $213\,{\rm km\,s^{-1}}$, $341\,{\rm km\,s^{-1}}$ and $597\,{\rm km\,s^{-1}}$. The similarity between the two velocity dispersion determinations provides confidence that the gravitational redshift models are correct. Although Figure 5.6 assumes isotropy, it was found that anisotropic orbits yielded similar results ($\beta = \pm 0.5$ models resulted in a $\sim 5\%$ variation in the magnitude of the signal compared to the isotropic case, without any significant shift in the radius of the break point).

### 5.3.4 Obtaining the Signal from the Sample

The observed gravitational redshift for each group was obtained using the method described earlier in this chapter. A physical scale of $R_{\rm cut} = 1$ Mpc was chosen for the cut-off between the inner and outer regions. 1 Mpc was selected on the basis of the predicted signal as discussed in the previous section. The mean redshift of each group was used to determine the distance to the group, which allowed the

physical 1 Mpc scale to be converted into an angular distance.

Since the cut-off was defined by a physical scale, rather than a fraction of the group size, there were cases where either the inner or outer regions contained no galaxies. Groups where this was the case were removed from the subsample. A total of 193 groups were rejected in this way, 181 because no galaxies lay outside the 1 Mpc break, 12 because none were inside that distance. Table 5.2 shows the distribution of the rejected groups between the three subsamples.

The gravitational redshift for each group was then determined by taking the difference between the median velocity in the inner and outer regions. These individual velocity shifts were then averaged within each $\sigma$ subsample to give an overall gravitational redshift. The errors on the shifts were determined from the spread of the velocities within the subsample, according to Equation 5.2, where $N$ is the number of groups in that subsample.

In order to compare the observed shift to the predictions of the gravitational redshift model, the model profiles were also binned into two radial bins, with the boundary between them at the same $R_{\rm cut}$ as the data. The binning was weighted using the projected density profile $\rho(R)$ in an analogous manner to Equation 2.14. The difference between the velocity of the two bins was used as the shift for that subsample.

Binning the data and models in this way resulted in some reduction of the observed signal, because of the gradual transition in the signal between the inner and outer values (see Figure 5.5). Using a single cut off radius tended to draw the velocity shifts in the inner and outer regions closer together, reducing $v_{\rm grav}$. A three region model was considered, with a 'buffer zone' between the inner and outer samples, but it was found that it would result in too many groups being excluded from the sample.

## 5.4 Results and Discussion

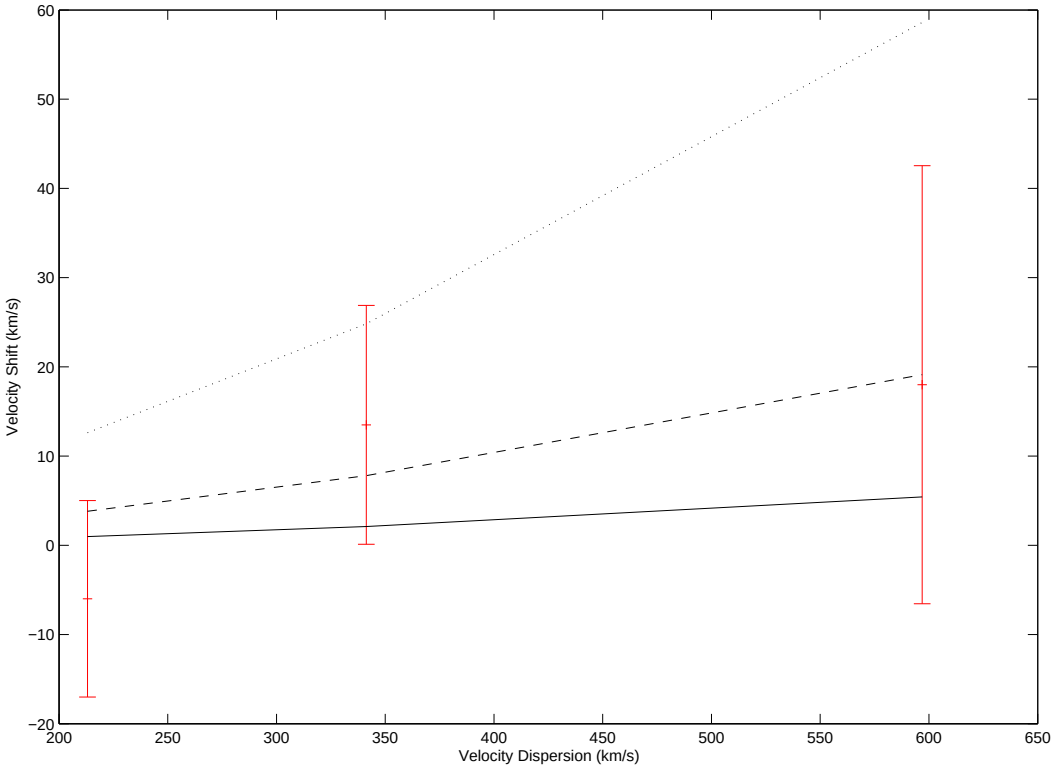


Figure 5.7: Variation in gravitational redshift with cluster velocity dispersion. The points represent the data for the three subsamples. The solid, dashed and dotted lines show models with 1, 10 and 100 times the mass predicted ($\sim 10^{14}\,M_{\odot}$, $\sim 10^{15}\,M_{\odot}$ and $\sim 10^{16}\,M_{\odot}$).

Figure 5.7 shows how the gravitational redshift varies depending on the mean velocity dispersion of the subsample. The solid line shows the predicted values from the model, while the three points represent the three $\sigma$ subsamples. The dashed and dotted lines show the shift expected for models with larger masses, in order to indicate how the data constrain halo mass.

Clearly the current quantity of data is insufficient to apply strong constraints to the amount of mass in cluster halos, with halos of $\sim 10^{16} M_{\odot}$ only just being ruled out at 95% confidence. Although at present the errors in the data are too large, a bigger sample of galaxy groups should continue to reduce the errors on the values obtained. The Sloan Digital Sky Survey aims to obtain 1,000,000 galaxy redshifts, which will offer a factor of four increase on the size of the 2dF sample.

Assuming that the errors scale as $\sqrt{N}$, the Sloan sample should reduce the size of the error bars by 50%. Given the continuing interest in galaxy redshift surveys, it seems likely that the number of available clusters to consider is likely to continue to increase sufficiently to allow the measurement of halo masses. Alternatively, one could choose to focus solely on the clusters which are expected to produce the largest gravitational redshift. A redshift survey of a number of regular, high velocity dispersion clusters could also be expected to provide interesting results.

# Chapter 6

# Conclusions

## 6.1 Summary

### 6.1.1 Longslit Spectroscopy of M87

Longslit spectroscopy of the giant elliptical galaxy M87 was obtained at two perpendicular position angles using the ISIS spectrograph on the WHT. The data were analysed using the Gauss-Hermite Fourier fitting software of van der Marel & Franx (1993), to obtain mean velocity and velocity dispersion profiles out to a radius of $\sim 80$ arcsec. The results showed good agreement with existing stellar kinematics and indicated a smooth transition to the planetary nebulae kinematics of Romanowsky et al. (in preparation) in the outer halo. The gently rising profile beyond 100 arcsec may indicate the location of the boundary between the galaxy and cluster environments.

The mass distribution was found from the velocity dispersion profile by solving the Jeans equation, under the assumption of (1) spherical symmetry and (2) a constant mass-to-light ratio. The effects of projection, atmospheric seeing and spatial binning were taken into account before comparison with the kinematics.

Several classes of model were considered. In each case, the mass-to-light ratio and orbital anisotropy of the model were allowed to vary in order to obtain the best fit to the data. The first mass distribution considered consisted of a constant mass-to-light ratio component, plus a central black hole. The central black hole mass could be either defined in advance, or be allowed to vary as an additional parameter in the fit in order to minimise $\chi^2$. If no central black hole was included,

the best fit mass-to-light ratio was $\Upsilon = 7.07 \pm 0.21$ while the orbital anisotropy was $\beta = 0.64 \pm 0.024$. Introducing a central black hole of mass $2 \times 10^9\, M_\odot$ had little effect on the mass-to-light ratio ($\Upsilon = 7.08 \pm 0.17$), but resulted in less radially anisotropic orbits ($\beta = 0.56 \pm 0.025$). In general it was found that central black hole mass could be traded off against orbital anisotropy, which made it difficult to constrain the central black hole mass (see Figure 2.8). The best-fit black hole mass was $M_{\rm BH} = 4.48 \times 10^8\, M_\odot$ which was obtained with $\Upsilon = 7.12 \pm 0.21$ and $\beta = 0.61 \pm 0.13$, although black hole masses in the range $0 - 3.73 \times 10^9\, M_\odot$ were all consistent with the data. This range of masses is in agreement with existing mass determinations of $M_{\rm BH} = 2.4 \pm 0.7 \times 10^9\, M_\odot$ (Harms et al. 1994) and $M_{\rm BH} = 3.2 \pm 0.9 \times 10^9\, M_\odot$ (Macchetto et al. 1997). The poor constraint on the mass of the central black hole was to be expected, since the black hole only influences the stellar kinematics very near to the centre. The combination of spatial binning and atmospheric seeing limited the number of independent data points in the central region to the extent that the mass could not be well constrained.

Since `M87` lies at the centre of the Virgo Cluster, a two component model was also considered, which was composed of a constant mass-to-light ratio component and a dark halo. The dark halo used an NFW profile to represent the mass of the cluster. The mass of the halo, along with $\Upsilon$ and $\beta$ were left as free parameters. The best-fit values obtained were $\Upsilon = 5.34 \pm 0.34$, $\beta = 0.71 \pm 0.03$ and $M_{\rm halo} = 2.64 \pm 0.92 \times 10^{12}\, M_\odot$. Although these values fit well in the inner regions (where there are many data points with small errors from the stellar kinematics), the fit is poorer to the planetary nebulae data in the halo. Comparisons of the mass distribution to other mass estimates (see Figure 2.11) confirm this — the mass in the outer regions is underestimated compared to X-ray gas measurements. The poor fit was attributed to the simplicity of the model used: there is no reason for the orbital anisotropy to remain constant as a function of radius. An alternative model with a halo mass of $7.3 \times 10^{13}\, M_\odot$, for which $\beta$ was allowed to vary radially was able to fit the data from a variety of sources over 3 orders of magnitude in radius. The flexibility introduced by varying the anisotropy of the stellar orbits makes it very difficult to constrain the mass distribution in elliptical galaxies. This degeneracy is, unfortunately, unavoidable when determining the mass distribution from kinematics using the Jeans equation.

### 6.1.2 A Statistical Approach to Measuring Gravitational Redshift

In order to break the mass-anisotropy degeneracy, an alternative method of determining an elliptical galaxy's mass distribution was considered: gravitational redshift. Previous work by Stiavelli & Setti (1993) indicated that the effect should occur at a level of $\sim 10 - 20\,\mathrm{km\,s^{-1}}$ at the centre of a typical elliptical galaxy. The Stiavelli & Setti sample was reanalysed using a gravitational redshift model developed for this work, which took into account the effect of deprojection, atmospheric seeing and spatial binning on the gravitational redshift profile. $H$-band HST photometry was used to reduce contamination of the density distribution by gas and young stars. The even component of the stellar kinematics was obtained and compared to a range of mass models for each galaxy. The mass-to-light ratio of each galaxy was found by selecting the model that best fit the data. Mass-to-light ratios were also determined independently from the velocity dispersion profiles, using the method outlined in Chapter 2.

The gravitational redshift in each individual galaxy was expected to suffer from some intrinsic scatter due to the physical and instrumental effects discussed in Chapter 3. To reduce this scatter, the galaxies were considered together and a statistical approach was used to determine the average mass-to-light ratio of the whole sample. The results obtained from the velocity dispersion profiles were combined in the same fashion and both sets of mass-to-light ratios were compared with predicted values from stellar population models.

The gravitational redshift method gave a predicted mass-to-light ratio of $\overline{\Upsilon}_v = 4.84 \pm 2.67$, while the velocity dispersion measurements predicted $\overline{\Upsilon}_\sigma = 1.67 \pm 0.1$. Given the size of the uncertainties, these results are not statistically inconsistent. Stellar population models predict $H$-band mass-to-light ratios of $\sim 1$. Given the uncertainty in the both the predicted value and the determination from the gravitational redshift, the predicted values are consistent with little dark matter in the sample galaxies. Although dark matter has been shown to dominate the outer regions of elliptical galaxies, in the central regions it is common for the stellar mass to be the dominant component.

### 6.1.3 Integral Field Spectroscopy of M60

While the statistical approach described above gave some tentative evidence of gravitational redshift at the level predicted, it would be more useful to be able to map the mass distributions of individual galaxies. Improvements in observational techniques have reduced the error in determining stellar kinematics to the level where this may now be possible. A pilot study was performed, in order to assess the feasibility of using integral field spectroscopy to measure gravitational redshift in the core of M60.

In order to achieve the high spectral resolution required, the observations were carried out using INTEGRAL/WYFFOS on the WHT in echelle mode. Unfortunately, poor weather at the observing site led to $\sim 3$ arcsec atmospheric seeing and some difficulty with the spectrograph led to additional problems removing scattered light from the flat field frames. The reduced stellar spectra were binned using the Voronoi tessellation method of Cappellari & Copin (2003), which resulted in roughly circular bins of similar signal-to-noise ratio.

Velocity and velocity dispersion measurements were obtained using the Gauss-Hermite Fourier fitting software of van der Marel & Franx (1993). The resulting 2-dimensional maps were compared with existing longslit data. The mean velocity map agreed well with the kinematics of Fisher, Illingworth & Franx (1995), clearly showing rotation at a level of $\sim 50\,\mathrm{km\,s^{-1}}$. The axis of rotation was found to lie at a position angle of 5°, which corresponds to the minor axis in the inner region (Peletier et al. 1990). The velocity dispersion map showed less agreement with existing data, with this work giving a systematically lower central velocity dispersion by $\sim 40\,\mathrm{km\,s^{-1}}$. The difference was attributed to problems subtracting the continuum given the unusually high central velocity dispersion of M60 ($\sim 400\,\mathrm{km\,s^{-1}}$).

Before attempting to detect gravitational redshift, the velocity field was investigated for any signs of coherent stellar streaming or kinematically distinct cores. This was achieved by unsharp masking the data along the spectral direction, then cross correlating the result with a stellar template. If coherent cross-correlation peaks were found across several independent spatial bins it could be attributed to low surface brightness stellar streams, superimposed on top of the galaxies light profile. None were found, which added weight to the assumption that the galaxy was reasonably undisturbed.

The gravitational redshift models developed in Chapter 3 were used to generate models for the galaxy based on its light profile. In order to remove the effect of rotation, the velocity field was divided into radial annuli. The velocity for each ring was then obtained from the mean of the individual Voronoi bin velocities.

Unfortunately it was found that the gravitational redshift predicted by the models for `M60` was only $0.5\,\mathrm{km\,s^{-1}}$. This was surprising given the galaxy's large central velocity dispersion and the predictions of existing models. It was found that while the total gravitational redshift was significantly larger, the shallow central light profile of `M60` spread the redshift over a large radial range meaning that the gravitational redshift could not be detected in this case.

Predictions showed that compact elliptical galaxies are more suitable for this work. A constant mass-to-light ratio model for `M32` predicted a shift of $\sim 6\,\mathrm{km\,s^{-1}}$ within the central 10 arcsec. `M32` would provide twice the number of counts obtained for `M60` as well as at least twice as many resolved absorption features (due to its significantly lower velocity dispersion). This additional signal and the removal of the error associated with the scattered light, means that it should indeed be possible to measure the mean velocity of a single galaxy to the degree of accuracy required.

### 6.1.4 Gravitational Redshift in the 2dF Groups Catalogue

Although galaxies are a more dynamically stable environment in which to attempt to measure gravitational redshift, the larger mass of clusters of galaxies are expected to result in an order of magnitude increase in the redshift signal. It has been previously suggested (Stiavelli & Setti 1993) that gravitational redshift could be detected in clusters by comparing the redshift of central cD galaxies to the mean redshift of the cluster. This method has had some success (Cappi 1995; Broadhurst & Scannapieco 2000), but has the drawback that it can only be applied to clusters which contain an identifiable central galaxy.

A new method of obtaining the gravitational redshift in clusters was developed, which involved taking the difference between the median redshift in the inner and outer regions of a cluster. Numerical simulations were performed in order to determine the expected velocity scatter due to the intrinsic velocity dispersion of the cluster and due to galaxy infall along the line of sight. The effect of projection on to the plane of the sky was also considered.

The simulations described above showed that, in order to reduce the errors, it was crucial to study a large sample (both in terms of the number of clusters and the number of galaxies per cluster). For this reason, the 2dF Percolation-Inferred Galaxy Group (2PIGG) catalogue was used. It consists of 54,888 galaxies in 7,259 groups and offers a homogeneous sample of galaxy groups with which to do the analysis. After rejecting groups with less than 10 members, the sample was divided by group velocity dispersion into three equal subsamples. This made it possible to determine if the measured shift was mass dependent.

In order to obtain the intrinsic gravitational redshift from the projected redshift that was observed, it was necessary to determine the typical density distribution of galaxies within a cluster. This was obtained by considering the area weighted number counts in circular annuli from the cluster centre, for each of the three subsamples. It was found that the density distribution followed an exponential profile, in agreement with the prediction of Merrifield & Kent (1989). Furthermore, aside from the differing scale length, the three profiles showed remarkable agreement with each other (see Figure 5.4). This suggests that clusters of galaxies can be fit by a universal density profile, which scales in relation to the mass of the cluster.

Gravitational redshift models for clusters were generated using NFW density profiles. It was found that the change in predicted gravitational redshift with radius was steepest at a radius of $\sim 1\,\mathrm{Mpc}$, independent of the subsample considered. This was used to define the cut off radius between the inner and outer regions of each group in order to maximise the measured gravitational redshift.

Plotting the observed central shift against the mean velocity dispersion of the subsample showed a slight indication of a positive correlation, but not at a statistically significant level. The errors on the observed values were still too high to rule out all but the most massive cluster halos ($M_{\mathrm{halo}} \sim 10^{16}\,M_{\odot}$). The increasing quantity and quality of galaxy redshift surveys provides reason for optimism — when complete the Sloan Digital Sky Survey will immediately quadruple the available sample size (and hence half the errors) in comparison to the 2PIGG catalogue. Alternatively smaller redshift surveys of the most massive, regular clusters could also be successful in detecting gravitational redshift in clusters.

## 6.2 Future Work

### 6.2.1 Gravitational Redshift in Elliptical Galaxies

It has been shown that, given careful target selection, it should be possible to measure the stellar kinematics in the centre of compact elliptical galaxies to the accuracy required to make a statistically significant detection of gravitational redshift. Future improvements in the size and number of elements in integral field units, combined with the introduction of adaptive optics will further improve the chances of a successful detection.

There are of course a number of issues that complicate the measurement of gravitational redshift that cannot be solved by higher resolution or longer exposure times. Non-equilibrium motions in galaxy cores can mimic the gravitational redshift signal and can only be differentiated statistically by considering a large sample of galaxies. A dedicated study using integral field spectroscopy of a number of nearby compact ellipticals would help determine the magnitude and frequency of such motions.

The unsharp masking technique used in Chapter 4 could be of some use in quantifying the extent of stellar streaming motions, but would also be scientifically interesting in its own right. The technique used in this work was rather basic and could easily be improved upon. For instance, rather than subtracting a smoothed version of the spectrum (which will result in some broadening of the absorption lines) the best-fit spectrum obtained from a standard kinematic analysis could be subtracted instead. It would also be useful to test the technique by observing a galaxy which showed recent signs of merger activity or stellar streaming. Astrophysical phenomena such as the supposed tidal arc in the Andromeda Galaxy (Ibata et al. 2001; Ferguson et al. 2002) are likely to exist in more distant galaxies and this kind of analysis could be used to detect it.

In this thesis the mean velocity was determined using the Fourier fitting software of van der Marel & Franx (1993). Since the gravitational redshift relies only on the determination of the mean of the line-of-sight velocity distribution, it may be beneficial to use a less complicated approach to obtain a more robust mean velocity.

### 6.2.2 Gravitational Redshift in Galaxy Clusters

Determining the gravitational redshift in clusters of galaxies is made difficult by the uncertainty in the equilibrium state of clusters and the intrinsic velocity dispersion of the clusters. There are two approaches to the problem (1) considering only a subset of the most massive, regular clusters or (2) using a large enough sample such that the uncertainties are significantly reduced. The Sloan Digital Sky Survey will offer a significant improvement in numbers by providing a homogeneous sample of $\sim 1,000,000$ individual galaxy redshifts.

## 6.3 The Big Picture

The goal of the work described in this thesis was to (1) measure the gravitational redshift generated due to large concentrations of visible and dark matter in the Universe and (2) to use the result to directly constrain the underlying mass distribution.

It was found that, while gravitational redshift is a clean, fundamental test of the distribution of mass in astrophysical objects, it does suffer from a number of technical problems. Careful target selection and observations may be able to reduce these difficulties to a level where gravitational redshift is able to be used as another tool in determining the nature of dark matter.

# Bibliography


Arribas, S., del Burgo, C., Carter, D., Cavaller, L., Edwards, R., Fuentes, J., García, A., Gentles, B., Herreros, J. M., Jones, L., Mediavilla, E., Pi, M., Pollacco, D., Rees, P., Sosa, N., 1998. *INTEGRAL Users Manual.*

Ashman, K. M., 1992, Publ. Astron. Soc. Pacific, **104**, 1109.

Beers, T. C., Flynn, K., Gebhardt, K., 1990, Astron. J., **100**, 32.

Bender, R., 1990, Astron. Astrophys., **229**, 441.

Bender, R., Saglia, R. P., Gerhard, O. E., 1994, MNRAS, **269**, 785.

Bettoni, D., Buson, L. M., 1987, Astron. Astrophys. Suppl., **67**, 341.

Binney, J., Mamon, G. A., 1982, MNRAS, **200**, 361.

Binney, J., Merrifield, M., 1998. *Galactic astronomy.* Galactic astronomy / James Binney and Michael Merrifield. Princeton, NJ : Princeton University Press, 1998.

Binney, J., Tremaine, S., 1987. *Galactic dynamics.* Princeton, NJ, Princeton University Press, 1987, 747 p.

Brainerd, T. G., Blandford, R. D., Smail, I., 1996, Ap. J., **466**, 623.

Broadhurst, T., Scannapieco, E., 2000, Ap. J. Lett., **533**, L93.

Bullock, J. S., Kolatt, T. S., Sigad, Y., Somerville, R. S., Kravtsov, A. V., Klypin, A. A., Primack, J. R., Dekel, A., 2001, MNRAS, **321**, 559.

Byun, Y.-I., Grillmair, C. J., Faber, S. M., Ajhar, E. A., Dressler, A., Kormendy, J., Lauer, T. R., Richstone, D., Tremaine, S., 1996, Astron. J., **111**, 1889.

Caldwell, N., 1984, Publ. Astron. Soc. Pacific, **96**, 287.

Cappellari, M., Copin, Y., 2003, MNRAS, **342**, 345.

Cappi, A., 1995, Astron. Astrophys., **301**, 6.

Carr, B., 1994, Ann. Rev. Astron. Astrophys., **32**, 531.

Carter, D., Benn, C. R., Rutten, R. G. M., Breare, J. M., Rudd, P. J., King, D. L., Clegg, R. E. S., Dhillon, V. S., Arribas, S., Rasilla, J.-L., García, A., Jenkins, C. R., Charles, P. A., 1994. *ISIS Double Beam Spectrograph Users Manual.*

Cohen, J. G., Ryzhov, A., 1997, Ap. J., **486**, 230.

Colberg, J. M., White, S. D. M., Jenkins, A., Pearce, F. R., 1999, MNRAS, **308**, 593.

Davies, R. L., Birkinshaw, M., 1988, Ap. J. Suppl., **68**, 409.

De Bruyne, V., Dejonghe, H., Pizzella, A., Bernardi, M., Zeilinger, W. W., 2001, Ap. J., **546**, 903.

De Filippis, E., Schindler, S., Castillo-Morales, A., 2003, Astron. Astrophys., **404**, 63.

de Vaucouleurs, G., de Vaucouleurs, A., Corwin, H. G., 1976. *2nd reference catalogue of bright galaxies containing information on 4364 galaxies with reference to papers published between 1964 and 1975.* University of Texas Monographs in Astronomy, Austin: University of Texas Press, 1976.

de Vaucouleurs, G., de Vaucouleurs, A., Corwin, H. G., Buta, R. J., Paturel, G., Fouque, P., 1991. *Third Reference Catalogue of Bright Galaxies.* Volume 1-3, XII, 2069 pp. 7 figs.. Springer-Verlag Berlin Heidelberg New York.

Eke, V. R., Baugh, C. M., Cole, S., Frenk, C. S., Norberg, P., Peacock, J. A., Baldry, I. K., Bland-Hawthorn, J., Bridges, T., Cannon, R., Colless, M., Collins, C., Couch, W., Dalton, G., De Propris, R., Driver, S. P., Efstathiou, G., Ellis, R. S., Glazebrook, K., Jackson, C., Lahav, O., Lewis, I., Lumsden, S., Maddox, S., Madgwick, D., Peterson, B. A., Sutherland, W., K., T., 2003, In preparation.

Faber, S. M., Gallagher, J. S., 1979, Ann. Rev. Astron. Astrophys., **17**, 135.

Ferguson, A. M. N., Irwin, M. J., Ibata, R. A., Lewis, G. F., Tanvir, N. R., 2002, American Astronomical Society Meeting, **200**.

Ferrarese, L., Mould, J. R., Kennicutt, R. C., Huchra, J., Ford, H. C., Freedman, W. L., Stetson, P. B., Madore, B. F., Sakai, S., Gibson, B. K., Graham, J. A., Hughes, S. M., Illingworth, G. D., Kelson, D. D., Macri, L., Sebo, K., Silbermann, N. A., 2000, Ap. J., **529**, 745.

Fisher, D., Illingworth, G., Franx, M., 1995, Ap. J., **438**, 539.

Fried, J. W., Illingworth, G. D., 1994, Astron. J., **107**, 992.

Harms, R. J., Ford, H. C., Tsvetanov, Z. I., Hartig, G. F., Dressel, L. L., Kriss, G. A., Bohlin, R., Davidsen, A. F., Margon, B., Kochhar, A. K., 1994, Ap. J. Lett., **435**, L35.

Henry, J. P., Briel, U. G., Nulsen, P. E. J., 1993, Astron. Astrophys., **271**, 413.

Hoekstra, H., Franx, M., Kuijken, K., 2000, Ap. J., **532**, 88.

Ibata, R., Irwin, M., Lewis, G., Ferguson, A. M. N., Tanvir, N., 2001, Nature, **412**, 49.

Jedrzejewski, R., Schechter, P. L., 1989, Astron. J., **98**, 147.

Joseph, C. L., Merritt, D., Olling, R., Valluri, M., Bender, R., Bower, G., Danks, A., Gull, T., Hutchings, J., Kaiser, M. E., Maran, S., Weistrop, D., Woodgate, B., Malumuth, E., Nelson, C., Plait, P., Lindler, D., 2001, Ap. J., **550**, 668.

Kaiser, N., 1996. Weak Gravitational Lensing: Current Status and Future Prospects. In *Gravitational dynamics*, page 181. astro-ph/9509019.

Katgert, P., Mazure, A., Perea, J., den Hartog, R., Moles, M., Le Fevre, O., Dubath, P., Focardi, P., Rhee, G., Jones, B., Escalera, E., Biviano, A., Gerbal, D., Giuricin, G., 1996, Astron. Astrophys., **310**, 8.

Kuijken, K., Merrifield, M. R., 1993, MNRAS, **264**, 712.

Landau, L. D., Lifshitz, E. M., 1975. *The classical theory of fields.* Course of theoretical physics - Pergamon International Library of Science, Technology, Engineering and Social Studies, Oxford: Pergamon Press, 1975, 4th rev.engl.ed.

Lauer, T. R., 1985, MNRAS, **216**, 429.

Lauer, T. R., Faber, S. M., Lynds, R. C., Baum, W. A., Ewald, S. P., Groth, E. J., Hester, J. J., Holtzman, J. A., Kristian, J., Light, R. M., O'Neil, E. J., Schneider, D. P., Shaya, E. J., Westphal, J. A., 1992, Astron. J., **103**, 703.

Lauer, T. R., Ajhar, E. A., Byun, Y.-I., Dressler, A., Faber, S. M., Grillmair, C., Kormendy, J., Richstone, D., Tremaine, S., 1995, Astron. J., **110**, 2622.

Macchetto, F., Marconi, A., Axon, D. J., Capetti, A., Sparks, W., Crane, P., 1997, Ap. J., **489**, 579.

McNamara, B. R., Wise, M. W., Nulsen, P. E. J., David, L. P., Carilli, C. L., Sarazin, C. L., O'Dea, C. P., Houck, J., Donahue, M., Baum, S., Voit, M., O'Connell, R. W., Koekemoer, A., 2001, Ap. J. Lett., **562**, L149.

Merrifield, M. R., Kent, S. M., 1989, Astron. J., **98**, 351.

Milgrom, M., 1983, Ap. J., **270**, 365.

Mould, J. R., Oke, J. B., de Zeeuw, P. T., Nemec, J. M., 1990, Astron. J., **99**, 1823.

Navarro, J. F., Frenk, C. S., White, S. D. M., 1997, Ap. J., **490**, 493.

Nulsen, P. E. J., Bohringer, H., 1995, MNRAS, **274**, 1093.

Oort, J. H., 1932, Bull. Astron. Inst. Netherlands, **6**, 249.

Oosterloo, T., Balcells, M., Carter, D., 1994, MNRAS, **266**, L10.

Ostriker, J. P., Peebles, P. J. E., 1973, Ap. J., **186**, 467.

Peletier, R. F., Davies, R. L., Illingworth, G. D., Davis, L. E., Cawson, M., 1990, Astron. J., **100**, 1091.

Press, W. H., Teukolsky, S. A., Vetterling, W. T., Flannery, B. P., 1992. *Numerical recipes in C. The art of scientific computing.* Cambridge: University Press, —c1992, 2nd ed.

Prugniel, P., Heraudeau, P., 1998, Astron. Astrophys. Suppl., **128**, 299.

Ravindranath, S., Ho, L. C., Peng, C. Y., Filippenko, A. V., Sargent, W. L. W., 2001, Astron. J., **122**, 653.

Roszkowski, L., 1999. Non-Baryonic Dark Matter-A Theoretical Perspective. In *AIP Conf. Proc. 478: COSMO-98*, page 316. hep-ph/9903467.

Sandage, A., Tammann, G. A., 1987. *A revised Shapley-Ames Catalog of bright galaxies.* Carnegie Institution of Washington Publication, Washington: Carnegie Institution, 1987, 2nd ed.

Sargent, W. L. W., Young, P. J., Lynds, C. R., Boksenberg, A., Shortridge, K., Hartwick, F. D. A., 1978, Ap. J., **221**, 731.

Seljak, U., 2000, MNRAS, **318**, 203.

Sembach, K. R., Tonry, J. L., 1996, Astron. J., **112**, 797.

Statler, T. S., 1991, Ap. J. Lett., **382**, L11.

Stiavelli, M., Setti, G., 1993, MNRAS, **262**, L51.

Tonry, J. L., Dressler, A., Blakeslee, J. P., Ajhar, E. A., Fletcher, A. B., Luppino, G. A., Metzger, M. R., Moore, C. B., 2001, Ap. J., **546**, 681.

Tran, H. D., Tsvetanov, Z., Ford, H. C., Davies, J., Jaffe, W., van den Bosch, F. C., Rest, A., 2001, Astron. J., **121**, 2928.

Trinchieri, G., Fabbiano, G., Canizares, C. R., 1986, Ap. J., **310**, 637–659.

van der Marel, R. P., 1994, MNRAS, **270**, 271.

van der Marel, R. P., Franx, M., 1993, Ap. J., **407**, 525.

van Dokkum, P. G., 2001, Publ. Astron. Soc. Pacific, **113**, 1420.

van Dokkum, P. G., Franx, M., 1995, Astron. J., **110**, 2027.

Vazdekis, A., Casuso, E., Peletier, R. F., Beckman, J. E., 1996, Ap. J. Suppl., **106**, 307.

Verolme, E. K., Cappellari, M., Copin, Y., van der Marel, R. P., Bacon, R., Bureau, M., Davies, R. L., Miller, B. M., de Zeeuw, P. T., 2002, MNRAS, **335**, 517.

Veron-Cetty, M.-P., Veron, P., 1988, Astron. Astrophys., **204**, 28.

Wagner, S. J., Bender, R., Moellenhoff, C., 1988, Astron. Astrophys., **195**, L5.

Wambsganss, J., 1998, Living Reviews in Relativity, **1**, 12.

Williams, T. B., 1976, Ph.D. Thesis.

Winsall, M. L., Freeman, K. C., 1993, Astron. Astrophys., **268**, 443.

Worthey, G., 1994, Ap. J. Suppl., **95**, 107.

Zabludoff, A. I., Huchra, J. P., Geller, M. J., 1990, Ap. J. Suppl., **74**, 1.

Zwicky, F., 1933, Helv. Phys. Acta 6, **110**.

Zwicky, F., 1937, Ap. J., **86**, 217.

# Acknowledgements

There are many people that I'd like to thank for their help, support and friendship during the course of my PhD.

My supervisor Mike for his patience and support (particularly during my writing up year) and for providing such clear and concise answers to my many questions. Steve and Aaron for generously allowing me to use some of their data in my thesis. Pete and Bryn for taking the time to proofread some of my chapters, and for the useful improvements they suggested. Nigel Douglas, Konrad Kuijken, Begoña Garcia Lorenzo, Tim de Zeeuw and Ellen Verolme for their assistance with various aspects of this work.

I would also like to thank the rest of the astronomy group and all my other friends and housemates who made my PhD so memorable. In particular there are a few people who will always spring to mind when I look back on my time at Nottingham. Ed, for all those forgotten nights at the Irish, and for patiently helping to spot all those missing semicolons. Patrick, for many great nights out and for letting me win at pool occasionally. Laura, for saving me from microwave meals during my last few weeks in Nottingham and for being such a thoughtful and caring friend. Bo, for sharing his vast knowledge of all things astronomical and for his ceaseless efforts to make England a more efficient country. I'll miss you all!

I owe a huge debt to my sister Alice, for encouraging me to carry on when things weren't going well. Finally, thanks to my parents, for helping me out during my final year when times were hard and for always encouraging me, no matter what direction my life may take.